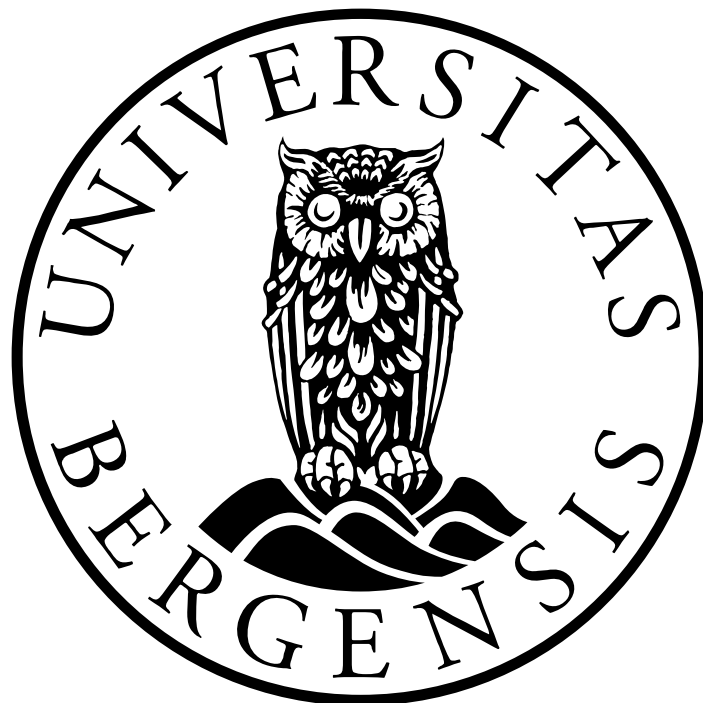


From outcrop to synthetic seismic: 2D and 3D modelling  
of igneous intrusions at Botneheia, central Spitsbergen

Sondre Hagevold



Master Thesis in Petroleum Geoscience

Department of Earth Science

University of Bergen

June 2019



## Abstract

The use of seismic reflection data and seismic modelling of igneous intrusions has greatly improved the understanding of igneous intrusions in sedimentary basins. However, there are still uncertainties in the seismic images of such intrusions, because they can have a complex architecture and their imaging potential is dependent on several factors. For instance, igneous intrusions crystallise from magma, which introduce heat to the host rocks in which they enter, resulting in a zone of contact metamorphism. Therefore, the present study analyses the effect a contact metamorphic aureole has on the seismic expression of igneous intrusions, and how intrusion geometries are imaged in both 2D- and 3D-seismic data. Digital outcrop models from the locality of Botneheia, Svalbard, from both lidar-data and photogrammetry, are first used to generate realistic 2D- and 3D-geological models. A modelling workflow is then applied to efficiently turn outcrops of intruded rocks into synthetic seismic images, both in 2D and 3D, and to perform sensitivity analyses. The study highlights which impact a change in dominant frequency has on the detail-level for intrusions in seismic data, this without and with contact aureoles, two types of the latter being tested in the 2D cases. The contact aureoles lead to lowered reflection amplitudes and influence how the reflections of the intrusions are resolved, i.e. a strong combined reflection and/or individual ones, and thus add to the list of factors complicating the imaging of igneous intrusions. The obtained results demonstrate that the seismic expression of intrusions may vary from case to case, i.e. dependent on local factors, and that seismic modelling should aid interpretation of real seismic data. This study also opens the door for more comprehensive 3D modelling of igneous intrusions, especially by including detailed contact aureoles.



## Acknowledgements

I would like to use the opportunity to thank a number of people who supported both scientifically and personally in order to build this thesis. First of all, I want to express my sincere gratitude to my main supervisor Isabelle Lecomte (UiB) for all the feedback, discussion, help and guidance during the last one and a half years. I would also like to express my appreciation to my co-supervisor Christian Haug Eide (UiB) for always being available for feedback, guidance and discussions. A special thanks to co-supervisor Kim Senger (UNIS) for guidance and feedback, especially related to my fieldwork session, and for providing valuable data for this thesis. In addition, I would like to thank UNIS for additional funding for this project.

Thanks to Simon Buckley (NORCE) for providing the lidar-dataset for this thesis, and NORCE for the academic license to the software LIME. A special thanks to NORSAR for the use of academic license to NORSAR Software Suite and SeisRoX. Thanks to Schlumberger for the academic license to Petrel, and thanks to Emerson for the academic license to RMS. Thanks to Peter Betlem and Line Klausen for providing assistance in the field at Svalbard, it would not been possible without you.

I would also like to thank my fellow students at the department of earth sciences for five memorable years. A special thanks to my friends in “Team Bergen” for making these years extraordinary through discussions and great field trips.

To my family, thank you for the encouragement, care and support during the work of this thesis, it is highly appreciated.

Finally, I would like to thank Olea for always being there for me.



---

Sondre Hagevold  
Bergen, June 2019

# Table of contents

<b>Abstract.....</b>	<b>I</b>
<b>Acknowledgements.....</b>	<b>III</b>
<b>1 Introduction .....</b>	<b>1</b>
<b>2 Geological framework .....</b>	<b>4</b>
<b>2.1 Tectonic setting and study area .....</b>	<b>4</b>
<b>2.2 Lithostratigraphy.....</b>	<b>4</b>
2.2.1 Permian .....	7
2.2.2 Triassic.....	8
2.2.3 Jurassic .....	9
2.2.4 Cretaceous.....	11
<b>2.3 The High Arctic Large Igneous Province (HALIP) and Diabasodden Suite.....</b>	<b>12</b>
<b>3 Theoretical background.....</b>	<b>14</b>
<b>3.1 Intrusion emplacement and geometry .....</b>	<b>14</b>
<b>3.2 Contact-metamorphic aureole .....</b>	<b>18</b>
<b>3.3 Seismic expression of igneous intrusions and associated contact aureole.....</b>	<b>20</b>
<b>4 Data and methods.....</b>	<b>23</b>
<b>4.1 Virtual outcrop models.....</b>	<b>23</b>
4.1.1 Virtual outcrop model from lidar-data .....	23
4.1.2 Virtual outcrop models from photogrammetry .....	24
4.1.3 Building of virtual outcrop models from photogrammetry.....	26
<b>4.2 Geological 3D modelling .....</b>	<b>30</b>
<b>4.3 Elastic properties.....</b>	<b>33</b>
<b>4.4 Seismic modelling.....</b>	<b>35</b>
4.4.1 From outcrop to synthetic seismic - seismic modelling workflow for 2D-models .....	36
4.4.2 From outcrop to synthetic seismic – seismic modelling workflow for 3D-model .....	37
<b>5 Results .....</b>	<b>38</b>
<b>5.1 Virtual outcrop models.....</b>	<b>38</b>
5.1.1 Interpretation of lidar-model .....	38
5.1.2 Interpretation of virtual outcrop models from photogrammetry.....	42
<b>5.2 2D geological models – input for 2D modelling.....</b>	<b>43</b>
<b>5.3 3D geological model – input for 3D modelling .....</b>	<b>47</b>
<b>5.4 Seismic modelling of 2D-models .....</b>	<b>49</b>
5.4.1 Changing the dominant frequency.....	49
5.4.2 Including a contact aureole.....	54
<b>5.5 Seismic modelling of 3D-model.....</b>	<b>58</b>
<b>6 Discussion .....</b>	<b>66</b>

<b>6.1</b>	<b>Comparison of outcrop models from photogrammetry vs. lidar-data .....</b>	<b>66</b>
<b>6.2</b>	<b>Limitations in geological models and associated elastic properties .....</b>	<b>67</b>
<b>6.3</b>	<b>Seismic modelling.....</b>	<b>70</b>
6.3.1	Change of dominant frequencies .....	70
6.3.2	Effect of contact metamorphism – one zone vs. several inner layers in zone .....	72
6.3.3	Comparison between 2D- and 3D synthetic seismic.....	75
<b>7</b>	<b><i>Conclusions and further work</i> .....</b>	<b>76</b>
7.1	<b>Further work.....</b>	<b>77</b>
	<b><i>References</i>.....</b>	<b>78</b>

## 1 Introduction

Igneous intrusions are important for basin dynamics and hydrocarbon systems, but can be difficult to map in seismic data due to a complex geophysical character, e.g. both high and low amplitudes and steeply dipping features. Large-scale geological mapping of an area is often done by interpreting seismic data. The seismic imaging potential of intrusions varies, as it is dependent on several factors and intrusions may affect the imaging potential of other units. Geological interpretation of an area is often performed by integrating several types of data to reduce risk, but because the scales of each dataset can vary, it can be difficult to relate interpretations from one dataset to another. This difference between scales, “the resolution gap”, is important to constrain in order to reduce risk and give a valid interpretation, especially for exploration and reservoir characterization. Well-data provide some constraints, but it is limited spatially. Outcrop analogues are therefore studied in order to understand the geology that may be present in the seismic data. Seismic modelling of outcrop analogues and its features can provide the needed constraint to close the resolution gap. This modelling can help to identify features that should be able to be identified on seismic data, by providing a link between field observations and their expression in seismic data (e.g. Eide et al., 2018; Rabbel et al., 2018).

Seismic modelling is known to be cost-efficient, dependant on the methods used, and to provide valuable insight for seismic interpreters (Lecomte et al., 2016). Synthetic seismic is created based on a geological model built with, e.g. the interpretation of a digital outcrop model as basis (Lecomte et al., 2016). Laser scanning (lidar) can create such digital outcrop models (Buckley et al., 2008a; Buckley et al., 2008b; Rittersbacher et al., 2014), or by photogrammetry, which is more cost efficient (Westoby et al., 2012). These two methods capture field data in high detail and act as a base for a 3D photorealistic model of the mapped area, which allows for geological interpretation (Lecomte et al., 2016). Seismic modelling studies are especially targeted at geological features with a complex geometry that are poorly or less understood in seismic reflection data, with the aim to be able to identify their seismic expression more easily. Such features can be igneous intrusions, sand-injectites, hydrothermal vents and fault-complexes.

This thesis will focus on seismic modelling of igneous intrusions and their associated contact aureole emplaced within host rocks, at Botneheia in central Spitsbergen, Svalbard. The large size of these features combined with detailed models make it possible to study how they are imaged in seismic data. The Svalbard archipelago consists of several islands and it is the outcropping part of the north-western Barents Sea Shelf, showing an extensive record of the geology in the region (Worsley, 2008). The Barents Sea Shelf is a well-known region for hydrocarbon exploration and production, and outcrops onshore Svalbard can therefore act as field analogues (Worsley, 2008).

Igneous intrusions are common in extensional basins and at rifted margins, often associated with large igneous provinces (Skogseid et al., 1992; Planke et al., 2005; Magee et al., 2016; Schofield et al., 2017). One such province is the High Arctic Large Igneous Province (HALIP), which consists of Late Mesozoic igneous rocks. The HALIP is present on Svalbard and is referred to as the Diabasodden Suite (Dallmann, 1999). The Diabasodden Suite is a group of geochemically distinguishable doleritic intrusions and the studied intrusions at Botneheia are a part of this group (Dallmann, 1999; Senger et al., 2014b). Igneous intrusions can have various architecture and connectivity, mainly due to factors in place during the emplacement of magma, e.g. stress-regime, host rock lithology and structure (Magee et al., 2016). Igneous intrusions are often part of an interconnected network of magma transport collectively referred to as sill-complexes, where a combination of mainly lateral and some vertical magma transport exists (Smallwood & Maresh, 2002; Planke et al., 2005; Magee et al., 2016; Schofield et al., 2017; Eide et al., 2018). Igneous intrusions are commonly known to have a strong velocity and density contrast from sedimentary host rocks and are therefore often identified as high amplitude reflections in seismic data (Smallwood & Maresh, 2002; Planke et al., 2005). These properties can also make it challenging to interpret underlying units due to shallow absorption of energy and high frequencies by the intrusions (Eide et al., 2018). Nevertheless, Rabbel et al. (2018) presented intrusions with low amplitude reflections, which are in contrast to the common high amplitude characteristic of intrusions. The geophysical response of igneous intrusions should therefore be studied with regards to the local factors in the studied area, such as host rock lithology, fracturing and alteration (Rabbel et al., 2018).

Igneous intrusions can have a strong effect on basin dynamics, related hydrocarbon systems, and CO<sub>2</sub>-storage. (Lecomte et al., 2016; Eide et al., 2018; Rabbel et al., 2018). Intrusions can influence maturation, trap, seal and reservoir of a potential hydrocarbon system (Senger et al.,

2017). This influence can both enhance or diminish the petroleum potential and it is therefore of interest to study intrusions and their architecture from a hydrocarbon perspective (Lecomte et al., 2016; Senger et al., 2017). Following this, intrusions may affect CO<sub>2</sub> capture and storage potential, as a reservoir, seal, trap etc., needs to be in place and function in order to store CO<sub>2</sub>. Seismic modelling of intrusions are of general interest, as there are several problems connected to their seismic imaging (Rabbel et al., 2018). Many sills are namely too thin to be identified in seismic reflection data, thus a large quantity of the sills actually present may not be recognised when interpreting volcanic basins (Schofield et al., 2017; Mark et al., 2018). Igneous intrusions are in addition rarely drilled compared to other rocks, due to the uncertain petroleum potential, but also due to challenging drilling-conditions, (Farooqui et al., 2009; Senger et al., 2017; Rabbel et al., 2018). As a result, it can be difficult to constrain the seismic interpretation of igneous intrusions without any well-tie. Therefore, seismic modelling of field analogues can be a method to aid seismic interpretation.

In order to better understand the seismic imaging potential of igneous intrusions and their contact aureole, and to constrain the resolution gap between scales, seismic modelling will be performed on the geological features exposed at Botneheia, central Spitsbergen. This will be done by first creating and interpreting virtual outcrop models. These will then be used to build geological models of Botneheia in both 2D and 3D, which includes the host rock formations and emplaced sills and dykes. Elastic properties from literature and relevant well-data from onshore Svalbard and offshore Barents Sea will serve as input to constrain the geophysical properties of the formations and the intrusions.

The aim of this study is therefore to (1) build 2D and 3D geological models of the intrusions and the host rocks at Botneheia based on high resolution field data, (2) use these models to do detailed seismic modelling in order to understand which details are imaged in 2D- and 3D-seismic data, (3) explore how the implementation of contact metamorphic aureoles affects the imaging of intrusions and (4) discuss the results in light of the previous studies.

## 2 Geological framework

### 2.1 Tectonic setting and study area

The Svalbard archipelago is located between 74 to 81°N and 10 to 35°E, and it is the outcropping north-western part of the Barents Shelf, showing an extensive record of the geology in the region (Figure 2.2.1, a-b) (Dallmann, 1999; Worsley, 2008). The area is positioned south of the passive continental margin bordering the Eurasian Basin of the Arctic Ocean and to the east of the sheared margin between East-Greenland and Svalbard (Figure 2.2.1) (Dallmann, 1999; Worsley, 2008). The study area is located at the Botneheia mountain, central Spitsbergen, on Svalbard (Figure 2.2.1 c).

### 2.2 Lithostratigraphy

Svalbard holds an extensive sedimentary record reflecting the middle Devonian to Early Carboniferous drift from the equatorial zone and northwards to its present location in the Arctic at ~80°N (Figure 2.2.2, a). Sedimentation patterns and climatic conditions varied because of the movement, leading to an interplay of processes over time (Worsley, 2008). Botneheia is mainly comprised by strata of Late Permian to Late Jurassic age (Figure 2.2.2, b), and these host rocks have been intruded by igneous intrusions during the Early Cretaceous. A review of the geological history and the associated lithostratigraphic units and intrusions will be provided below for the units relevant for this study; for further review see Worsley (2008) and Dallmann (1999); (2015).

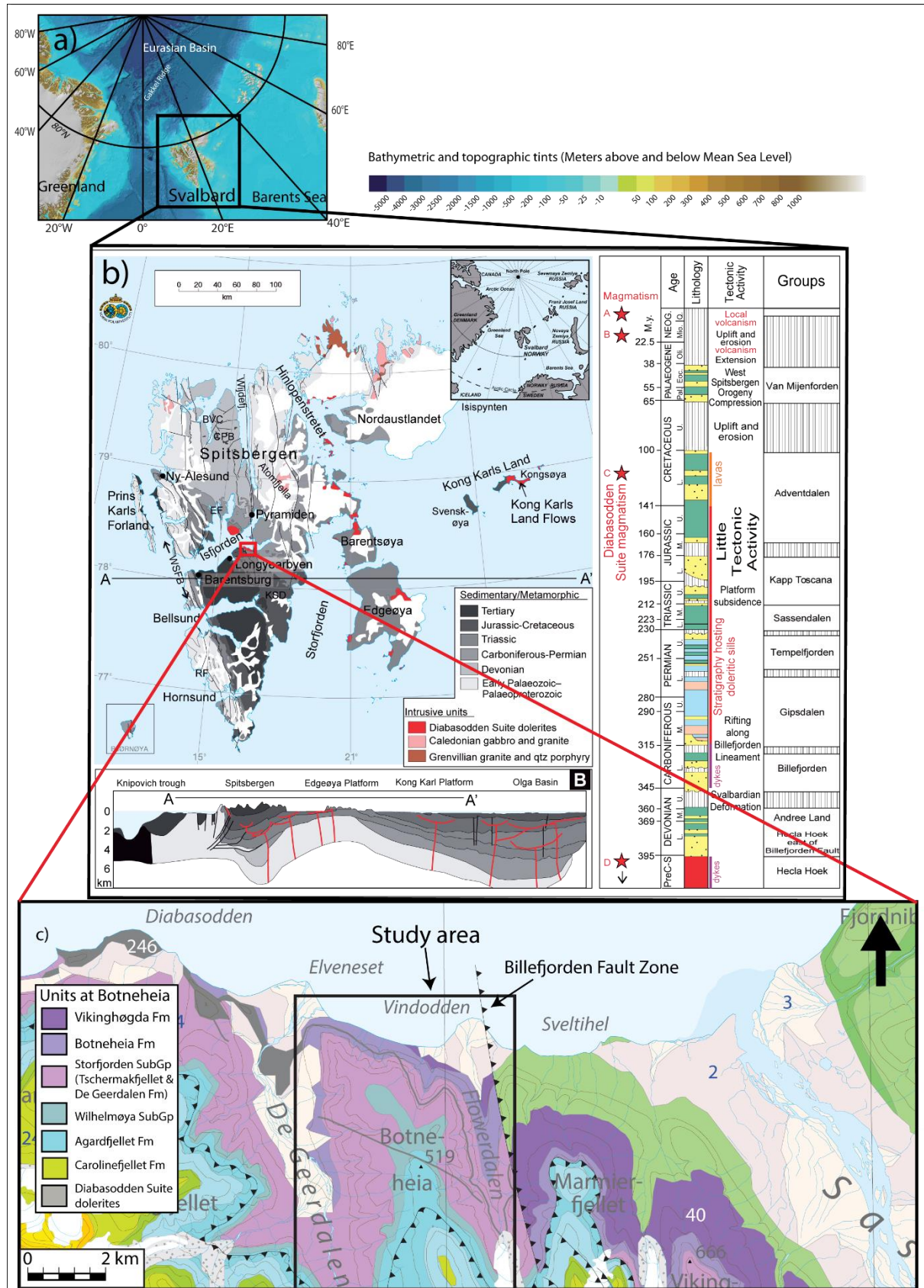


Figure 2.2.1 – Study area. a) Tectonic location of Svalbard. b) Geological map of Svalbard with stratigraphic column and magmatic events. c) Geological map with indicated study area - Botneheia in Central Spitsbergen, showing a legend of units present at Botneheia. Modified from Jakobsson et al. (2012); Senger et al. (2013); NPI (2019).

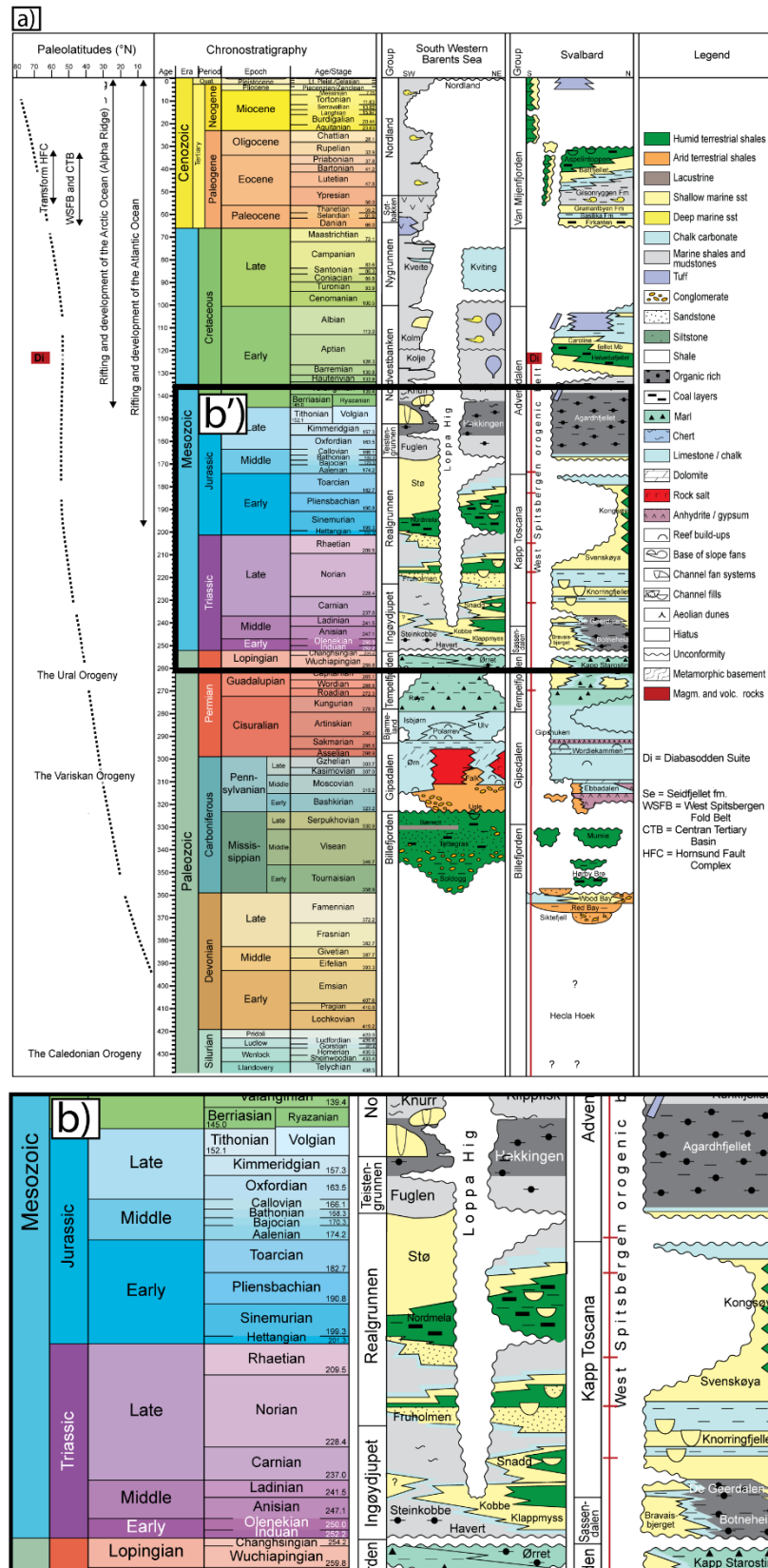


Figure 2.2.2 – a) Litostratigraphic chart of South Western Barents Sea and Svalbard. b) Extraction from “a”, highlighting stratigraphic units exposed in study area Botneheia, also illustrated in (Figure 2.2.1, c). Modified from Festøy (2017).

### 2.2.1 Permian

The Svalbard Archipelago was located at the northern margin of Pangea in Permian (Figure 2.2.3) (Worsley, 2008; Dallmann, 2015). The period is characterised by significant environmental changes, both tectonic and climatic, and the sea level was fluctuating due to glaciations and varying subsidence rates (Worsley, 2008; Dallmann, 2015). The sea level had an overall falling trend, following high levels in the Carboniferous. Due to this trend, the Early to Middle Permian deposits are recognised by carbonates and evaporites, which eventually were subaerially exposed, resulting in weathering and erosion forming a hiatus (Worsley, 2008; Dallmann, 2015). This stop in deposition was later followed by a regional flooding event, allowing clastic sediments to be deposited towards the end of Permian in an open-marine shelf setting (Figure 2.2.3). A mass extinction event caused by a significant increase in global temperatures, combined with the gradual shift from carbonates to a clastic sedimentation marks the Perm-Triassic boundary (Worsley, 2008; Dallmann, 2015).

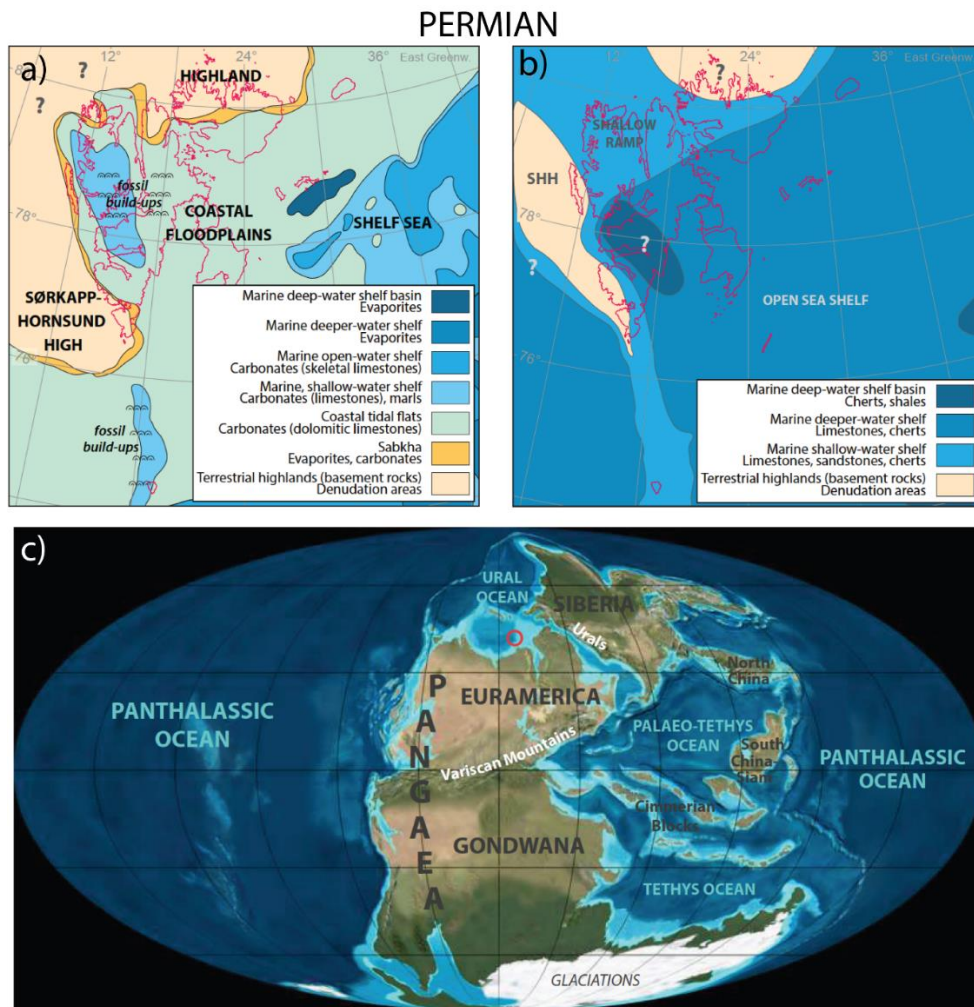


Figure 2.2.3 - Paleogeographic reconstruction of Svalbard's depositional setting in a) Early, b) Late Permian. c) Global paleogeographic reconstruction. Figure modified from Dallmann (2015).

### 2.2.2 Triassic

The Svalbard archipelago was located at around 55°N during most of the Triassic time in an arid and temperate climate, in contrast to the tropical climate during Permian (Dallmann, 2015). The area was part of the North West margin of the supercontinent Pangea, located on the shelf in stable tectonic conditions during the Triassic (Figure 2.2.4). Sediments were extensively filled into the basin and Triassic deposits are outcropping over large parts of Svalbard. The sediments deposited in Early Triassic were mainly sourced from North America and Greenland in the west (Figure 2.2.4, a). The Sassendalen Group was deposited during Early to Middle Triassic and the succession is recognised by significant coarsening upwards sequences reflecting several sea level changes. The Vikinghøgda Formation and the Botneheia Formation are both part of the Sassendalen Group in Central Spitsbergen. The Vikinghøgda Formation consists mainly of shale with some interbedded silt- and sandstone beds, while a black highly organic rich shale characterises the Botneheia Formation. The latter is forming extensive cliffs in Central Spitsbergen and can be traced over large areas (Dallmann, 2015). In addition to the high organic matter (ca. 10%), it also holds significant amounts of phosphate occurring as nodules (Worsley, 2008; Dallmann, 2015). A major shift in depositional pattern occurred entering Late Triassic (Figure 2.2.4, b-c), as sediments were now mainly infilled from the east and south, sourced from the recently formed mountain chain, the Uralides (Figure 2.2.4, d) (Worsley, 2008; Dallmann, 2015). These sediments form the Upper Triassic Kapp Toscana Group, which consists of shallow-marine to deltaic deposits gradually infilling the basin. The lowermost unit, the Tschermakerfjellet Formation, consists of shale and siltstone deposited in a pro-delta environment. This unit gradually goes into the next, the De Geerdalen Formation, time equivalent to Snadd in the Barents Sea, characterised by several coarsening upwards sandstone successions alternating with shale. This unit was deposited in a shallow marine system in the west, while a proximal deltaic environment was prominent in the east, reflected by abundant fluvial channels on e.g. the Hopen island (Klausen & Mørk, 2014). The Kapp Toscana Group thus reflects a large deltaic system prograding north-westward, shown by distal shallow marine deposits on Central Spitsbergen and more proximal deposits on e.g. Hopen and in the Barents Sea (Klausen & Mørk, 2014; Dallmann, 2015). Basin subsidence and sedimentation rates slowed significantly during Late Triassic to Middle Jurassic, forming shallow-marine and inner-shelf environments. As a result, sediments were also reworked leading to mature sandstones and there were events of exposure, leading to several hiatuses throughout this period of time (Worsley, 2008; Dallmann, 2015).

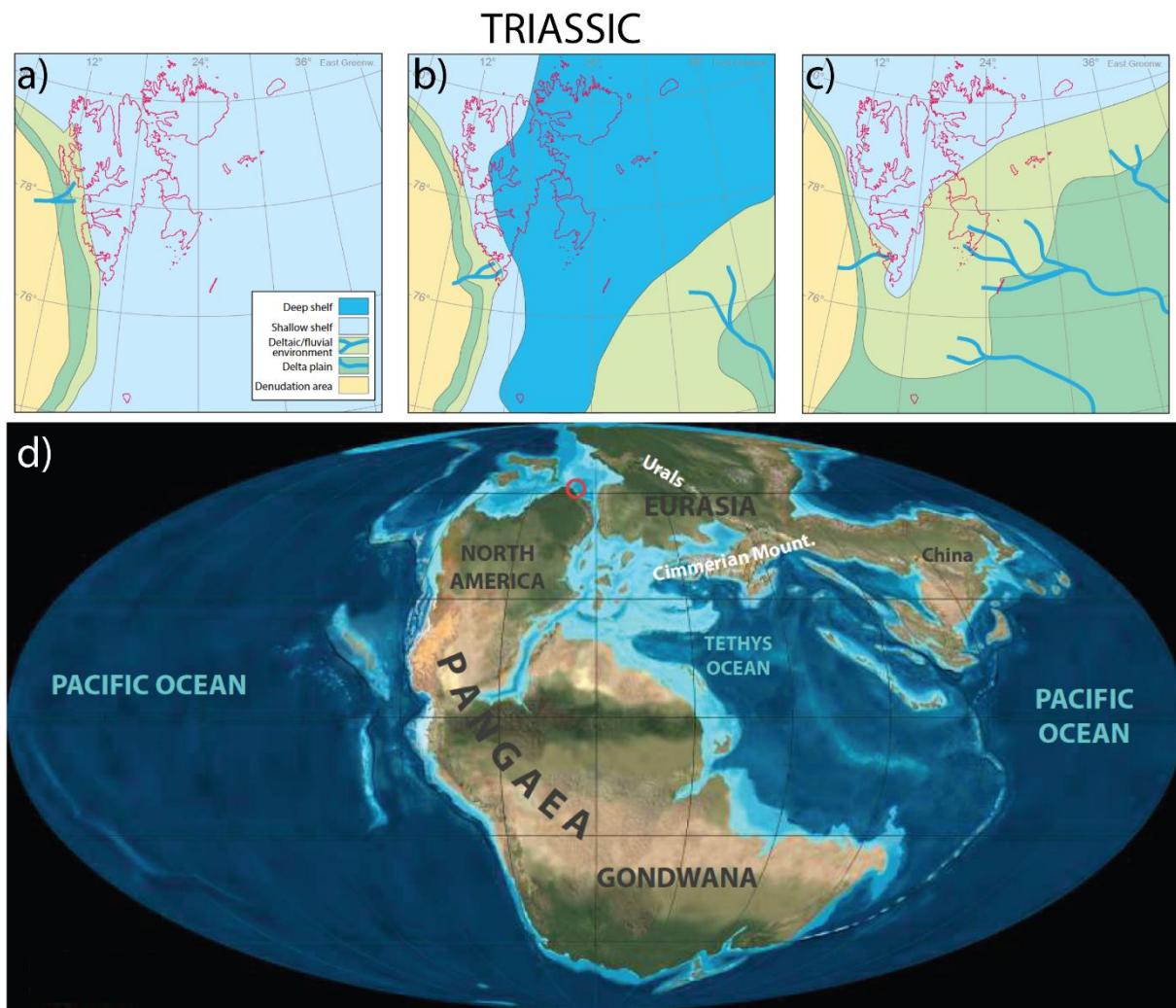


Figure 2.2.4 – Paleogeographic reconstruction of Svalbard’s depositional setting in a) Early, b) Middle, and c) Late Triassic. d) Global paleogeographic reconstruction. Figures modified from Dallmann (2015).

### 2.2.3 Jurassic

Svalbard was still part of the North West margin of Pangea during the Jurassic, but Pangea had now started to break up, dividing the landmasses into two supercontinents (Figure 2.2.5). The climate changed from arid and temperate conditions known from the Triassic, to warm and humid conditions (Dallmann, 2015). Several sea-level changes occurred during the period because of continued plate movement and reorganisation of Pangea. Shales with a high organic content characterise the last part of the Jurassic. These shales were deposited after a significant shift in depositional setting, where it went from shallow-marine to a deep-marine setting due to a global transgression (Figure 2.2.5 a-b). This setting in combination with high atmospheric CO<sub>2</sub> levels made it possible to produce and preserve large amounts of organic matter (Dallmann, 2015). As a result, the organic rich sediments of Jurassic age are the main source rocks for many of today’s oil and gas fields.

### JURASSIC

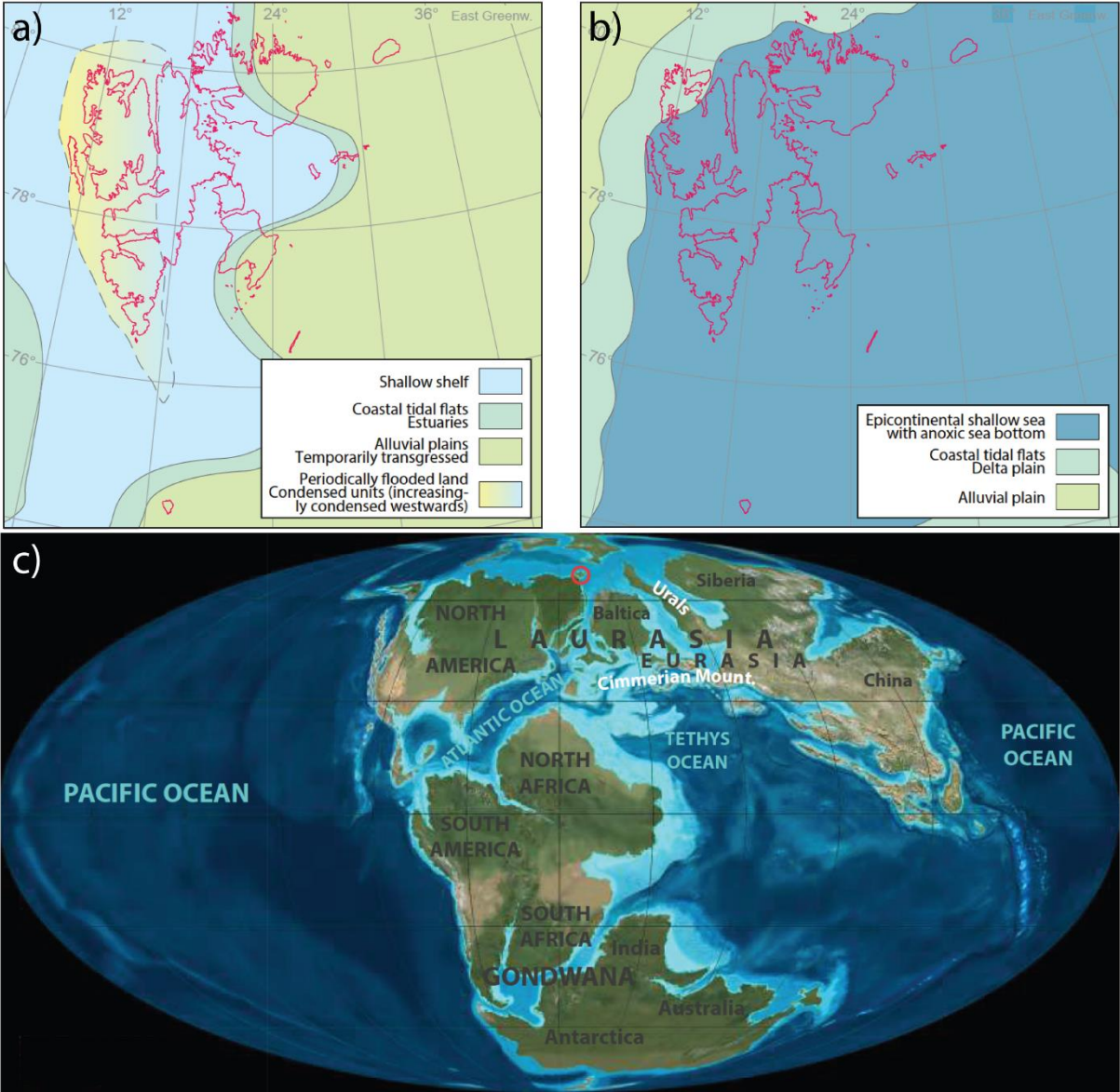


Figure 2.2.5 - Paleogeographic reconstruction of Svalbard's depositional setting in a) Early, b) Late Jurassic, c) Global paleogeographic reconstruction. Figures modified from Dallmann (2015).

### 2.2.4 Cretaceous

The last part of the breakup of Pangea took place in Cretaceous, and Svalbard was now positioned at around 65°N (Figure 2.2.6) (Dallmann, 2015). The early Cretaceous was a time of high volcanic activity, reflected by several igneous rocks found on Svalbard and at the margins of the Arctic Ocean. These igneous rocks are part of the High Arctic Large Igneous Province (HALIP), and these rocks are referred to as the Diabasodden Suite on Svalbard (Dallmann, 1999, 2015).

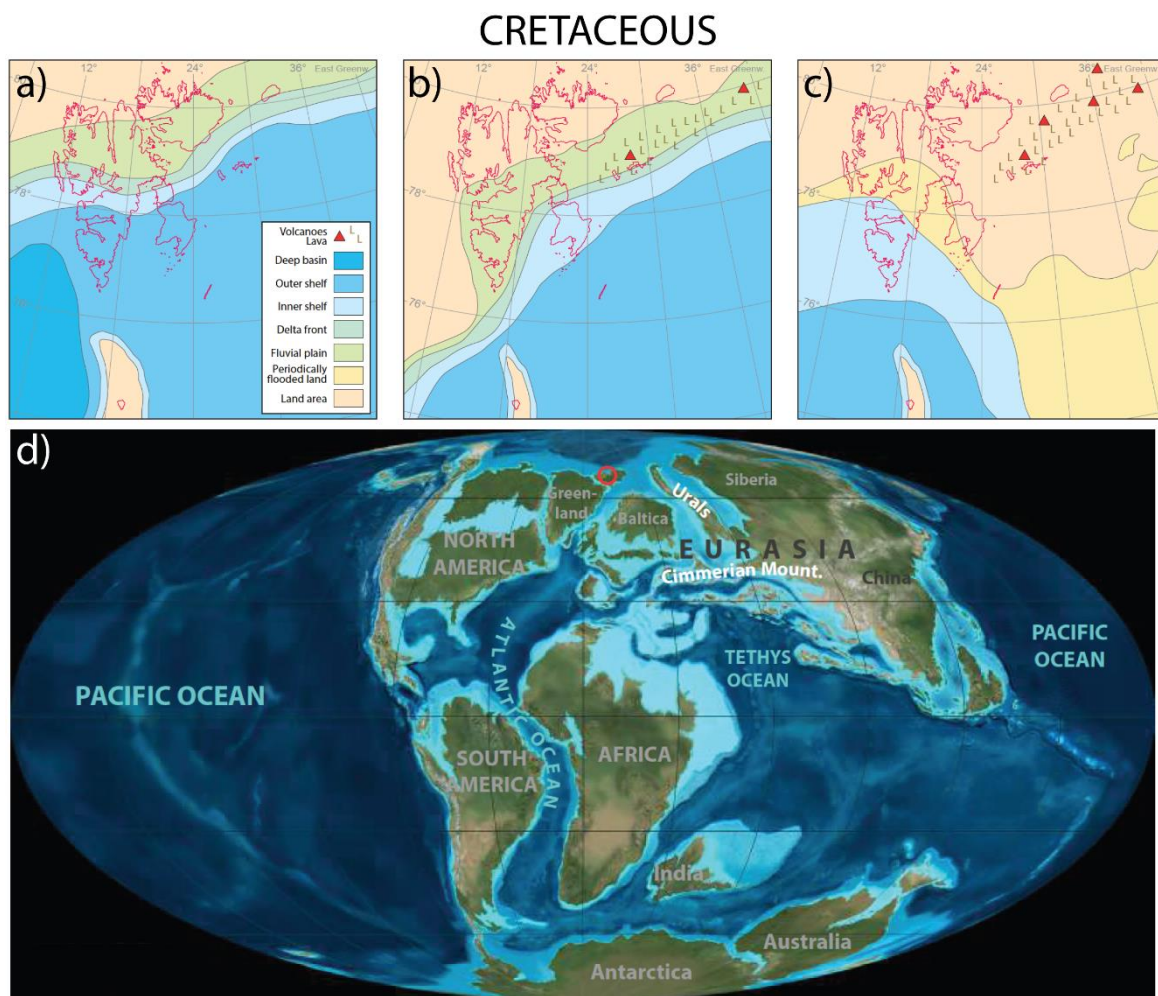


Figure 2.2.6 - Paleogeographic reconstruction of Svalbard's depositional setting in a) Early, b) Middle, c) Late Cretaceous. d) Global paleogeographic reconstruction. Figures modified from Dallmann (2015).

### 2.3 The High Arctic Large Igneous Province (HALIP) and Diabasodden Suite

An area that has been subject to significant igneous activity can be classified as a Large Igneous Province (LIP) if it meets the criteria as defined by Bryan and Ernst (2008). This criteria states: “Large Igneous Provinces are magmatic provinces with areal extents  $>0.1 \text{ Mkm}^2$ , igneous volumes  $>0.1 \text{ Mk}^3$  and maximum lifespans of  $\sim 50 \text{ Myr}$  that have intraplate tectonic settings or geochemical affinities, and are characterised by igneous pulse(s) of short duration ( $\sim 1\text{-}5 \text{ Myr}$ ), during which a large proportion ( $>75\%$ ) of the total igneous volume has been emplaced” (Bryan & Ernst, 2008, p. 177). The High Arctic Large Igneous Province (HALIP) is one such province, first defined by Tarduno et al. (1998), and it represents Lower Cretaceous igneous activity exposed on Franz Josef Land, Svalbard and the Canadian Arctic Islands (Figure 2.3.1) (Maher, 2001). The Diabasodden Suite is a term used for the intrusive rocks found onshore on Svalbard, and they are geochemically linked to the HALIP, which is indicative of a common source (Senger et al., 2014b). This source is believed to be a mantle plume located at the southern end of the Alpha Ridge in the Amerasia Basin (Døssing et al., 2013). The igneous intrusions on Svalbard and its surroundings have affected an area of  $200\,000 \text{ km}^2$  (Maher, 2001). The HALIP and the Diabasodden Suite have been extensively studied due to their potential impact on the petroleum system, but also with regards to paleoclimate and paleoenvironmental effects (Senger et al., 2014b; Polteau et al., 2016). The timing of magma emplacement for the Diabasodden Suite is uncertain as there is a large spread in published ages, as reviewed by Senger et al. (2014b). The majority of the samples have been dated by K-Ar and Ar-Ar dating which gives a long period of magma emplacement, 130-80 Ma, with two distinctive pulses with higher activity, 130-120 Ma and 85-80 Ma, respectively. On the other side, U-Pb dating of a limited number of samples suggests a significant shorter time of magma emplacement, i.e. between 120 and 125 million years ago (Corfu et al., 2013; Senger et al., 2014b; Polteau et al., 2016). It is believed that the method is more robust and probably less uncertain than the K-Ar and Ar-Ar method. The U-Pb ages are therefore given significant weight, even though the number of samples are statistically limited compared to those of the K-Ar/Ar-Ar dating (Corfu et al., 2013; Senger et al., 2014b; Polteau et al., 2016). Polteau et al. (2016) conclude that the large spread in ages given by the K-Ar and Ar-Ar dating most likely is due to alteration. Thus, a short period with rapid magma emplacement is believed to have formed the Diabasodden Suite.

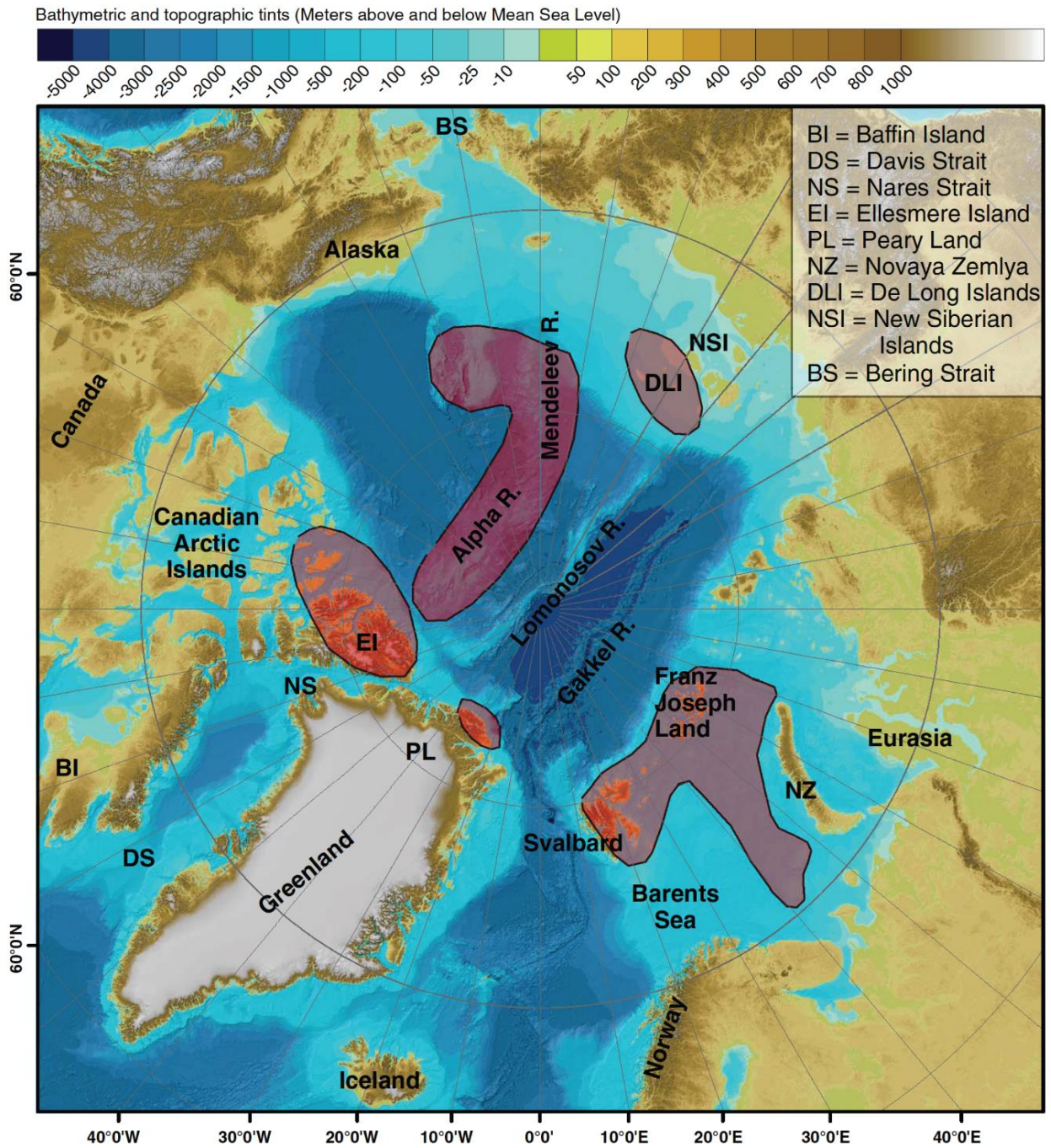


Figure 2.3.1 – The main igneous provinces taking part of the High Arctic Large Igneous Province. Figure from Senger et al. (2014b).

### 3 Theoretical background

Igneous intrusions are often part of large igneous complexes, where a combination of lateral and vertical magma transport exists (Muirhead et al., 2014; Magee et al., 2016). Lateral magma transport takes place through connected sills, dominantly layer parallel to the host rock with some transgressive segments (Malthe-Sørenssen et al., 2004; Magee et al., 2016; Schofield et al., 2017). Vertical magma transport takes place in form of dykes, vertically to sub-vertically cutting through the strata of the host rock (Malthe-Sørenssen et al., 2004; Muirhead et al., 2014). Igneous intrusions often take form as large sheets, which commonly develop through the inflation and coalescence of several separate magma segments (Magee et al., 2018; Galland et al., 2019). The emplacement of intrusions and their associated segments will be described in the following.

#### 3.1 Intrusion emplacement and geometry

The emplacement of an igneous intrusion in a sedimentary succession is largely influenced by the host rock lithology (Schofield et al., 2012). The resulting intrusion geometry is therefore a product of the emplacement mechanism acting at the time of the intrusion, which can be divided into two categories; a brittle or a non-brittle emplacement mechanism (Schofield et al., 2012). Local properties of the host rock, i.e. porosity, mechanical strength and volume of pore-fluids, control if the host rock will be able to be deformed in a non-brittle manner or not. These properties are already controlled by factors such as the burial history of the host rock and its associated diagenesis, cementation and dewatering, prior to magma intruding the rock (Schofield et al., 2012). As these two emplacement mechanisms differ in function, their resulting intrusion structures are distinguishable. One can therefore study the properties of the host rock in combination with the geometries of the intrusions, in order to tell something about the emplacement mechanism that acted at the time of intrusion (e.g. Schofield et al., 2012; Magee et al., 2015; Eide et al., 2017).

Brittle emplacement structures are commonly steps and bridges (Figure 3.1.1, a). Steps are generated from initially offset en echelon fractures that later merge into a single intrusion sheet as fractures propagate due to magma inflation (Figure 3.1.1, a, A-A' – C-C') (Schofield et al., 2012). As a result, the steps make up the previous offset part between the initially segmented intrusions, which are now one connected sheet (Figure 3.1.1, a, C-C'). These steps are

orientated perpendicular to the direction of magma flow and can thus be used to determine propagation direction, if these steps are exposed in an outcrop section. Bridges are generated when two or more sills are intruded slightly offset from one another, on overlapping horizons (Figure 3.1.1, a, A-A'). Continued magma inflation in the sills lead to deformation of the host rock between the sills, resulting in a bent structure called a bridge (Hutton et al., 2009; Schofield et al., 2012). Bridges like this can eventually break, if magma inflation continues and the build-up of stress within the bridge becomes too great for the host rock to withstand, resulting in brittle failure and the formation of a broken bridge as the sills are now linked (Figure 3.1.1 a, B-B'-C-C') (Hutton et al., 2009; Schofield et al., 2012). Both bridges and broken bridges indicate magma flow perpendicular to the outcrop, if seen in an outcrop cross-section (Hutton et al., 2009; Schofield et al., 2012).

Non-brittle emplacement structures commonly occur in host rocks with low mechanical strength and cohesion, e.g. shale (Schofield et al., 2012). In these cases, the host rock will undergo ductile or non-brittle behaviour during magma intrusion, which leads to a viscous-viscous interface between the host rock and the intruding magma, resulting in a lobate morphology (Schofield et al., 2012), also called elliptical magma fingers (Figure 3.1.1, b and c). Each finger correspond to separate segments of a sill and they can eventually coalesce into a larger lobe if magma inflation continues (Figure 3.1.1, b, t1-t3) (Schofield et al., 2012). The overall sheet shape of the sill located behind the segmented fingers is thus a result of the coalescence of fingers (Galland et al., 2019).

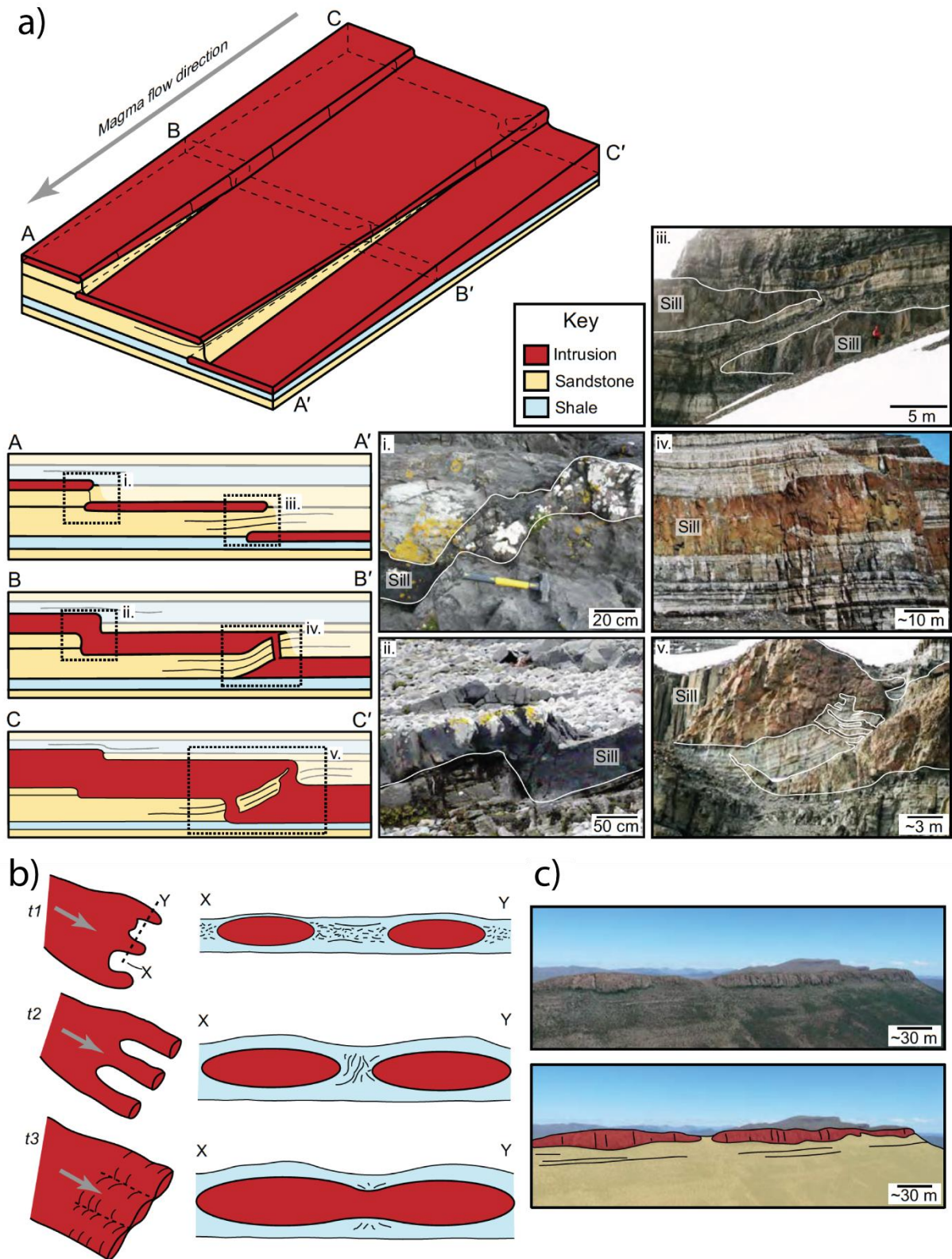


Figure 3.1.1 – Brittle and non-brittle emplacement structures. a) Steps and bridges related to brittle mechanisms, also indicating magma flow direction. Cross-sections A-A' to C-C' show the formation of a bridge and the resulting step, images i.-v. indicates field-examples. b) Formation of magma fingers, 't' is time. c) Fingers visible in an outcrop. All modified from Magee et al. (2015).

Intruding sills can lead to structural doming of the overburden and this deformation is a result of one or more mechanisms acting alone or collectively, forming a dome-shape (Schmiedel et al., 2017). Doming of the overburden may lead to the formation of traps with four-way dip closures, and it can form or destroy stratigraphic traps. Elastic uplift during emplacement is the most common mechanism resulting in dome structures. As there exist several mechanisms of host-rock deformation associated with sill intrusions, they are typically divided into synemplacement- and postemplacement processes (Schmiedel et al., 2017). A sill-associated dome has an amplitude, meaning the height from original position to new deformed position, which relates to the thickness of the intruded sill (Figure 3.1.2). This relationship is close to 1:1 if the dome is a result of syn-emplacement elastic uplift, whilst other post-emplacement mechanism may alter this relationship (Figure 3.1.2, a). A contact aureole surrounding an intrusion may lead to devolatilization, the release of fluids, and this can cause volume reduction of the overburden host rock. Thus, the amplitude of the dome most likely will be less than the thickness of the sill after devolatilization (Figure 3.1.2, c) (Schmiedel et al., 2017). If sedimentation is ongoing and continuing, it may lead to differentiated load and thus differential compaction. The intrusion is strong, i.e. it withstands compression better compared to the host rock, thus the host rock will be deformed as the load of sediments increases. This will cause higher subsidence on the sides of the intrusions, whilst sediments are still deposited on the top of the sill. As a result, the dome structure is enhanced and the amplitude of the dome becomes greater than the height of the sill (Figure 3.1.2, d) (Schmiedel et al., 2017).

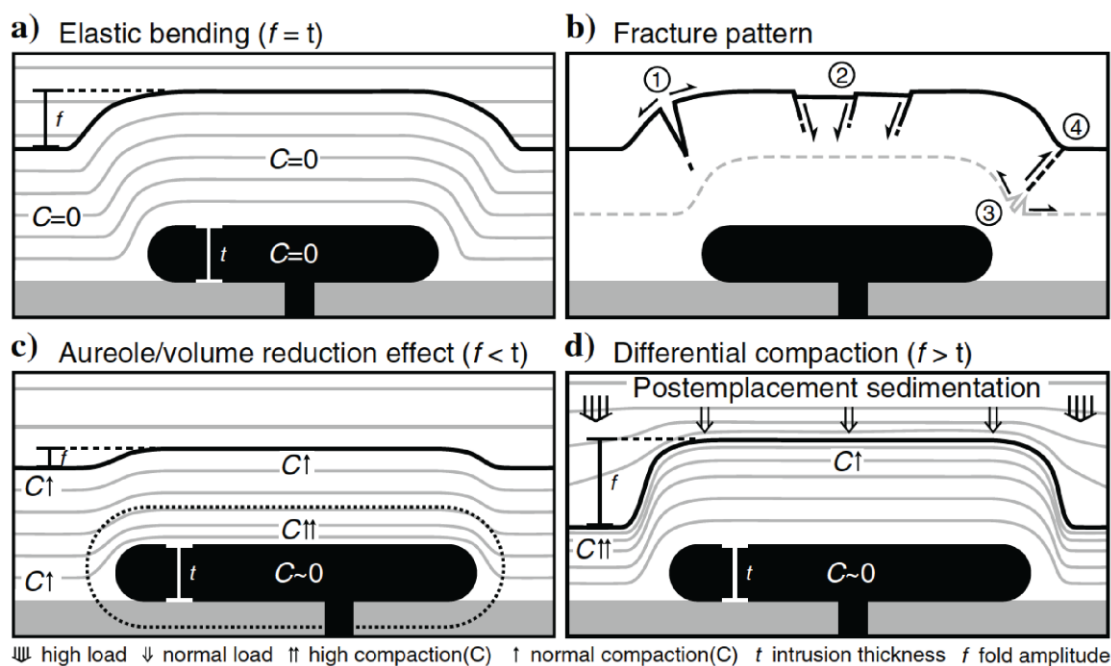


Figure 3.1.2 – Four models illustrating doming of overburden due to the emplacement of a sill. From Schmiedel et al. (2017).

## 3.2 Contact-metamorphic aureole

Igneous intrusions are influenced by the host rocks they enter, e.g. due to mechanical strength, fracture patterns, fault zones, but host rocks are also affected by intrusion activity. Intrusions affect the host rock by developing contact-metamorphic aureoles due to the high temperature of the melt, which commonly is higher than 1100°C (Senger et al., 2014a). The contact aureole surrounds the intrusion, and its thickness is defined as the zone with a higher degree of metamorphism than the unaffected background rock, measured from the intrusion contact (Aarnes et al., 2010). The contact aureole thickness may vary from 30% to 200% of the sill thickness, depending on the temperature of the intrusion and host rock during emplacement in addition to the sill thickness (Aarnes et al., 2010).

The contact aureole has several local alteration effects on the properties of the host rock due to physical-chemical reactions (Senger et al., 2014a). The aureole will lead to a loss of total organic content (TOC) towards the intrusion, in addition to devolatilization, compaction and density changes (Aarnes et al., 2010; Senger et al., 2014a). As a result, these effects may have a significant effect on petroleum prospectivity. It could lead to maturation of a source rock in a under-mature basin, thus increasing prospectivity, or it could lead to over-maturation in an already mature basin (Senger et al., 2014a; Senger et al., 2017). The contact aureole may also induce mineral dehydration, decarbonation and host rock melting (Aarnes et al., 2010). Mineralization of the host rock in the affected zone leads to a high electrical resistivity with large variations (Figure 3.2.1) (Smallwood & Maresh, 2002). However, the mineralogical changes are not significant enough to change the main composition of the rock, and the aureole is therefore not seen on the gamma ray (Figure 3.2.1) (Smallwood & Maresh, 2002). These local alterations may lead to increased fracturing in the zone surrounding the intrusion, which again can have an effect on porosity and permeability of the host rock. In total, the contact aureole leads to significant changes for the host-rock in the affected zone. Thus, the log-response of the contact zone will also differ from the unaffected host rock (Figure 3.2.1). The compaction, a reduction in TOC and a reduction in porosity will overall lead to an increased Vp and density (Figure 3.2.1) (Senger et al., 2014a; Aarnes et al., 2015). Both the Vp- and

density-log drop adjacent to the intrusion, which is believed to be a result of increased fracturing adjacent to the sill (Planke et al., 1999; Smallwood & Maresh, 2002).

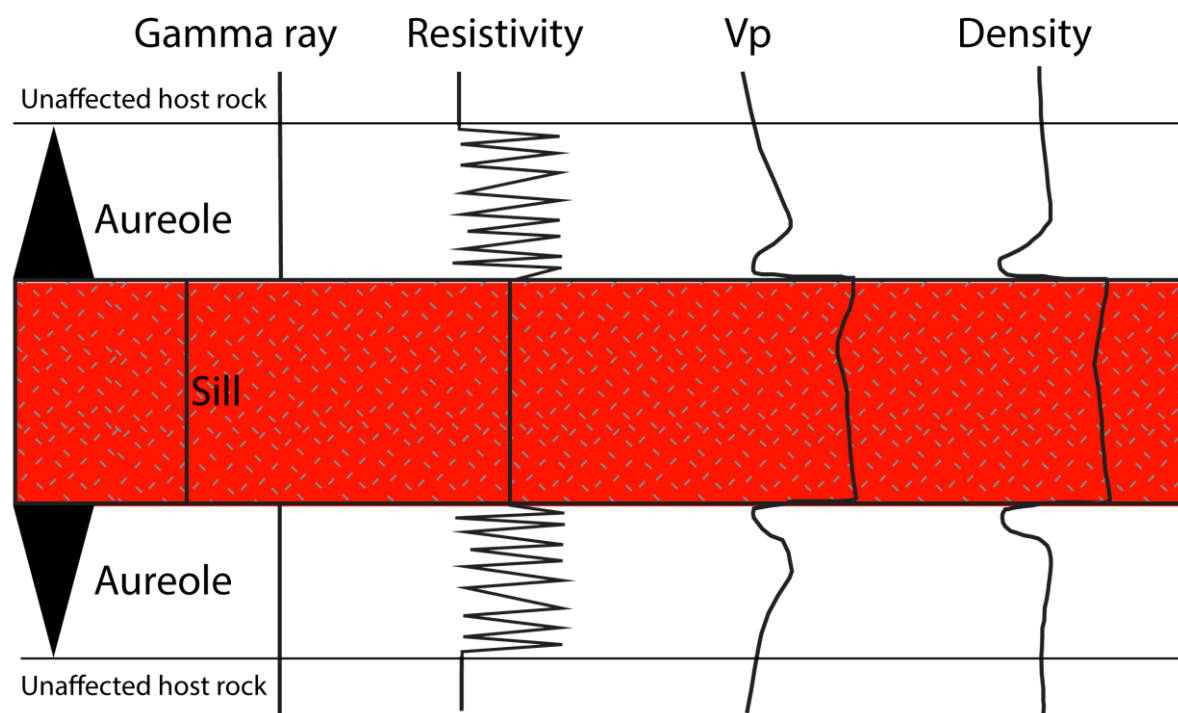


Figure 3.2.1 – Schematic summary of log responses around sills, showing typical variations in gamma ray-, resistivity-, sonic- and density-logs. This example is modified from Smallwood and Maresh (2002).

Igneous intrusions and their associated contact metamorphism have also effects on the regional scale of the area in which they intrude. Intrusions can act as a seal, or a migration pathway, clearly affecting the transport of fluids within the intruded host rock. In addition, they can compartmentalise potential reservoirs, or they could enhance vertical fluid flow, by allowing fluids to flow through fractures of intrusions and acting as a pathway (Schofield et al., 2017; Senger et al., 2017). This is influenced by secondary processes such as weathering, as weathering increases porosity and permeability in fractures, allowing for enhanced flow across an intrusion (Senger et al., 2014a). For example: a dyke cutting through a potential source-, cap- and reservoir-rock may enhance the probability for the hydrocarbons to flow to the reservoir by acting as a pathway, or it may form barriers/seals if it is unfractured. In addition to this, intrusions and their associated contact aureoles have the potential to affect global climate through devolatilization and the following release of gases during emplacement (Aarnes et al., 2010).

### 3.3 Seismic expression of igneous intrusions and associated contact aureole

The seismic expression (i.e. amplitude, thickness in time and architecture) of igneous intrusions is dependent on several parameters such as the velocity, frequency, thickness of intrusion, type of host rock and the acoustic impedance contrast. Velocity ( $v$ ) and frequency ( $f$ ) control the wavelength ( $\lambda$ ), i.e.  $\lambda = v/f$ , hence the resolution (Simm & Bacon, 2014). The thickness of an intrusion affects whether it is uniquely resolved or not as this is dependent on the resolution, e.g. if it is below seismic resolution, it will not be imaged. The type of the host rock relates to the lithological nature of the rock, e.g. if it is interbedded or homogeneous (Magee et al., 2015). Acoustic impedance (AI) is the product of velocity and density, thus the contrast in AI from one unit defines reflectivity. Intrusions in sedimentary basins are commonly recognised in seismic data as high amplitude reflectors, easily distinguished from the surrounding host rock due to the strong contrast in AI (Smallwood & Maresh, 2002; Planke et al., 2005). However, intrusions may also be represented by low amplitude reflections due to influencing local factors, i.e. host rock lithology, fracturing and alteration, or due to a more silicic mineralogy of the intrusions. The seismic response of igneous intrusions should therefore be studied with respect to the local factors and stratigraphy in the study area (Rabbel et al., 2018).

Igneous intrusions reflect and absorb seismic energy, especially the high frequencies. In addition, the high velocity layer of the intrusion will deflect the incoming rays, causing a steep focused path for the rays as they exit the intrusion (Eide et al., 2018). Lateral resolution is a function of velocity and frequency (as for vertical resolution) but also including illumination, i.e. max dip of imageable strata. A steep and focused ray-path below a high-velocity layer leads to a low lateral width for the span of ray-paths and a reduction in max dip (Eide et al., 2018). Consequently, this effect leads to a lower lateral resolution below the sill, and in addition, the loss of high frequencies further worsens the resolution. As a result, shallow intrusions can make it challenging to interpret underlying strata and/or intrusions, as they become poorly imaged or not imaged at all (Smallwood & Maresh, 2002; Magee et al., 2015; Eide et al., 2018). This involves steep intrusions, i.e. dykes, multiple intrusions appearing to be one and tuned reflector packages (Eide et al., 2018). This effect becomes more significant at greater depths and can lead to underestimation of sill volume, uncertainty in interpretation of sill architecture and sill thickness (Schofield et al., 2017; Eide et al., 2018).

Seismic resolution needs to be addressed to better understand issues with seismic imaging of geological features, i.e. intrusions (Figure 3.3.1). There is a limited range of frequencies available in seismic surveys, which leads to limitations in the lower limit of bed thicknesses that may be uniquely resolved, known as vertical resolution (Simm & Bacon, 2014). The vertical resolution is commonly estimated to be one-quarter of the dominant wavelength ( $\lambda/4$ ) (lateral  $\lambda/2$ ), but this is dependent on the wavelet shape (Kallweit & Wood, 1982; Simm & Bacon, 2014). A wavelet is a seismic pulse of energy, which is the response of a reflector, i.e. an interface between layers with contrasting acoustic impedance. The shape of a wavelet may differ, and the Ricker-wavelet is one type with a distinct shape (Ricker, 1940). The Ricker-wavelet is a zero-phase wavelet, i.e. it has a peak aligned at time zero (Simm & Bacon, 2014). In relation to this, tuning thickness also needs to be addressed, which is the thickness of the bed that makes two events indistinguishable in time (Widess, 1973; Kallweit & Wood, 1982). As a result, two events below the tuning thickness will appear as one event with a higher amplitude (Figure 3.3.1), while the same events with a greater thickness than the tuning thickness will be resolvable as two separate events (Eide et al., 2018).

Seismic detectability is also an issue when it comes to imaging igneous intrusions in seismic reflection data. It relates to whether a reflection from a unit can be identified or not, in this case, igneous intrusions. Seismic detectability is a more complex issue to address compared to vertical resolution, as there are more factors in play (Eide et al., 2018). A seismic reflection is commonly detected when its amplitude can be distinguished from the surrounding reflections (Simm & Bacon, 2014). The amplitude of the reflection is a result of a contrast in acoustic impedance, which is a function of velocity and density. Rock properties may vary due to several factors, i.e. mineralogy, compaction, alteration, fractures, thus the elastic properties such as P-wave ( $V_p$ ) and S-wave velocities ( $V_s$ ) and density will also be affected. Detectability is also dependent on the signal-to-noise ratio of the seismic (Simm & Bacon, 2014). Rules of thumb for seismic detectability is therefore difficult to constrain for general use and should rather be individually addressed for each case (Eide et al., 2018). Seismic modelling of igneous intrusions of mafic composition (dolerites) are the main target in this study, and they are commonly known to have higher density and  $V_p$ , compared to intrusions of felsic composition. As a result, the contrast to the surrounding siliciclastic host rock will be greater than what it would have been had the intrusions been felsic (Eide et al., 2018). This can increase the detectability of dolerites, and it can lead to detectability of thinner intrusions than what the general rules of thumbs address, but with a poor vertical resolution, hence the risk of constructive/destructive

interferences with the surrounding. In reality, boreholes still encounter more sills than what are detected in the associated seismic datasets of the area in which the borehole penetrate (Schofield et al., 2017). Thus, seismic interpretation alone can result in an underestimation of the volume and the distribution of the sill complex.

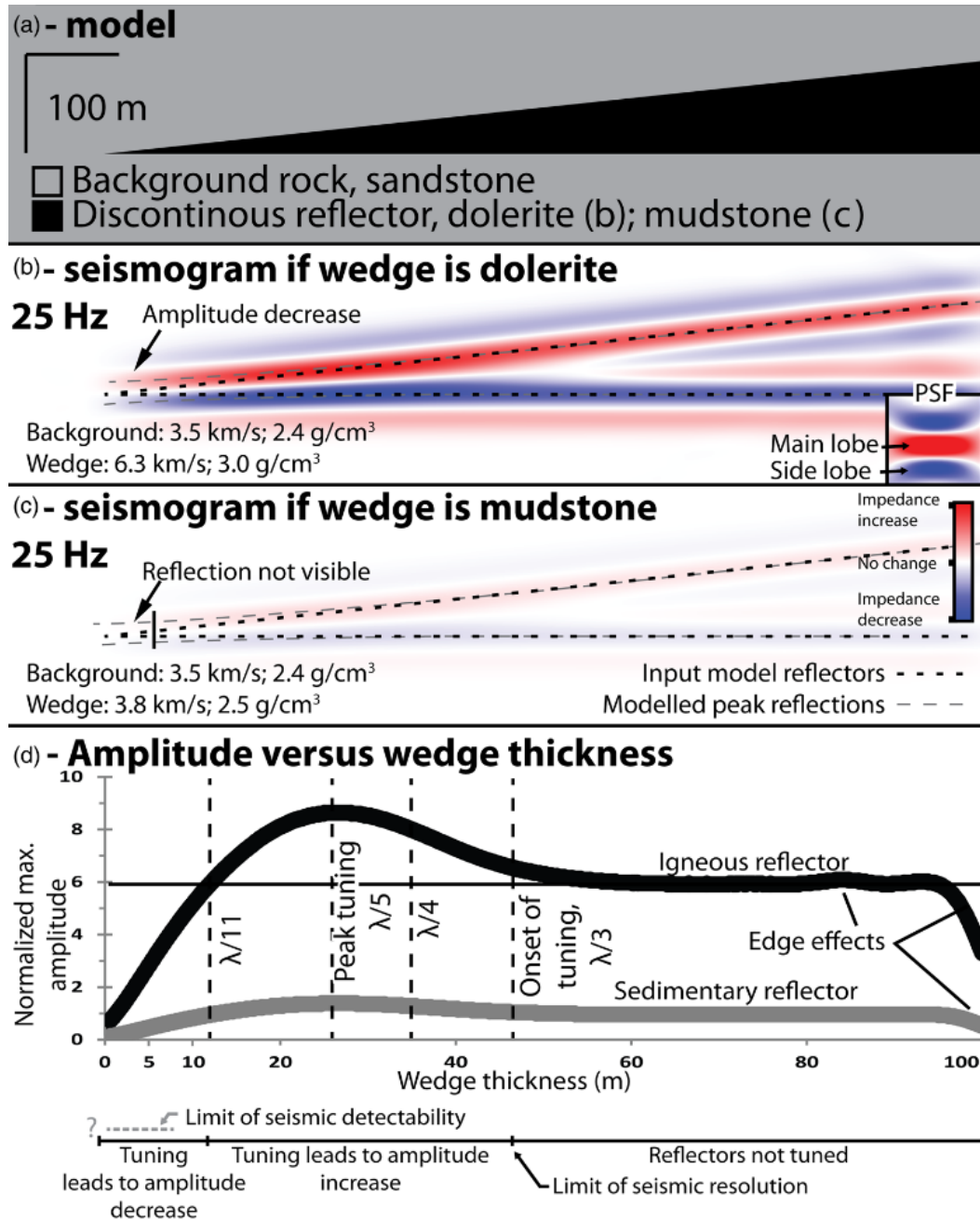


Figure 3.3.1 – Wedge model presenting the concepts of seismic resolution, seismic tuning and seismic detectability (Eide et al., 2018). a) Input model, b) Resulting seismic image at 25 Hz for a wedge consisting of dolerite, top and base reflectors are resolved from wedge thicknesses from 100 m to 45 m, while the amplitude increases and thickness is overestimated from 45 m to 12 m due to seismic tuning before a rapid drop from 12 m to 0 m. c) Seismic image at same conditions as for b), for a wedge consisting of mudstone, showing a decreased amplitude compared to b) and lack of visible reflections below 10 m. d) Graphs illustrating maximum amplitude per trace for b) and c). Figure from Eide et al. (2018).

## 4 Data and methods

Several virtual outcrop models of Botneheia in Central Spitsbergen, Svalbard, are the main data for this thesis, with a size of  $\sim 10 \text{ km}^2$ . One of these is a high-resolution virtual outcrop model based on data previously collected by lidar (Light Detection And Ranging) scanning. This model covers the main areas of interest of Botneheia, but some areas have poor coverage and photos were therefore collected by photogrammetry in the field during the present work. Photogrammetric image collection is based on capturing overlapping photos, from which it is possible to calculate the unique 3D location of points that are present on all overlapping photos, relative to the camera position (Bemis et al., 2014). The photos were gathered by an “unmanned aerial vehicle” (UAV), i.e. a drone, and a handheld “digital single-lens reflex camera” (DSLR) during autumn 2018 with the aim to build new virtual outcrop models, which can aid the interpretation of the lidar-model.

Geological interpretation of the virtual outcrop models was carried out to identify the geometries of the igneous intrusions, in addition to map the main formation- and facies-boundaries present in the outcrop. This interpretation is performed in the software LIME for all of the models described further below (Buckley et al., 2019). The geological interpretation is the fundament for building several 2D-models, and one 3D geological model, representing the outcrop as realistic as possible.

These models are then assigned elastic properties in order to do seismic modelling with the aim to investigate how igneous intrusions are imaged, first in 2D, then in 3D. The data and methods will be described in further detail below.

### 4.1 Virtual outcrop models

#### 4.1.1 Virtual outcrop model from lidar-data

The virtual outcrop model from a helicopter-based lidar-survey is part of the main dataset of this thesis. This model was acquired and built prior to this work, and is the courtesy of the Virtual Outcrop Geology group at NORCE. A lidar-survey collects point-clouds by laser scanning, and digital images with a camera, which are then processed over several steps to form a virtual outcrop model (Buckley et al., 2008a; Buckley et al., 2008b). Lidar-scanning is geometrically accurate and allows for a high spatial resolution. Lidar-scanning is thus highly

applicable for geological purposes, as geology is studied on both detailed and larger scales. The Botneheia mountain has cliff-sides with a horizontal extent of 5-6 km and a height of ~ 500 m above sea level, and the outcrop data were collected by a helicopter-based system. The data were gathered by Helimap Systems AG in August 2009 at the western, northern and parts of the eastern side of the Botneheia. The system used for the survey was a laser scanner, (Riegl LMS VQ-480, average point spacing of ~ 0.5 m) and a high-resolution digital camera (Hasselblad H3DII-50 50MP, 35 mm lens, pixel size 6.0  $\mu\text{m}$ ) which are both obliquely mounted on the helicopter to best capture the outcrop exposure (Buckley et al., 2008a; Senger et al., 2013). The virtual outcrop model resulting from this survey has an image resolution of ~ 0.07 m and allows for high-resolution interpretation of the exposed geological features.

#### **4.1.2 Virtual outcrop models from photogrammetry**

One week of fieldwork at Botneheia during September 2018 culminated in four new virtual outcrop models, in order to assist the lidar-model where it is missing outcrop data. This fieldwork focused on photographing the outcrop with cameras with a built in Global Navigation Satellite System (GNSS), with the aim to build virtual outcrop models from photogrammetry. Ground-based photos shot normal to the outcrop with a DSLR-camera (Nikon D5300 – Sigma 50mm f/3.5) covered the majority of the steep cliffs. The photos were shot at a distance from the outcrop so that both top and bottom of Botneheia were within the frame. One set of photos from the DSLR covers the northern side of Botneheia and this set was captured from a boat. The inaccessible parts of the mountain were covered with an UAV, (DJI Mavic Air) with a digital camera of 12MP and a 35mm f/2.8 lens.

The photos were shot so that they overlap with one another, which is key for being able to stitch them together into a virtual outcrop model. For the DSLR, this was done by shooting one photo straight at the outcrop and two or more overlapping photos slightly on the sides of the first photo, and then moving 10-50 m parallel to the outcrop before doing the same. This was repeated until the whole outcrop was covered with overlapping photos. The same practice followed for the drone, but it was only used for the inaccessible parts of the mountain, and/or the parts that were more interesting to cover in higher-detail. The flying-time for the drone was very limited due to cold weather reducing the battery capacity. As a result, the DSLR photos covered the majority of the mountain.

Approximately 4700 high-resolution, georeferenced photos were taken, and these were filtered and processed into 3D virtual outcrop models using AgiSoft PhotoScan Professional 1.4.2. Photos with poor quality and non-relevant photos were manually sorted out. The remaining photos were then imported to AgiSoft PhotoScan, where they were filtered on image quality, where photos with a quality below 0.5 were rejected. The virtual outcrop models created from photogrammetry are all built by following the workflow illustrated in the flowchart below. Internal settings for each step of the workflow may vary, as different numbers of photos in the models affect the quality in which the computer can process.

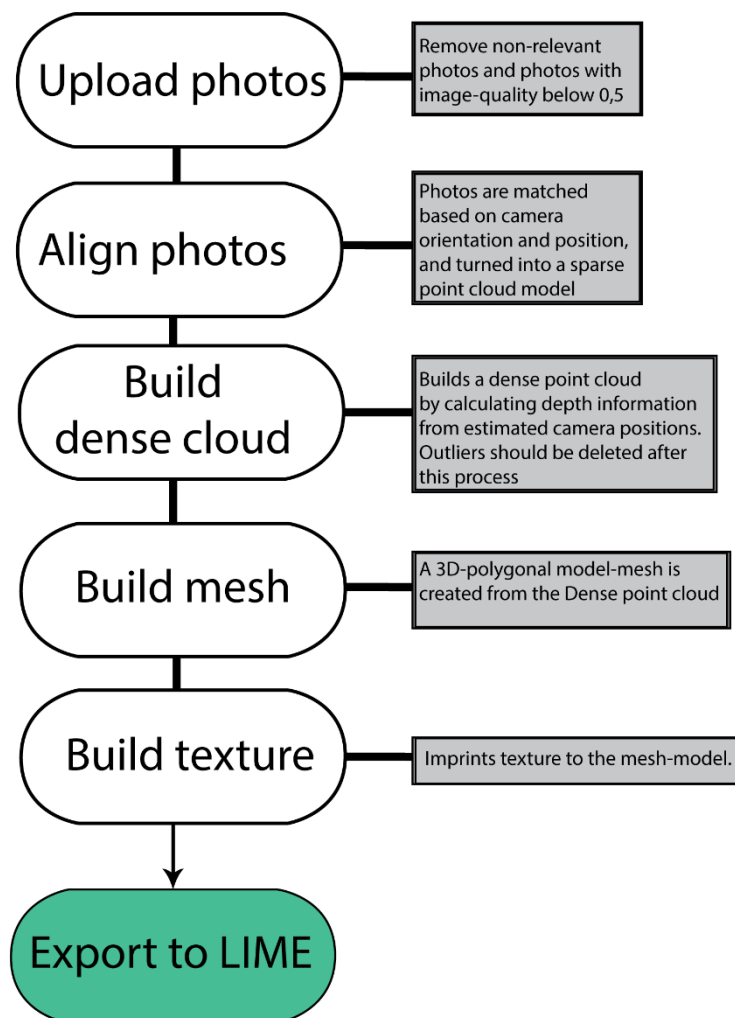


Figure 4.1.1 – Workflow for the creation of virtual outcrop models in AgiSoft Photoscan.

### 4.1.3 Building of virtual outcrop models from photogrammetry

Significant time was spent on building new virtual outcrop models from photogrammetry based on photos collected during fieldwork autumn 2018. The aim was to build a more complete outcrop model of Botneheia, as data were missing on the eastern and northern side of Botneheia in the lidar-model. The build resulted in four models in total; two large overview outcrop models of the whole mountain, one model covering a dyke visible at the top part of the mountain, and one highly detailed model of the well exposed northern side of Botneheia.

The large model illustrated in Figure 4.1.2 clearly shows the extent and geometry of Botneheia. The outcrop sections are clear and one can interpret intrusion geometries and major formation and/or facies boundaries on all sides of Botneheia. It also provides valuable information for areas without data in the lidar-model. Parts of the model are disconnected and/or overlapping (Figure 4.1.4, a), this was addressed by manually merging and realigning the model by placing markers, i.e. a point attached to an item that is present on several overlapping photos. This led to a well-aligned model in the area in which the method was applied (Figure 4.1.4, b), but the method was inefficient and imprecise, it was thus discarded. Nevertheless, the virtual outcrop models from photogrammetry provides excellent datasets that can aid the interpretation of the lidar-model, and they are thus highly valuable for further geological modelling in this study.

There is a dyke visible on top of Botneheia, with an extent diagonally from the western side facing “De Geerdalen” to the eastern side and in to Flowerdalen (Figure 4.1.2). The dyke is covered with photos in the east and west where it pops out of the mountain, indicated in Figure 4.1.2. A detailed virtual outcrop model was built for the dyke where it shoots up from De Geerdalen in the west towards the top of Botneheia (Figure 4.1.3).

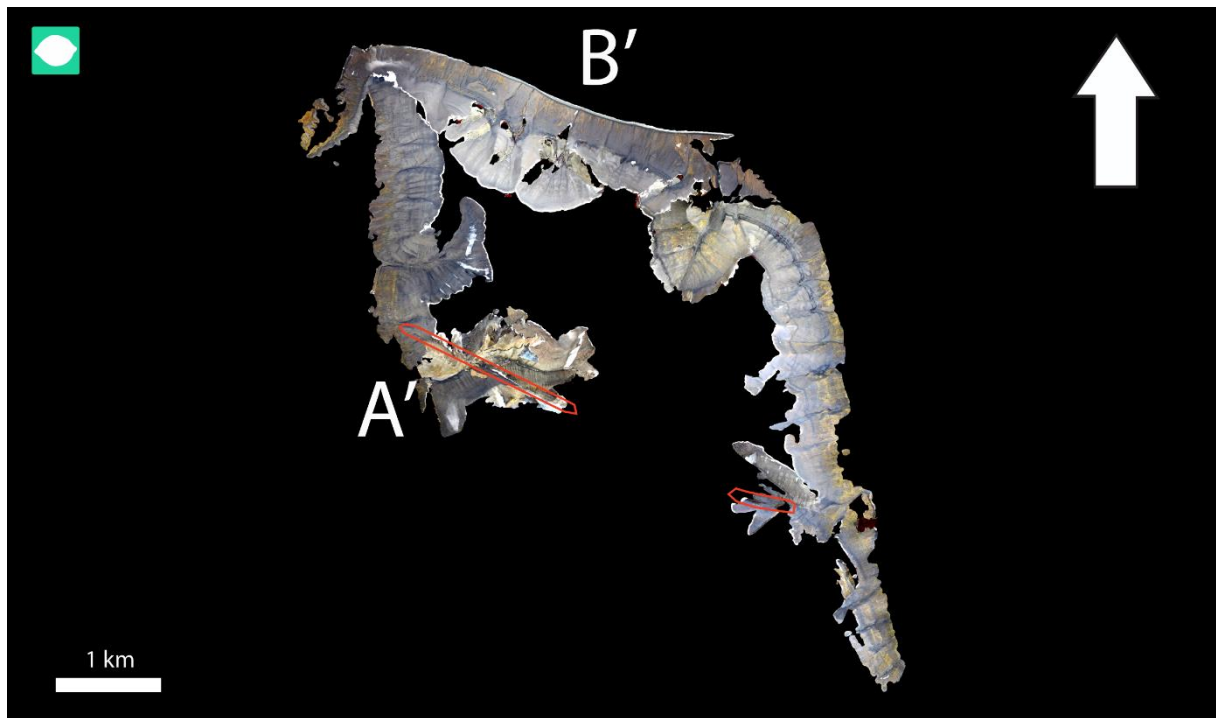


Figure 4.1.2 – Model number 1., covering all of Botneheia, viewed from above. Red circles indicate areas in which the dyke on top of Botneheia is visible. A' refers to Figure 4.1.3 while B' refers to Figure 4.1.5.

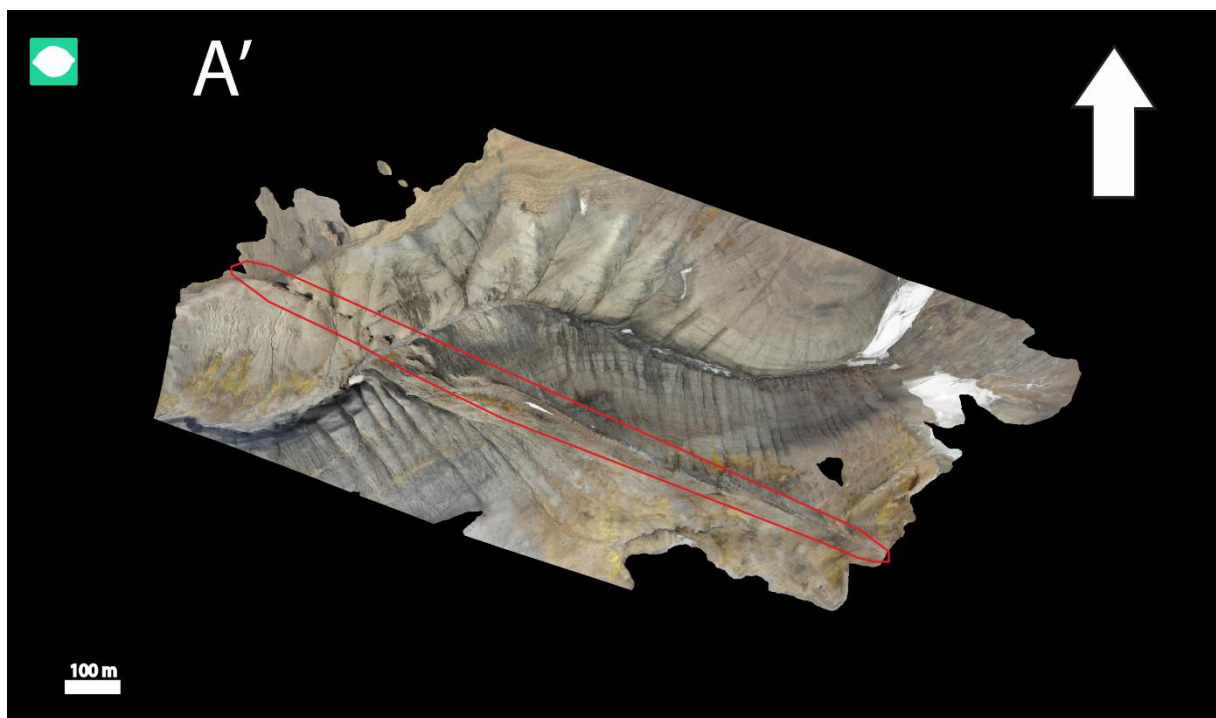


Figure 4.1.3 – Virtual outcrop of dyke (circled) on top of Botneheia, viewed from above. Location indicated on Figure 4.1.2.

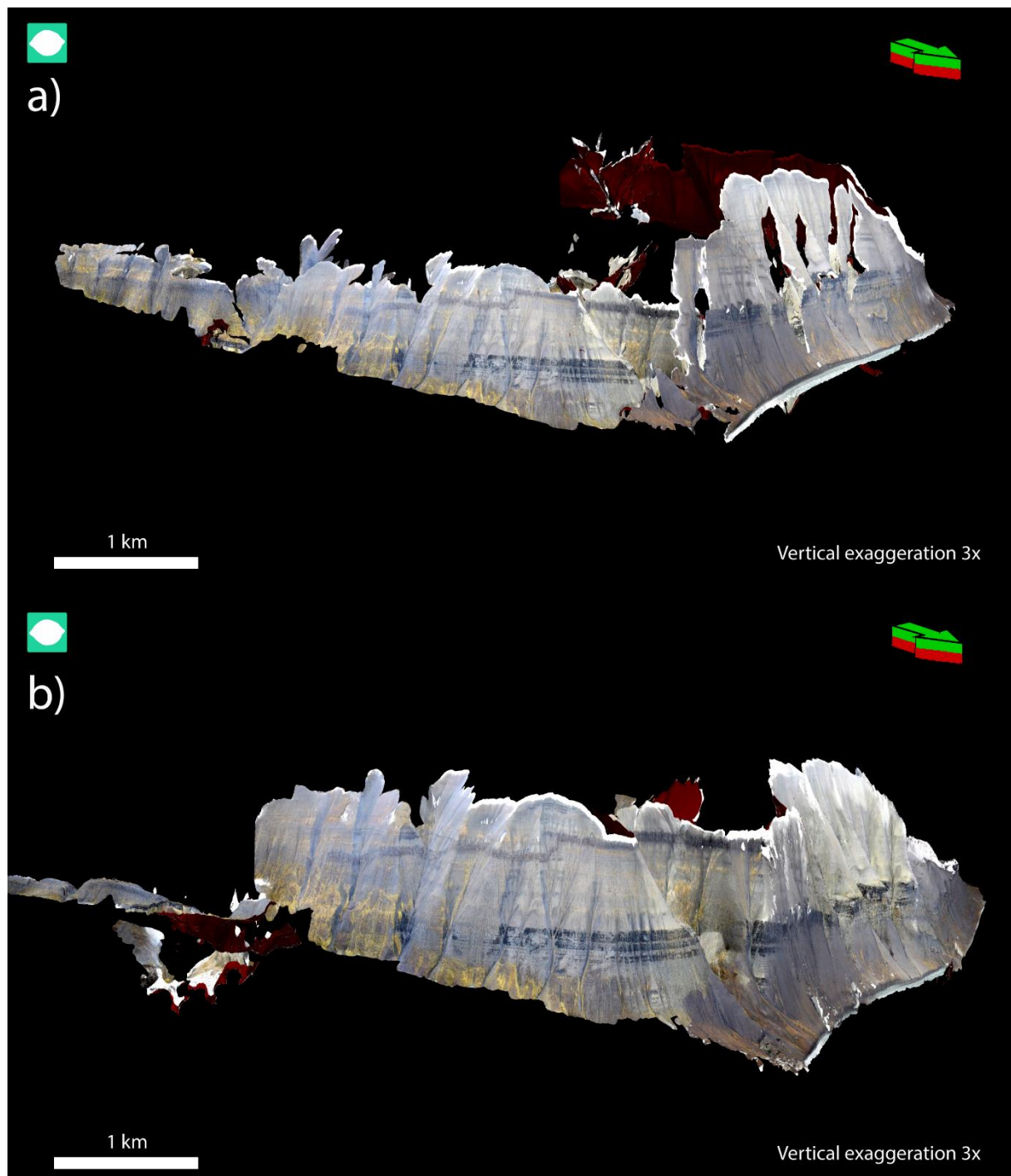


Figure 4.1.4 – Comparison between model nr. 1 (a) and model nr. 2 (b). Model 2 is merged with the use of markers, resulting in a better aligned, but smeared section on the northern side of Botneheia, to the right in the figure, while the part in the far left is mismatched.

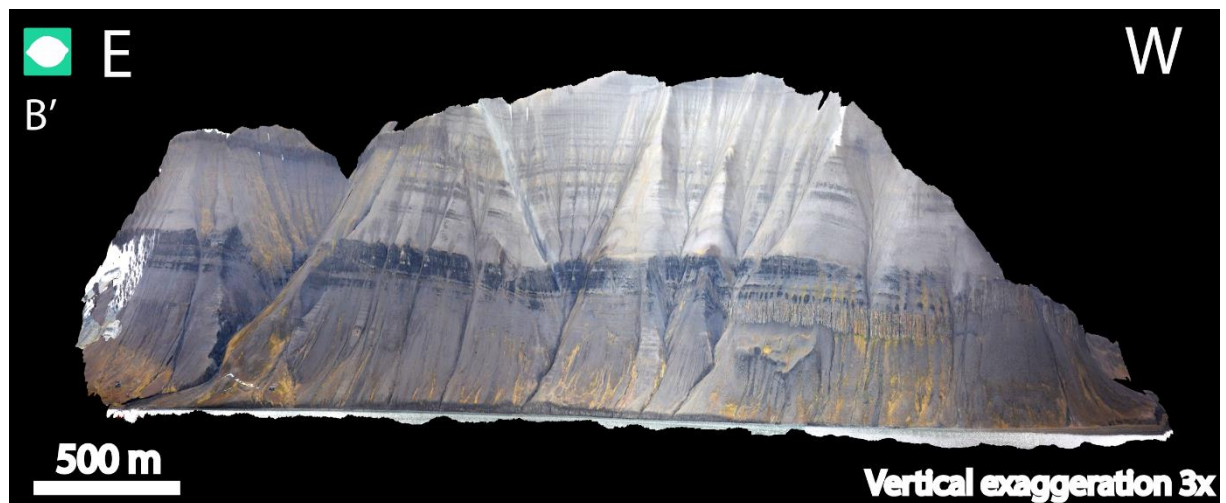


Figure 4.1.5 – Virtual outcrop model of well-exposed northern side of Botneheia. Location is indicated on Figure 4.1.2.

The high detail model of the northern side of Botneheia shows a well-exposed outcrop section, showing important formation boundaries, stratigraphic variation and most important – intrusion geometries (Figure 4.1.5). It also provides coverage of the bottom part of the cliff, which, as mentioned, is missing in the lidar-model. As a result, this particular model is important for constraining the intrusion geometry in this part of the mountain for further geological modelling.

## 4.2 Geological 3D modelling

The virtual outcrop models were visualised and interpreted in LIME (Buckley et al., 2019), with the aim to (1) map the geometries of the igneous intrusions, (2) identify main formation boundaries and (3) map facies boundaries if possible. The interpreted models were then used to build a gridded simplified geological model of Botneheia by following the steps below. Significant time and effort were necessary to build this model due to the comprehensive steps involving manual work.

- Export of the Botneheia formation boundary and intrusion geometries interpreted in LIME, from lidar-model, and imported these as lines to Petrel.
- Import polylines of detailed intrusion geometries from virtual outcrop model (from ground based photos), from the lowermost part of the northern side of Botneheia, as this was not imaged in the lidar-model.
- Move the lowermost interpreted intrusions geometries spatially in Petrel in order to fit with lines from lidar-model by manually editing the coordinates. This is done by calculating the difference in spatial offset.
- Add points to the Botneheia Formation polyline in Petrel in order to extend the interpretation into areas without data. These points are placed spatially based on thematic and topographic maps of Svalbard from the NPI (2019) with mapped formation boundaries.
- Create a surface based on the Botneheia formation polyline, using a convergent interpolation algorithm, with an increment of X, Y; 5, 5. The boundary is set from input and extended with 100 nodes.
- Create surfaces for the remaining formation boundaries by using the *Calculator* in Petrel and the Botneheia surface as reference by adding or subtracting the height difference based on measurements of formation thickness in virtual outcrop model.
- Create a grid by using the *Make simple grid* process in Petrel. Surfaces of the formation boundaries are used as input data.
- Select the 3D Model in Petrel and edit *Corner point gridding - Layering process*, select *Follow base* for the zones and defined *Cell thickness* of 5 m.
- Facies are modelled in zones by adding sand, fine sand, shale, organic rich shale and intrusion as facies types.

- Facies are modelled in Petrel in the zone “Top De Geerdalen Fm – Top Tschermakfjellet Fm” by setting the background to shale. Sand is set to a fraction of 50% with an elliptical geometry, with a horizontal distance of minimum 1500 m, mean 3000 m and maximum 6000 m.
- Facies are modelled by Petrel in the zone; Top Tschermakfjellet Fm – Top Botneheia Fm, by setting the background to shale and fine sand of 3% with an elliptical geometry, with a horizontal distance of minimum 1500 m, mean 3000 m and maximum 6000 m.
- Facies are modelled by Petrel in the zone; Top Botneheia Fm – Top Vikinghøgda Fm, by first dividing the zone into two, where the upper zone within the Botneheia Fm was filled with the facies organic rich shale, while the lower zone was filled with the facies shale.
- The remaining facies type, i.e. intrusion, is manually drawn, in RMS, as the *Facies editing tool* proved more efficient than the *Facies tool palette* in Petrel. The model was therefore exported and imported between RMS and Petrel several times in Recue format in order to do this.
- The geometry of the intrusions was drawn in by filling in the intrusion polylines interpreted in LIME. These polylines are exposed on the northern side (Figure 4.2.1, b) of Botneheia and the eastern side (Figure 4.2.1, c). The intrusion geometries were manually extrapolated in the lateral extent for every Z-slice of the model (Figure 4.2.1, a).
- The model is imported back to Petrel in order to assign elastic properties such as  $V_p$ ,  $V_s$  and density, by assigning a constant value to each facies.
- The 3D model is exported to NORSAR Software Suite by using the *NORSAR Plugin* in Petrel, in order to do seismic modelling.

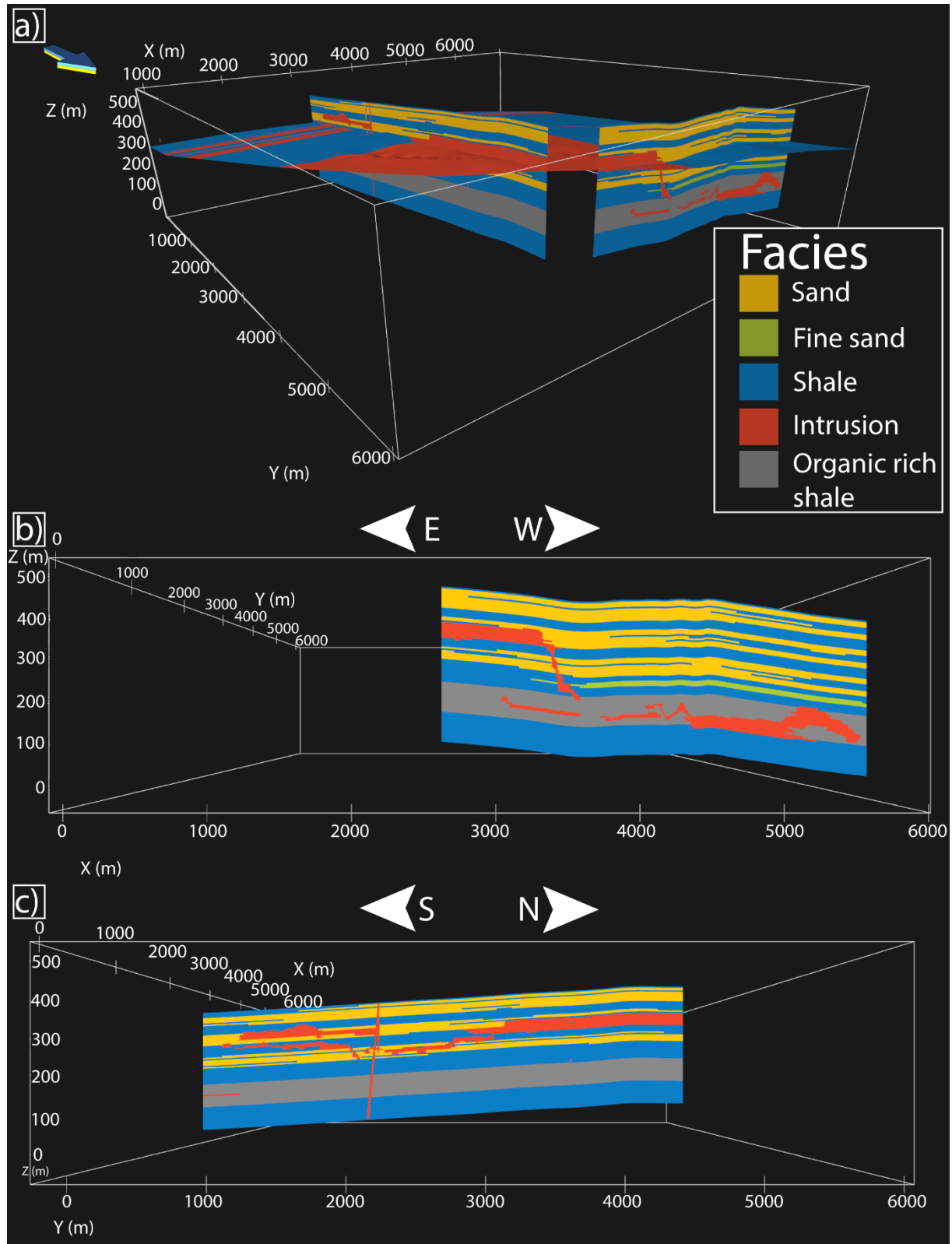


Figure 4.2.1 – 3D geological model representing Botneheia, viewed in RMS. a) Overview of the model, showing one slice in each direction; b) northern side of Botneheia, c) eastern side of Botneheia.

### 4.3 Elastic properties

The geological units at Botneheia need elastic properties, i.e.  $V_p$ ,  $V_s$  and density in order to do seismic modelling. These properties vary along with rock properties and they are therefore different from one unit to another. Data gathered from an offshore well (7222/1-1) from the western Barents Sea Shelf were used to populate the model with elastic properties. This well has been selected because it penetrates rock formations that are time equivalent to those found onshore at Botneheia. The resulting seismic will therefore illustrate how the outcrop and its geological features could be imaged in seismic if it was located subsurface.

Values for  $V_p$  and density have been picked by doing an average of the property in a certain interval in which a time equivalent formation and associated facies exist. For example, a sand in De Geerdalen formation at Botneheia is assigned an average  $V_p$  for a sand interval of 5 m in the corresponding Snadd formation in well 7222/1-1. The same was done for density.  $V_s$  is commonly not given, and it is therefore often calculated by using a  $V_p/V_s$ -ratio from relevant literature.  $V_p$  for the igneous intrusions at Botneheia was picked from well 7715/3-1 located onshore Svalbard, which penetrates a 62 m thick intrusion. The  $V_p/V_s$ -ratio for the igneous intrusions has been set to 1.86, and density to  $3.0 \text{ g/cm}^3$ , as given in Smallwood and Maresh (2002).

There is a relationship between the  $V_p/V_s$ -ratio and lithology, and the ratio is also affected by rock properties such as porosity, pore fluid and degree of consolidation (Mjelde et al., 2003). Sandstones and shales are commonly associated with a ratio of (1.65-1.75) and (1.7-3.0), respectively (Mjelde et al., 2003). The degree of consolidation increases with burial depth, leading to a lower  $V_p/V_s$ -ratio. As the units at Botneheia have been buried at a depth of  $>3 \text{ km}$  and later been uplifted due to erosion of the overburden, the  $V_p/V_s$ -ratio would have been affected by these events, and a proper estimation of the ratio may be complex. Nevertheless, the focus in this study is how the intrusions and their architecture would be imaged if they were located subsurface, thus Botneheia act as an analogue. A  $V_p/V_s$ -ratio of 1.7 has therefore been set for the sedimentary units, as this is within the intervals given by Mjelde et al. (2003) and similar to  $V_p/V_s$ -ratios in other studies (c.f. Flesland, 2017; Eide et al., 2018; Friestad, 2018).  $V_s$  is thus estimated in this study, but it will not affect modelling in this work, because this study will only model a zero offset case, i.e. normal incidence on the reflectors, for simplicity. In this case,  $V_s$  does not have an effect as all energy is conserved as P-waves. Consequently,

the reflection coefficient in this study is dependent on the contrast in acoustic impedance, i.e. the product of density and  $V_p$ , but as  $V_s$  is also estimated, the model will be ready for non-offset modelling as well.

Smallwood and Maresh (2002) illustrated a typical log response of an igneous intrusion and its associated contact aureole (Figure 3.2.1). The contact aureole is recognised by a gradual increase and a following sudden drop in elastic properties above and below the intrusion. In order to model the contact aureole surrounding the intrusions at Botneheia, values have been picked from log-data with a similar response to that of Smallwood and Maresh (2002), for the intrusion in well 7715/3-1. The contact metamorphic aureole will be modelled in two cases, (1) with one zone of contact metamorphism with constant properties, and (2) a zone made up of several steps/layers with different elastic properties, which is used in order to simulate a gradual increase followed by a sudden drop in elastic properties, bordering the intrusion.

Table 4.3-1 provides the elastic properties used in the study. Inner layer of contact aureole 1-4 relates to case (2) of contact aureole modelling, and the values are defined by gradually increasing them from the contact aureole to and including inner layer 3, before a sudden drop is modelled by significantly lowering the values in the inner layer 4, according to Smallwood and Maresh (2002), (Figure 3.2.1).

*Table 4.3-1 - Elastic properties used for modelling. Well 7222/1-1 and associated data is from NPD (2019) and the DISKOS database, well 7715/3-1 is provided to UNIS by the NPD.*

<b>Facies</b>	<b><math>V_p</math> (m/s)</b>	<b><math>V_s</math> (m/s)</b>	<b>D (g/cm<sup>3</sup>)</b>	<b><math>V_p/V_s</math> ratio</b>	<b>Source</b>	<b>Depth, m MD</b>
Sand (S)	3092	1819	2.46	1.7	7222/1-1	1020-1025
Fine sand (F.S)	3080	1812	2.47	1.7	-	S>F.S>Sh
Shale (Sh)	3070	1806	2.48	1.7	7222/1-1	1796-1866
Organic rich shale	3277	1928	2.5	1.7	7222/1-1	1034-1049
Intrusion	6096	3277	3.0	1.86	7715/3-1	2485-2547
Contact aureole	4689	2520	2.67	1.86	7715/3-1	2406-2484
Inner layer 1	4996	2686	2.7	1.86	Smallwood and Maresh (2002)	-
Inner layer 2	5100	2742	2.725	1.86	Smallwood and Maresh (2002)	-
Inner layer 3	5200	2796	2.75	1.86	Smallwood and Maresh (2002)	-
Inner layer 4	3809	2047	2.5	1.86	Smallwood and Maresh (2002)	-

## 4.4 Seismic modelling

Seismic modelling can help to identify features that are potentially detectable and resolved in seismic data, and to provide a link between what is observed in the field and the expression in the seismic data, in order to guide interpretation of real seismic data (Magee et al., 2015; Eide et al., 2018; Rabbell et al., 2018). In order to study how igneous intrusions at Botneheia would be expressed in seismic data, synthetic seismic images will be generated first from 2D vertical sections and then from a 3D geological model, all built based on the interpreted virtual outcrop models. A detailed review of seismic modelling methods is outside the scope of this thesis and they will therefore only be briefly presented here, including the applied method.

Seismic modelling provides insights on elastic wave propagation in the subsurface, and is known to be cost-efficient, though dependent on the methods used (Lecomte et al., 2016). High-resolution virtual outcrop models allow for realistic geological models of high detail to be used as input for seismic modelling. This detail level may even be higher than what the typical seismic resolution would be, but it can give insights on what potential effects fine details may have on the seismic response. Seismic modelling can be performed in various ways and there are two approaches for 2(3D) geological structures – full-wavefield and ray-based. These two approaches are both widely used as they have both their pros and cons, meaning full-wavefield may be the best fit for one study, while ray-based will be favourable for another. The full-wavefield approach can be seen as the ideal modelling strategy, as it results in complete synthetic seismograms ready to use for processing and imaging tests (Lecomte et al., 2016). The ray-based method is in comparison much faster and requires less computer-cost, thus generating synthetic seismograms more efficiently. Due to these factors, a ray-based method was used in this study, namely a convolution modelling one, because both time and computer resources are restricted.

There are two main convolution modelling types within the ray-based class, i.e. 1D convolution and 2(3)D convolution. 1D convolution is fast, efficient and widely used in the industry, i.e. for well calibration and seismic inversion, but it is too simplistic and should be disregarded in favour of 2(3)D convolution for modelling of detailed target structures, such as those provided by the digital outcrop models in this study (Lecomte et al., 2015; Lecomte et al., 2016). The 1D convolution approach overestimates horizontal resolution and does not account for lateral velocity- and geometry-variations, which is inaccurate for geologically complex areas

(Lecomte et al., 2016; Eide et al., 2018; Rabbel et al., 2018). On the other hand, the 2(3D) convolution method allows for more realistic imaging effects affecting illumination and resolution, whilst being computationally nearly as efficient as the 1D method (Lecomte et al., 2016). In addition, the 2(3)D modelling approach directly generates 2(3)D seismic Pre-stack Depth Migration (PSDM) images, i.e. images in the depth domain (the optimal output of a seismic imaging) and this allows direct comparisons with the input outcrop models.

The 2(3)D convolution method uses the image response of a point scatter - called Point-Spread Function (PSF) - for the convolution, the PSF, being a function of various parameters including the average velocity at the considered zone, a seismic wavelet and the maximum geological dip imaged by seismic waves and later called maximum illuminated dip (Lecomte et al., 2016). The PSF is then convolved with the reflectivity in order to generate PSDM images. For this study, a maximum illuminated dip of  $45^\circ$  has been selected, and the cases are modelled with a zero incident-angle for simplicity, as earlier discussed (corresponding to a zero-offset seismic acquisition). The average velocity is in the interval of  $\sim 3.0 - 4.0$  km/s in the studied cases. For further review of the methods used, see Lecomte et al. (2015) and (2016), and further use and description of these methods are given in e.g. (Flesland, 2017; Eide et al., 2018; Friestad, 2018; Rabbel et al., 2018).

#### **4.4.1 From outcrop to synthetic seismic - seismic modelling workflow for 2D-models**

The interpretation of intrusion geometries, facies boundaries and formation boundaries were used as input for generating 2D-images of the geological sections for input to the seismic modelling, this by following the steps listed below:

1. Interpretations are projected as 2D-panels parallel to the outcrop by taking a high-resolution screenshot within LIME and it is exported as an image file.
2. This image file is set as a background layer within a photo editing software, in this case, Adobe Illustrator. The interpreted intrusion geometries and stratigraphic units are traced and filled with a specific colour associated with the different lithologies. As there is little lateral stratigraphic variation, the interpretation of stratigraphic units is extrapolated into areas without data in order to make a complete figure.
3. The complete 2D-image showing a model of the outcrop is then converted to 32 bit greyscale (png.) image, so that it can be mathematically identified by a *MATLAB*-script.

Each distinct lithology has now a specific black/white-ratio number associated to it, and these distinct lithologies and associated colours are referred to as a “block”.

4. Elastic properties ( $V_p$ ,  $V_s$  and density) are assigned to each block. These properties are selected as described in section 4.3.
5. The greyscale image is imported to *MATLAB* by using a script in which the elastic properties are connected to their associated block, which is identified by the black/white number. The script writes one *SEG-Y-file* (seismic format used by the modelling software) for each property, meaning block,  $V_p$ ,  $V_s$  and density.
6. These models are imported to the SeisRoX software of the NORSAR Software Suite as properties, which are used to build a target model.
7. A user-defined *Wavelet*-workflow is set up by assigning average velocity, incident angle, max reflector dip and wavelet frequencies, in order to generate a reflectivity model and then the following seismic images. A sampling of (X, Z) 1 m x 0,33 m is used. The workflow is complete after ~ 1 minute.

#### **4.4.2 From outcrop to synthetic seismic – seismic modelling workflow for 3D-model**

This workflow continues where the workflow of the complete building of the 3D geological model in section 4.2 ended. As the model was exported from Petrel, it could be opened as a 3D model within SeisRoX with the elastic properties ( $V_p$ ,  $V_s$  and density) attached as properties. The following steps were used in order to generate a synthetic seismic model:

1. A user-defined *Wavelet*-workflow is set up, as for the 2D modelling, but now with the 3D-model as input and sampling of (X, Y, Z) 5 m x 5 m x 1 m, i.e. less detailed than for the 2D-models. The workflow is complete after 2 hours and 6 minutes.
2. The resulting synthetic seismic can be displayed as a 3D model in the *3D depth viewer* within SeisRoX, and in the *2D viewer* where every slice of the model can be viewed in all directions, i.e. XZ, YZ, and XY.

## 5 Results

The following section will present the results from the seismic modelling of one 3D model and two 2D-models. Firstly, the geological interpretation of the virtual outcrop models is addressed. Secondly, synthetic seismic images from both 2D and 3D- models will be analysed in terms of intrusion architecture, structures and seismic expression. By using different dominant frequencies and input structures, the seismic expression of intrusions is studied. The changes in input structure correspond to cases with or without a contact aureole surrounding the intrusion, and a contact aureole with several inner layers versus “one-zone”-aureole.

### 5.1 Virtual outcrop models

The virtual outcrop models were interpreted with the aim to (1) identify the main intrusion geometries, (2) identify the main formation boundaries and (3) identify facies boundaries - whenever possible. Two models were used in order to do this, namely one overview model and one detailed model of a well-exposed outcrop section, i.e. the lidar-model and the photogrammetry-model of the northern side of Botneheia, respectively.

#### 5.1.1 Interpretation of lidar-model

The lidar-model was interpreted following the aim as stated above. The northern side of Botneheia is particularly well exposed and it allows for a detailed interpretation (Figure 5.1.1, A<sup>1</sup>). In addition, Knarud (1980) logged this outcrop-section at one location (Figure 5.1.1, A<sup>1</sup>), from Top Botneheia Fm. to the top of the cliff, this log was thus used to aid the interpretation of the northern side (Figure 5.1.2).

Starting at the bottom of the model at the northern side and going up, one unit stands out from the outcrop as a cliff-forming black shale, which is characteristic for the Botneheia Fm. There is a package of shale overlying the Top Botneheia Fm, which is interpreted to correspond to the Tschermakfjellet Fm, supported by the log from Knarud (1980) in Figure 5.1.2. This unit gradually coarsen upwards into a sandstone package, which marks the transition to the De Geerdalen Fm (Knarud, 1980) (Figure 5.1.2). There are several stacked coarsening upwards units of shale grading into sandstone all the way to the top of the outcrop section. The facies boundaries within the De Geerdalen Fm. is thus interpreted by identifying the main sand packages. The sand packages vary in thickness, but have little lateral variation and they are

mainly layer parallel. They can therefore be traced to the eastern side of Botneheia, and partly to the western side. The interpretation of formation- and facies-boundaries have been extrapolated into areas where these boundaries are not visible, e.g. due to scree, due to the horizontal nature and little/no lateral variation of the stratigraphic units at Botneheia. This is done in order to use this interpretation as input to build a geological model covering all of Botneheia.

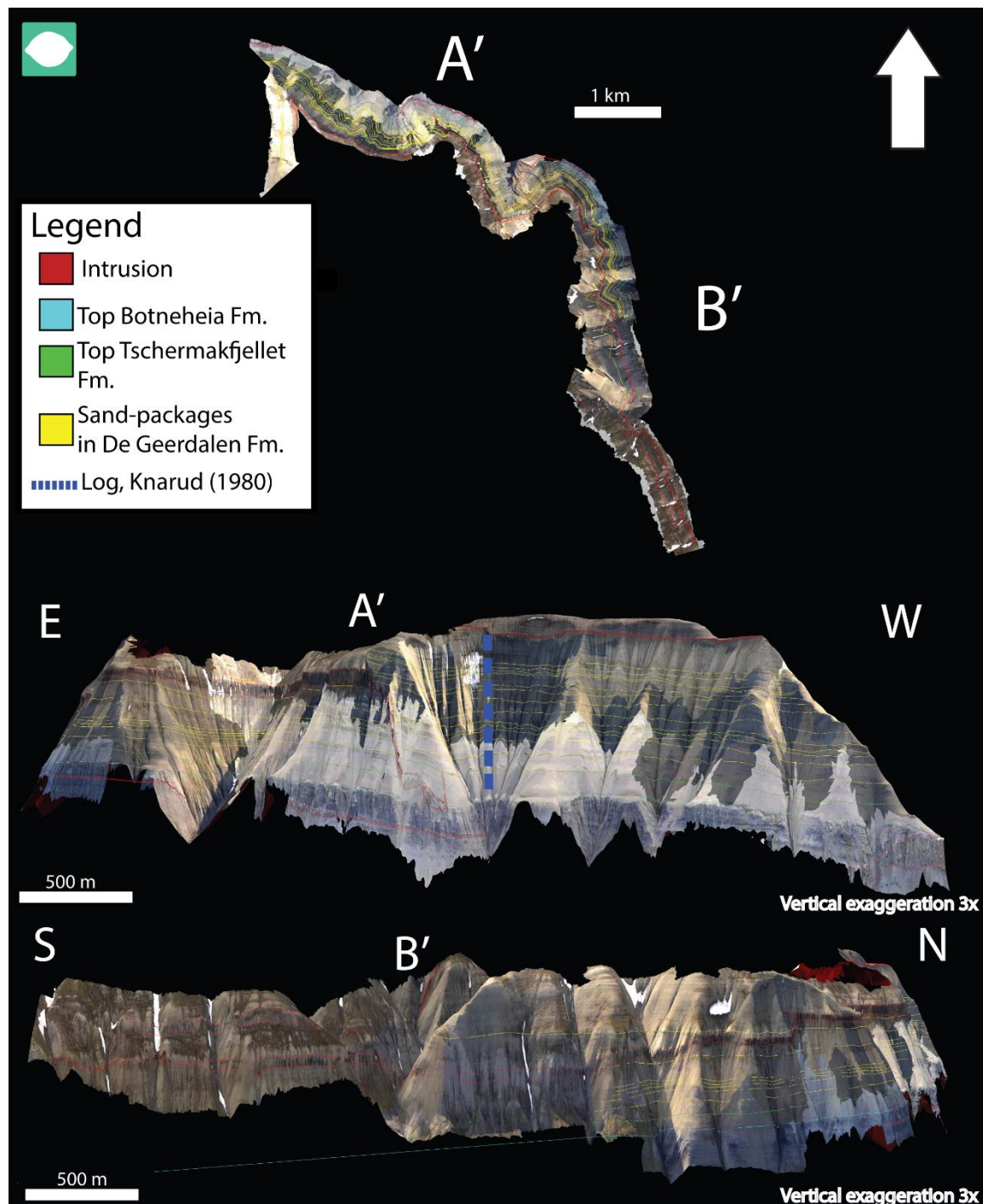


Figure 5.1.1 - Interpreted virtual outcrop model from lidar-data, showing Botneheia viewed from above and well-exposed outcrop sections, A' and B', northern and eastern-side, are viewed in detail, looking directly at the outcrop. The section logged by Knarud (1980) is indicated, and log is presented in Figure 5.1.2.

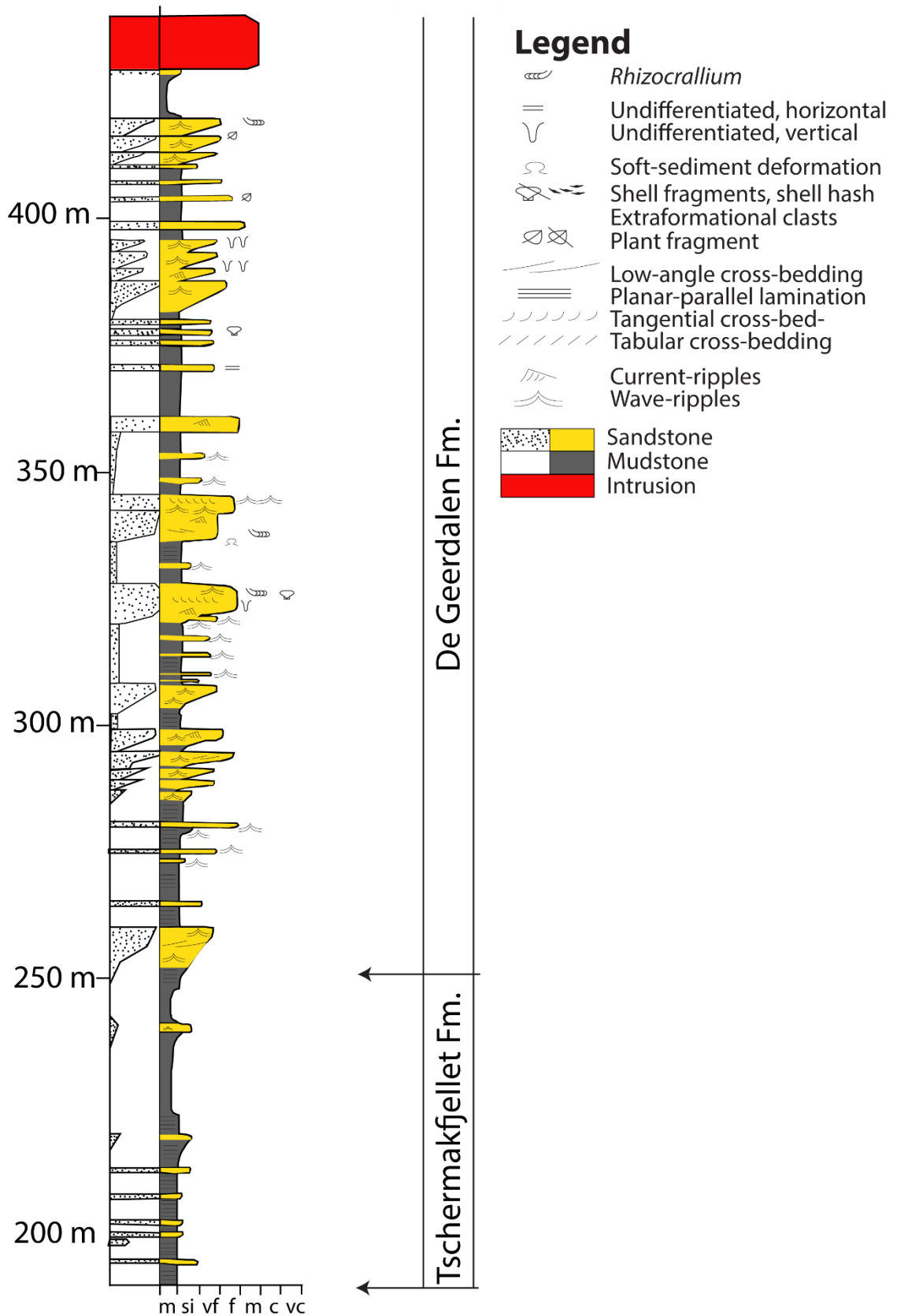


Figure 5.1.2 - Sedimentary log of the northern side of Botneheia, showing the exposed lithology. Logged from top Botneheia Fm and towards the top of the northern outcrop section, ending in an intrusion. Modified from Knarud (1980).

The igneous intrusions stand out from the surrounding host-rocks, both by colour and by forming small cliffs, which allows for confident interpretation. Their geometry has a high degree of lateral and vertical variation compared to the sedimentary host-rocks. Starting from the bottom on the northern side of Botneheia (Figure 5.1.1, A'), there is one large intrusion, ~ 30 m thick in the most western part. There is a lack of data in the lidar-model to the east of this intrusion, but it continues eastward, as seen in Figure 5.1.3. This intrusion is relatively layer-parallel and thick (~ 30 m) in the west, before it thins (~ 2 m) eastward and have splays. There are several disconnected, slightly offset parts of this thin intrusion towards the east, before it dips gently towards the top of the Botneheia Fm., before the valley in the left in Figure 5.1.1, A'. The slightly offset parts may have similarities to step- and bridge-structures, as described in the theoretical background (3.1). The bridges would be the host-rock in between the offset parts of the intrusion, while a step has not been able to form, maybe due to a lack of magma infill. The intrusion is difficult to trace within the valley to the east in Figure 5.1.1, A', due to the erosion that probably has undergone there, but it appears again on the left side of the valley, with approximately the same thickness, splays, and disconnected parts. This thin sill continues for some distance further into Flowerdalen, the eastern side of Botneheia, before it becomes untraceable (Figure 5.1.1, B').

Going back to the northern side of Botneheia again, a sub-vertical transgressive intrusion, a dyke, shoots up from the Botneheia Fm. and towards the top of Botneheia (Figure 5.1.1, A'). This dyke is probably connected to the same magma-network as the sill(s) in the Botneheia Fm., but there is no clear link between them in the outcrop section. The sedimentary units are offset from one another on each side of the dyke, i.e. one unit on the western side is located a bit higher than the same unit on the eastern side of the dyke (Figure 5.1.3). This can be a result of uplift mechanisms acting at the time of intrusions, or it may be due to a fracture/fault already existing in the area, in which the magma has intruded and formed the dyke. This transgressive intrusion goes into a thick sill at the top, which continues into Flowerdalen. By following the intrusion into Flowerdalen and southwards (Figure 5.1.1, B'), one can see that the intrusion moves down at several locations. This structure has similarities to step- and bridge-structures as previously described. While the thin sill in the Botneheia Fm., mainly had bridge-like structures, this thick top sill has more prominent step-structures, i.e. the sill does not have offset parts, but rather consists of one connected sheet with steps, which can be indicative of continued magma infill at the time of intrusion (Schofield et al., 2012). This sill continues all the way into the southernmost part of Flowerdalen, until it cannot be traced any longer. At this location,

there is also one additional sill present. This sill is overlying the first mentioned and it can be traced at half of the eastern side of Botneheia, facing Flowerdalen. This intrusion seems to dip upwards towards the dyke, which shoots up and goes over all of Botneheia and into the DeGeerdalen on the other side of Botneheia. It is difficult to constrain in the outcrop section if this dyke and the sill is connected, as this outcrop is prone to scree, valleys and gullies. Nevertheless, it is likely that the dyke and this sill dipping towards it are related because of their close spatial relationship, indicating that they both belong to the same network of intrusions.

### **5.1.2 Interpretation of virtual outcrop models from photogrammetry**

The northern model from photogrammetry was also interpreted (Figure 5.1.3), in order to assist the lidar-dataset. The main focus was to constrain the interpretation in areas with missing data in the lidar-model. The interpretation was performed in the same way as for the lidar-model, i.e. by focusing on intrusion geometry, formation- and facies boundaries. The model representing the northern side of Botneheia displays parts that were missing in the lidar-model, thus allowing for interpretation of the bottom part of the northern side of Botneheia. There is a massive package of grey shale, underlying the cliff-forming black shales of the Botneheia Fm. This package is interpreted to also be a part of the Botneheia Fm, as this corresponds to a common characteristic of that formation in Central Spitsbergen (Dallmann, 1999). There is one other unit present in the area, Vikinghøgda Fm., according to maps by the Norwegian Polar Insitute, but it is difficult to interpret this exact formation boundary because the bottom part of the outcrop is covered by scree.

The large, ~ 30 m thick, sill is completely visible in this model, as commented in section 5.1.1. This allows for interpretation of the sill geometry (as presented in the section above), which is important to constrain for further geological modelling.

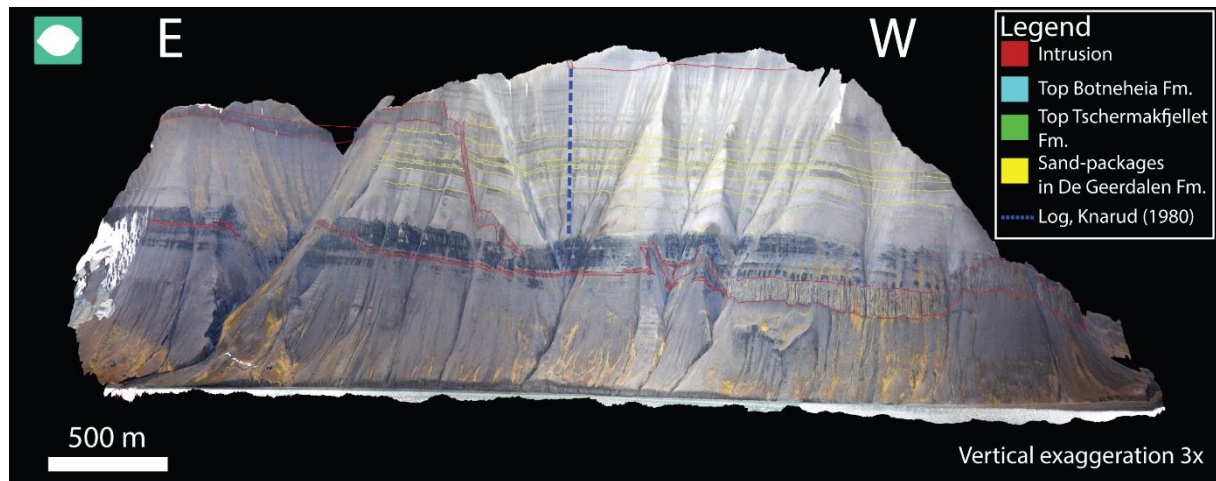


Figure 5.1.3 – Interpreted virtual outcrop model of northern side of Botneheia.

## 5.2 2D geological models – input for 2D modelling

Simplified 2D models were created based on the interpretation presented above, in order to use them as input models for 2D seismic modelling. Three models were created for the northern side of Botneheia (Figure 5.2.1), and two models for the eastern side facing Flowerdalen (Figure 5.2.3). These five models are the fundament for five 2D seismic modelling cases.

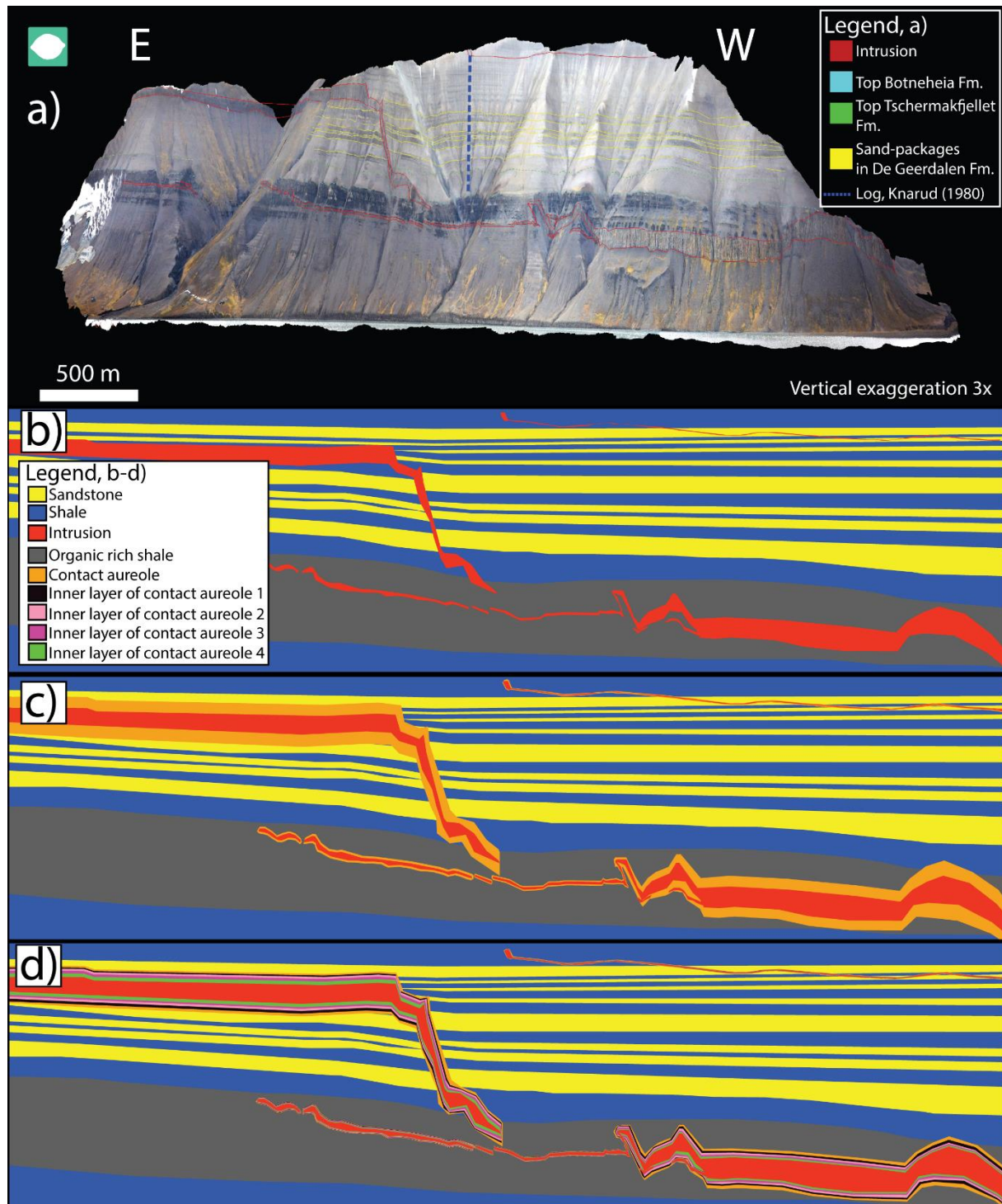


Figure 5.2.1 – 2D geological models from interpretation of northern side of Botneheia. a) Interpreted virtual outcrop model, b-d) 2D geological models with same scale, orientation and exaggeration as given in a). b) Model without contact aureole. c) Model with contact aureole. d) Model with several inner layers of contact aureole.

The 2D models (Figure 5.2.1, b-d and Figure 5.2.3, b-c) give a simplified representation of the sedimentary strata present in the outcrops, i.e. there is no lithological variation within the sedimentary facies in the model and the units are extrapolated into areas without data. However, the intrusion architecture is modelled with a higher degree of detail, since they are the main focus in this study. The intrusions are modelled with a surrounding contact aureole in Figure

5.2.1, c-d), with one zone in c) and four inner layers in d). The total thickness of the contact aureole varies between 100-150% of the intrusion thickness in the input models, because this is within the expected thickness interval for a contact aureole (e.g. Aarnes et al., 2010; Senger et al., 2014a). This is supported by observations from the field, where a thin sill with a visible contact aureole, i.e. sediments showing indications of contact metamorphism and metasomatism by colour change and/or reaction zones (Senger et al., 2014a), of ~100% of sill thickness was observed (Figure 5.2.2). However, the extent of the contact aureole may exceed the visible part, as the geochemistry of the host rock may be affected, thus the zone can therefore be even thicker (e.g. Hubred, 2006; Aarnes et al., 2010; Senger et al., 2014a).

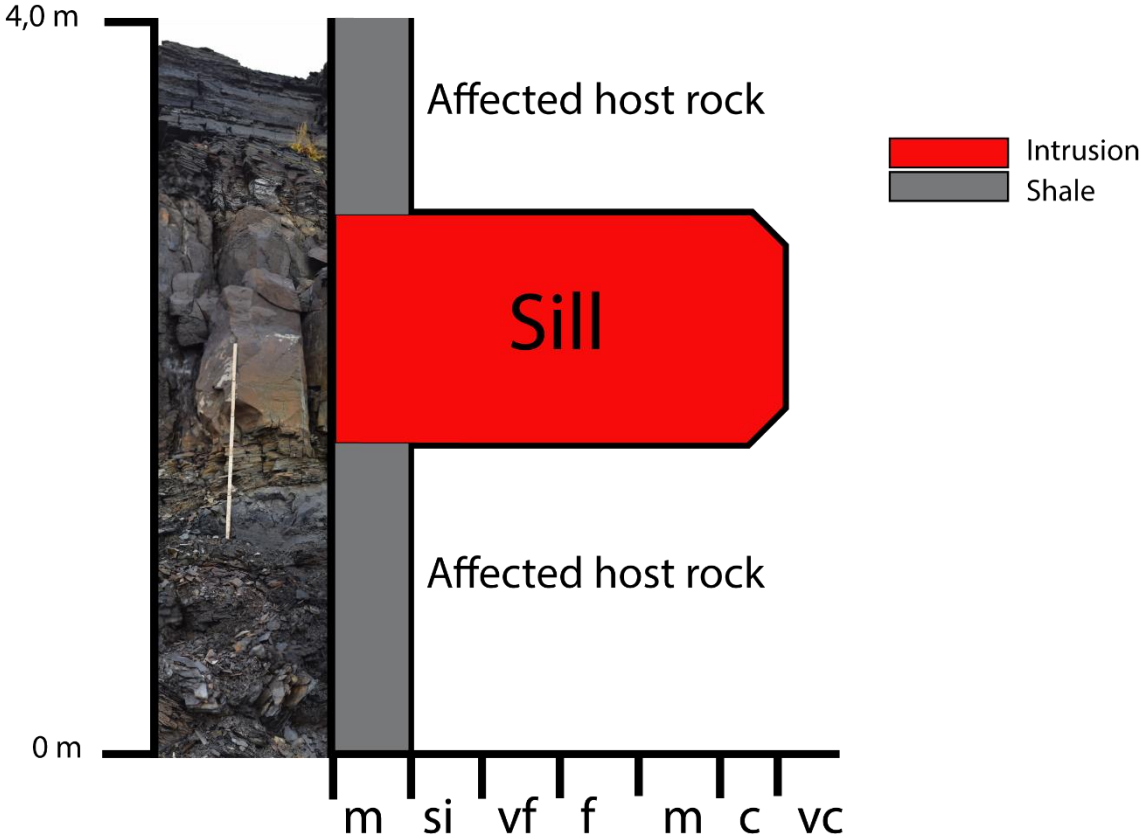


Figure 5.2.2 – Simplified log including photo of sill, ~2 m thick, within Botneheia Fm exposed on the northern side of Botneheia. Photo shows that the colour of the host rock changes towards the sill.

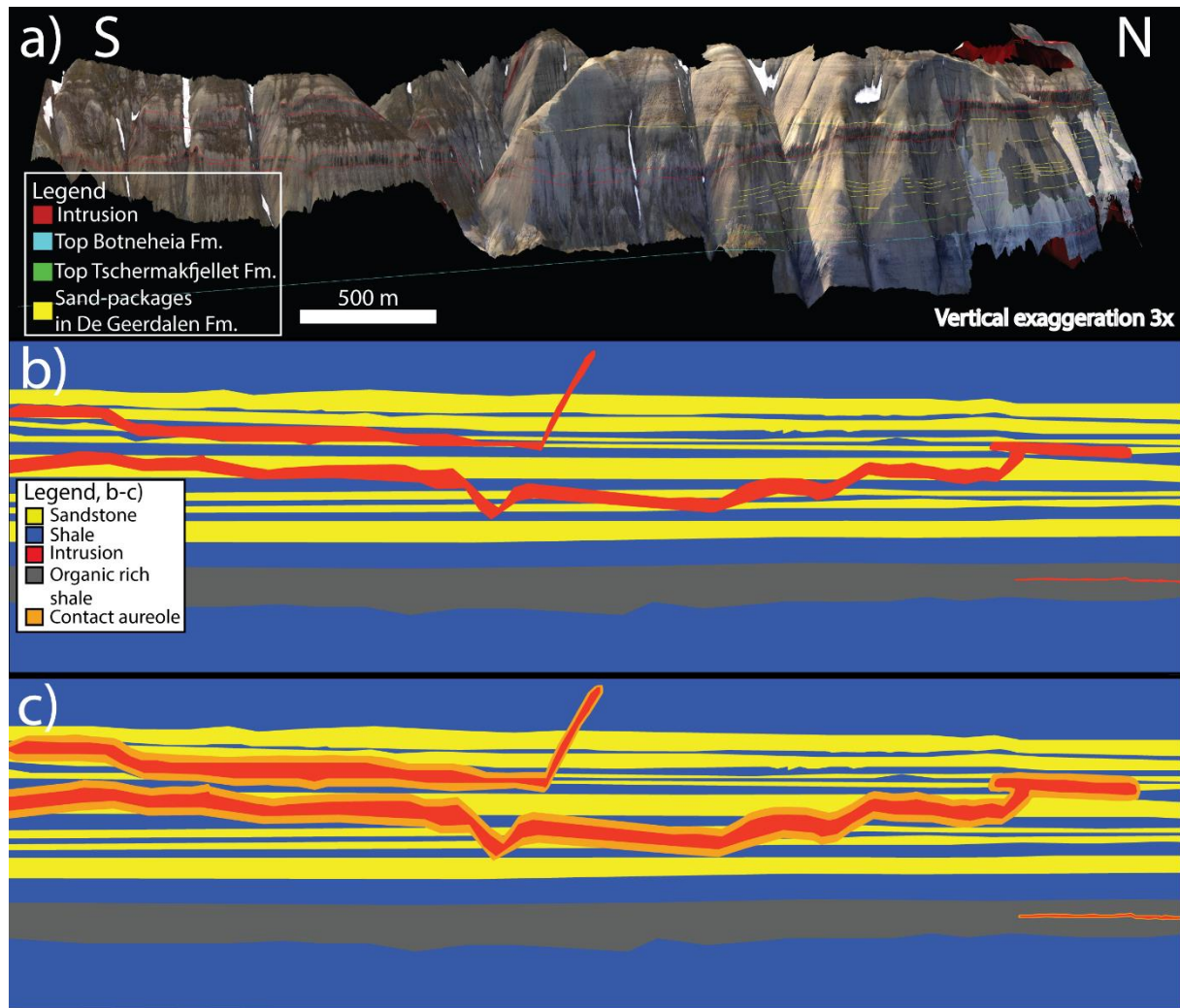


Figure 5.2.3 – 2D geological models from interpretation of eastern side of Botneheia. a) Interpreted virtual outcrop model. b-c) 2D geological models with same scale, orientation and exaggeration as given in a). b) Model without a contact aureole. c) Model with a contact aureole.

The 2D geological models for the eastern side of Botneheia are not modelled with a contact aureole including inner layers, because it is expected that the seismic images of the northern side will cover this aspect, either by showing an effect or no effect at all. Otherwise, the eastern models are created in the exact same way as the northern models, and give a simplified representation of the outcrop section and its geological features.

### 5.3 3D geological model – input for 3D modelling

This section will present the 3D gridded geological model built to represent Botneheia and its geological features, based on the interpretation of the virtual outcrop models. The gridded model was created following the steps described in detail in section 4.2.

The 3D model gives a large-scale, simplified representation of the stratigraphic units at Botneheia, which have been divided into the facies types: sand, fine sand, shale, organic rich shale and intrusion. These facies types are chosen, because they are dominant in the outcrop section of the formations that are modelled, i.e. Botneheia Fm., Tschermakfjellet Fm., De Geerdalen Fm (e.g Knarud, 1980; Dallmann, 1999; Dallmann, 2015) (Figure 5.1.1 and Figure 5.1.2). The intrusion geometry is modelled based on the interpreted lines from the lidar-model in Figure 5.1.1 combined with the bottom part of the northern side in Figure 5.1.3. Figure 5.3.1 displays the resulting 3D-gridded model, with an overview of the modelled area in a), while b) and c) each represent the slice of the model in which the intrusion geometry was defined from the visible outcrop sections, and later extrapolated in the rest of the model.

The dyke cutting through large parts of Botneheia is visible on the top of the model in Figure 5.3.1 a) and on the slice in b). It is close to vertical, and it is modelled so that it is connected to the other intrusions in the mountain at several locations within the model.

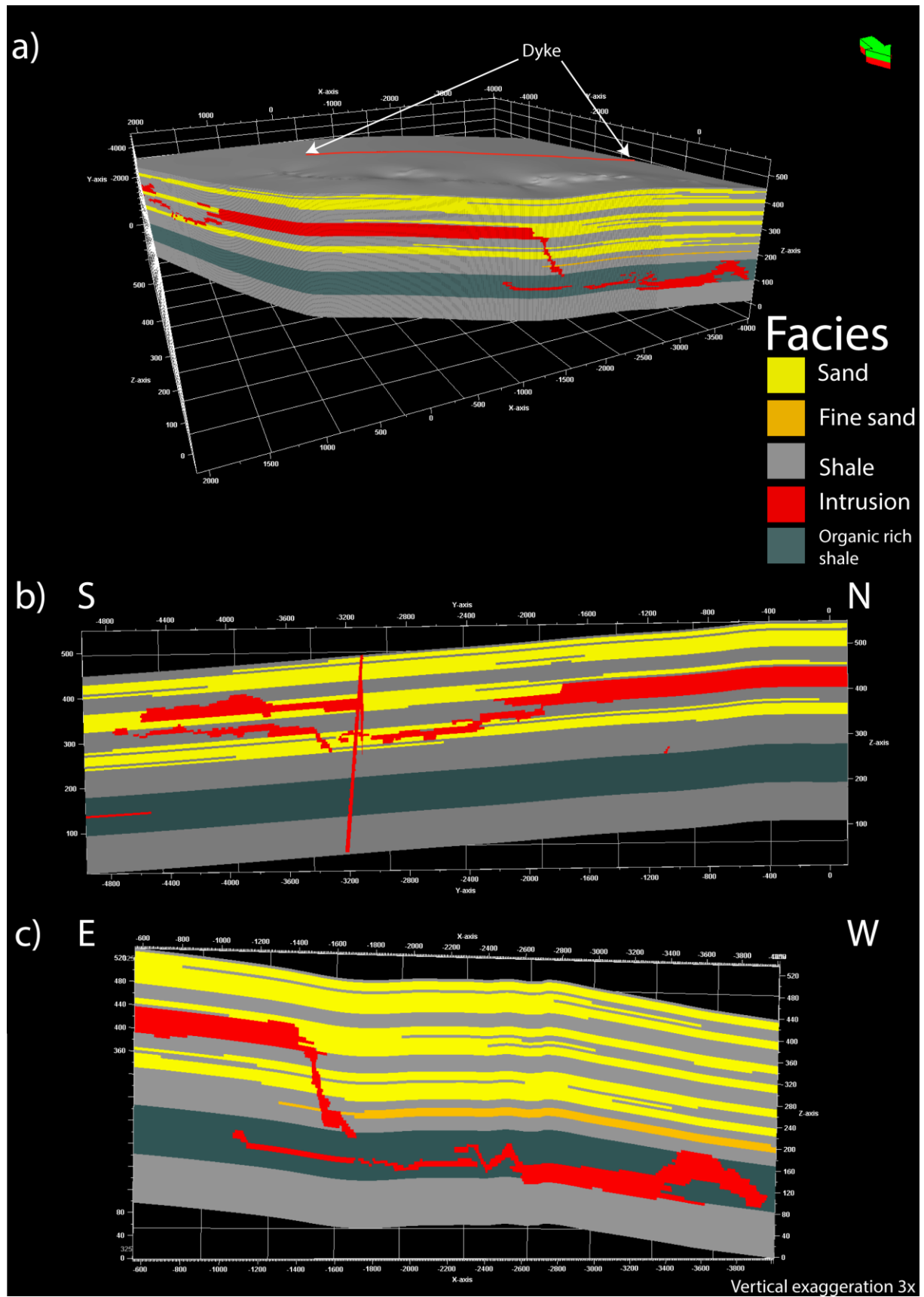


Figure 5.3.1 – 3D geological model representing Botneheia. a) Overview of the area. b) Slice cutting through the model, oriented S-N, corresponds to A' in Figure 5.1.1. c) Slice of the model representing the northern outcropping side of Botneheia, as seen in B' in Figure 5.1.1, and in Figure 5.1.3.

## 5.4 Seismic modelling of 2D-models

The results from the seismic modelling of the 2D-models will be presented in this section. Synthetic seismic images are generated from the 2D input models presented in the previous section by following the steps described in detail in section 4.4.1. The modelling setup defines which max illuminated reflector dip, average velocity, incident angle and dominant frequency that shall be used. The dominant frequency is the main factor that will be changed in this study, in order to investigate which geological features that are resolved in the seismic. For this study, the chosen frequencies are Ricker-wavelets of 20 Hz and 40 Hz because these frequencies correspond to dominant ones at depths of 3 km and 1 km, respectively, this derived from 3D seismic dataset by Eide et al. (2018).

There are five 2D modelling cases, as previously presented: three from the northern side of Botneheia - one without contact aureole, one with contact aureole and one with inner layers of contact aureole, and two models from the eastern side of Botneheia – one without and one with contact aureole.

### 5.4.1 Changing the dominant frequency

This section will present the result of changing the dominant frequency, i.e. 20 Hz vs. 40 Hz, represented by two of the five modelling cases, i.e. (1) Botneheia north and (2) Botneheia east, both without a contact aureole, as the potential effect of a contact aureole will be presented in the next section.

All of the models have high amplitude reflections at the igneous intrusions (Figure 5.4.1 - Figure 5.4.2), because they have high contrast in AI compared to the surrounding host-rock (Figure 5.4.1, b). The geometry of the intrusions are therefore well imaged, and the similarity to the input model is high. Steeply dipping geometries are not imaged as well as horizontal features, due to the limitation in illumination, but rather steeply dipping features are still present in the seismic images.

The main intrusions correspond to thick, strong reflections, both at top and base in the 20 Hz seismic image of Botneheia north (1) (Figure 5.4.1). The very thin intrusion (i) at (1) Botneheia north (Figure 5.4.1, c,) is also visible, but the amplitude is low relative to the other intrusions in the modelled area (ii, iii and iiiii) (Figure 5.4.1, c). The (i) reflection has a high degree of

lateral variation with several gaps where the amplitude drops down to near zero. Some of these gaps seem to correlate to steep reflections located between intrusion (i) and (iii) in the “host rock area”. These steep reflections are most likely seismic image artefacts, i.e. a cross-pattern resulting from the PSF (Lecomte et al., 2015), due to the limited illumination pattern used, i.e. 45 - degree maximum illuminated dip. Intrusion (ii) is well imaged, and its structure has a high resemblance to the input model. However, small details are not distinguished at 20 Hz, due to lack of vertical resolution at this frequency, forming a thick reflection, e.g. at the top where the dyke goes into the top sill (ii), there is a step in the input model, which is not imaged at 20 Hz. The same applies for intrusion (iii) and (iiii); the overall geometry has high resemblance to the input model, while splays and offset parts are not well imaged, but rather a part of the larger reflections. The amplitude of intrusion (iiii) has lateral variation and gaps within the reflection. These observations most likely relate to the bridges, i.e. offset intrusions with host rock in between that exist as a part of this intrusion in the outcrop model. A lowered amplitude may indicate a small offset between the intrusion-parts, while a gap in the reflection amplitude may be indicative of a larger offset, and more host rock present, resulting in a lower-amplitude. However, these amplitude effects may also be the result of interference between reflections, because constructive and destructive interferences may happen (Lecomte et al., 2015). This is because of both a reflectivity that may change signs, e.g. negative to positive, and due to the wavelet shape, which has both positive and negative parts. The splays of intrusion (iii) are not well imaged, especially a small near-vertical splay in the input model, which is not visible at all in the seismic image.

Looking at the eastern side of Botneheia (2) at 20 Hz (Figure 5.4.2, b), the seismic reflections are thick and the geometry of the modelled intrusions are quite well resolved, as for the northern side (1). The reflections are thicker than the intrusions in the input model itself (Figure 5.4.2 b), most likely due to seismic tuning, this is also the case for (1) Botneheia north. The thick intrusion (i) has a large degree of lateral variation in geometry. As interpreted from the virtual outcrop section, this intrusion has a step-structure and this structure is well resolved in the seismic image. The amplitude of the intrusion (i) has a sudden drop and a gap within the reflection in the northern corner, most likely due to the splay that is present in the input model (Figure 5.4.2, a). Going from north and towards south, there are several steps, first downwards, and then some upward, for intrusion (i). There is a thick sill (ii) overlying sill (i) which eventually goes into an intrusion transgressing towards the top of Botneheia (looking at it from S towards N). It is known from field observations and virtual outcrop models that this

transgressive intrusion is a dyke that goes over all of Botneheia. The visible part of this dyke from the eastern side of Botneheia is well-imaged in the seismic image. There is a high degree of lateral amplitude variation in sill (i) and sill (ii) in the southern part where they are located close together. Sill (iii) is clearly visible, but its thickness is over-estimated.

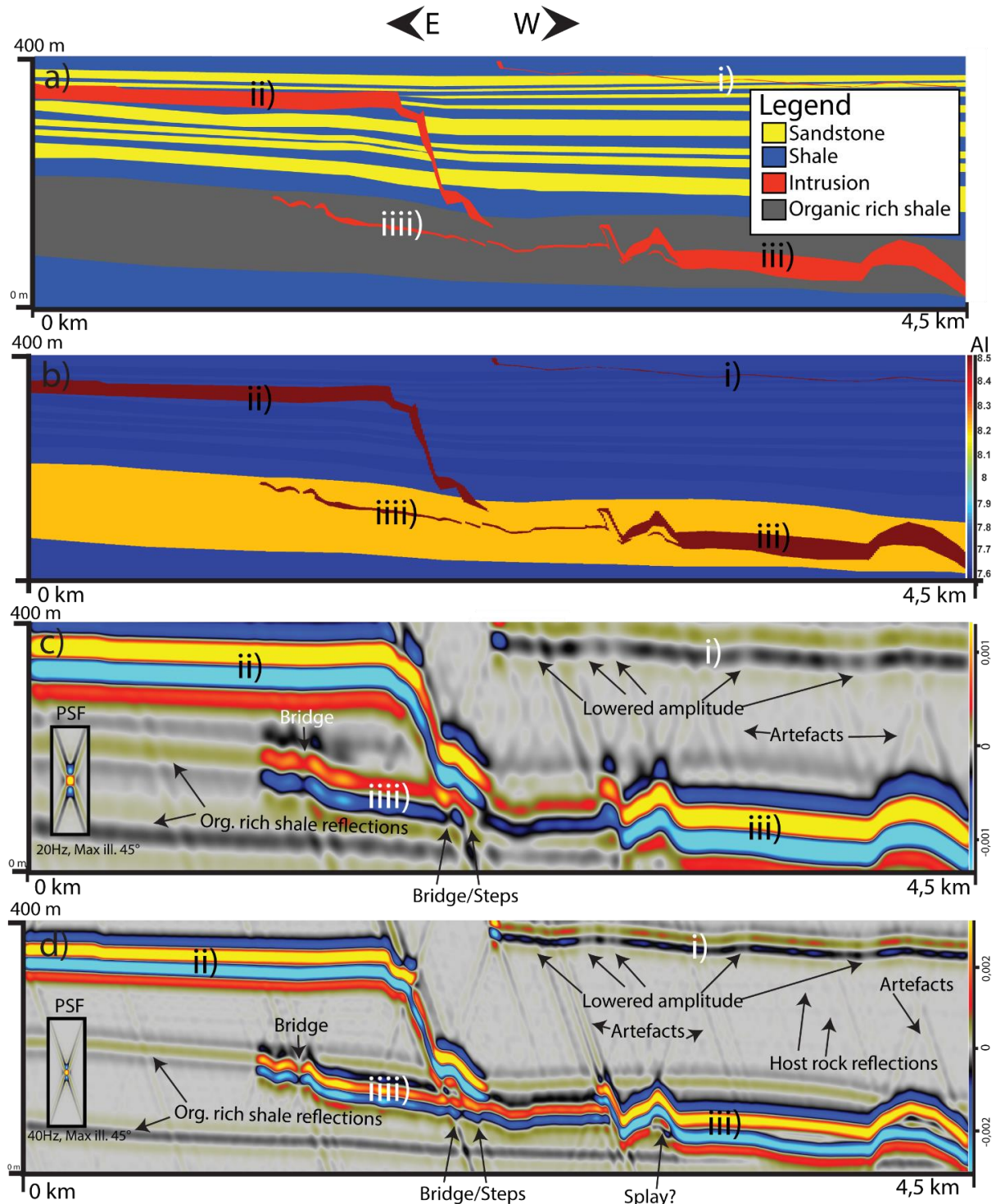


Figure 5.4.1 - a) Input model of Botneheia northern side, without contact aureole. b) Acoustic impedance, note the large difference in values for the intrusions contra the host rocks. c - d) Seismic images showing the effect of varying dominant frequencies, 20 Hz – 40 Hz. The point spread function (PSF) for each seismic image is illustrated, and the maximum dips is set to 45°. Vertical exaggeration 3x.

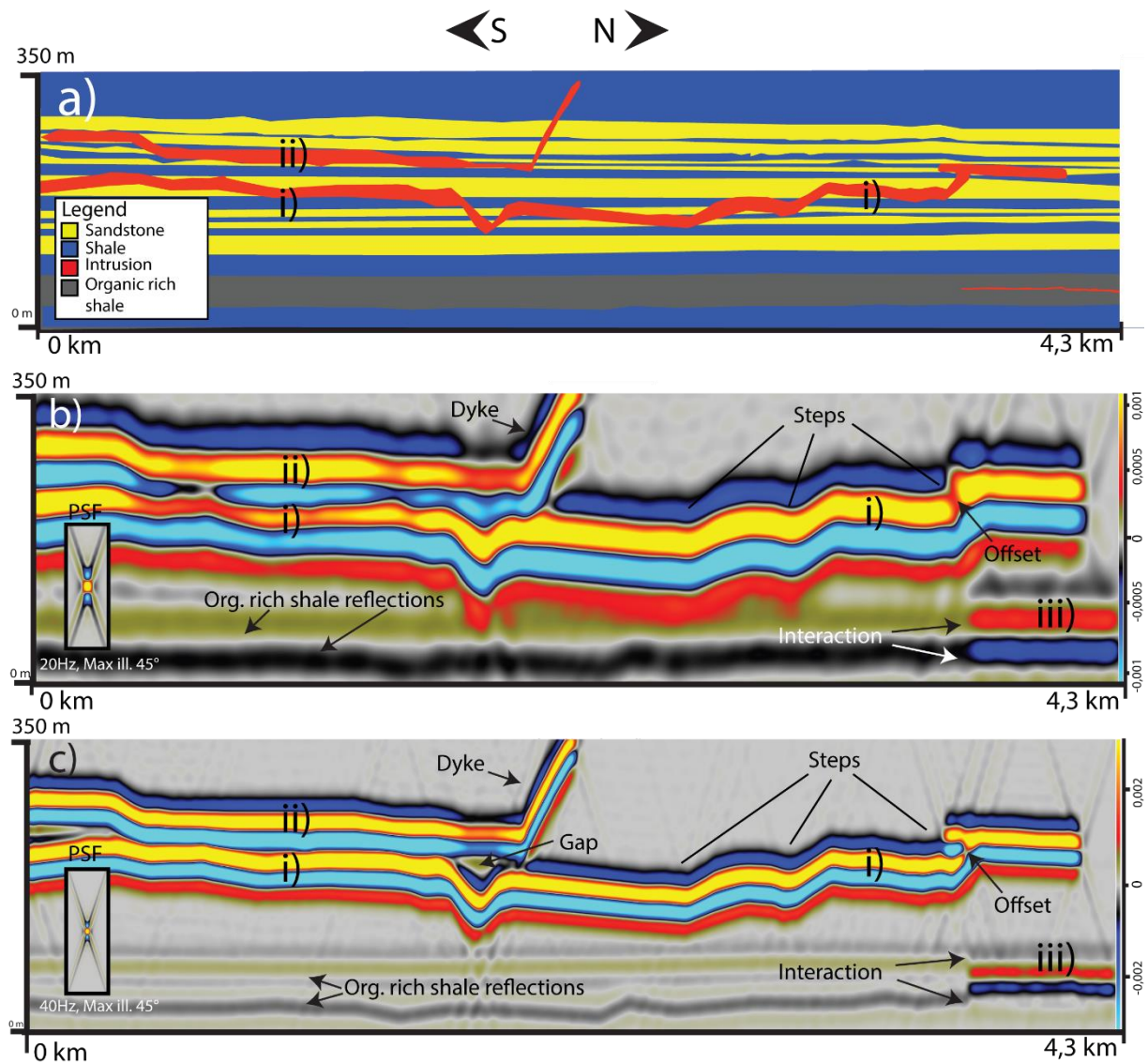


Figure 5.4.2 - a) Input model of Botneheia eastern side, without contact aureole (Figure 5.2.3). b) and c) Seismic images showing the effect of varying dominant frequencies, 20 Hz – 40 Hz. The point spread function (PSF) for each seismic image is illustrated, and the maximum dips is set to 45°. Vertical exaggeration 3x.

The surrounding host rocks are barely visible in the seismic images at 20 Hz, because they have a very low amplitude in comparison to the intrusions. The majority of the facies boundaries can be resolved as horizontal, weak reflections, but there are two stronger near horizontal host-rock reflections near the bottom of Figure 5.4.1, c) and Figure 5.4.2, b). This corresponds to the top and base reflectors of the organic rich shale, as this unit has a higher AI than the sandstone and shale (Figure 5.4.1, b). These two reflections interact with the reflection of intrusion (iii), as the intrusion reflections are embedded into the organic rich shale reflections (Figure 5.4.2, b).

The seismic images modelled at 40 Hz differ from the 20 Hz images, as there is an overall higher degree of detail displayed (Figure 5.4.1, d) and (Figure 5.4.2, c). The reflections are generally thinner than what they are in the 20-Hz images, and thus closer to the actual thickness of the features. The intrusion geometries are overall the same as described for the 20-Hz images, but they are better resolved – as expected due to a higher frequency content - and thus higher resolution.

The seismic image of the northern side (1) at 40 Hz, (Figure 5.4.1, d), shows better resolved intrusion geometries than what were imaged at 20 Hz. Intrusion (i) is still recognised with a high degree of lateral variations in amplitude and gaps. These gaps show less apparent correlation/relationship to the near-vertical features of the in the host rock below, probably because the seismic imaging artefacts, i.e. the cross-pattern from the PSF, is thinner. The top sill (ii) is well imaged, and the connecting part that go into the transgressive intrusion is well resolved, in contrast to the 20-Hz image. Sill (iii) is also well imaged and considerably thinner compared to the 20-Hz image and the near vertical thin part in the left is well resolved too. Two splays are still not imaged in the 40-Hz image. Sill (iiii) have a less degree of lateral amplitude variation than in the 20-Hz image, but it still fluctuates. There are several offset parts of this intrusion. In the seismic, these structures have a resemblance to step-structures, while it is known from the outcrop interpretation that it is closer to a bridge-structure.

The overall imaging features are much the same for the eastern side (2) at 40 Hz. Sill (i) is completely disconnected in the northern part of the outcrop (Figure 5.4.2, c) while there is no disconnection at this location in the 20-Hz images. There is also no interference between sill (i) and (ii) on the 40-Hz image in the south, as both sill (i) and (ii) are well resolved. Sill (iii) is also well resolved and the observed thickness on seismic is close to the actual thickness of the sill in the input model.

The host-rock reflectors are better resolved in the 40-Hz images, but the reflection from the contrasting sand-shale boundary is still weak. As for the 20-Hz image, top and base of the organic rich unit is well resolved. However, the interaction with intrusion (iii) differs, as the intrusion reflections now create a step for both the top and base reflections of the organic rich shale (Figure 5.4.2, c).

### 5.4.2 Including a contact aureole

This section will present reflectivity- and wiggle-plots (Figure 5.4.3), and the seismic images at 40 Hz (Figure 5.4.4) resulting from input models including a contact aureole, which surrounds the intrusions. The contact aureole is modelled in two cases for the northern side of Botneheia, i.e. (1) with one zone of contact metamorphism with constant properties (Figure 5.4.4, b), and (2) a zone made up of several inner layers with different elastic properties (Figure 5.4.4, c), as previously described. The eastern side of Botneheia is only modelled with case (1).

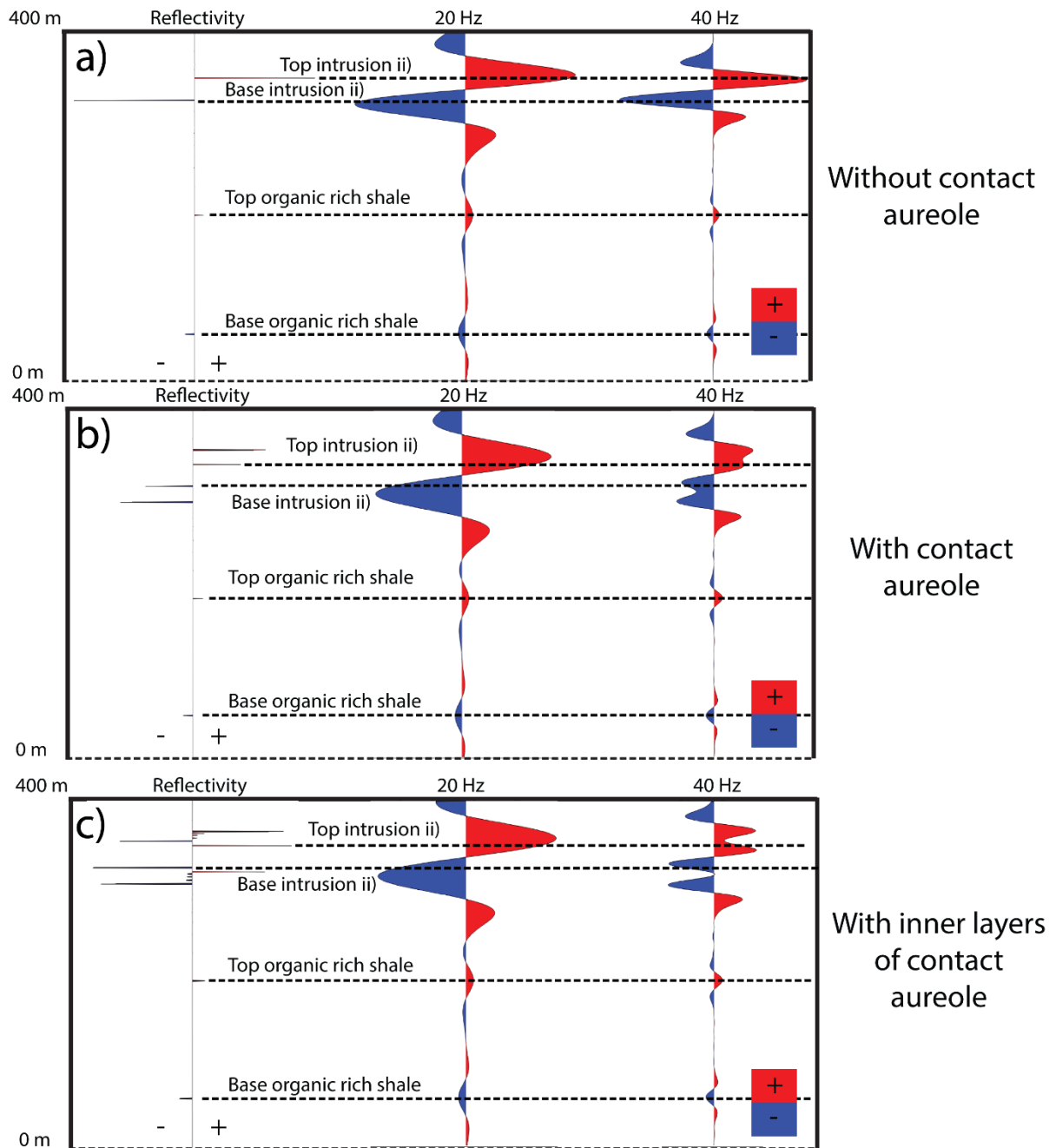


Figure 5.4.3 – Reflectivity- and wiggle-plots of Botneheia north, all at location 0,8 km, i.e. dashed line in Figure 5.4.4. a) Without contact aureole. b) Including one zone of contact aureole. c) Including several inner layers of contact aureole. Dashed line is correlation from reflectivity plot to the response in the wiggle-traces.

The reflectivity- and wiggle-plots show the amplitude of the reflected wave and the resulting waveform versus depth, respectively. This is included as it illustrates the seismic response of the reflectors in detail, and can thus help to better analyse the following seismic images. The wiggle-plots, show that the two peaks and troughs both are resolved individually at the top in Figure 5.4.3 b and c) at 40 Hz, while these peaks are resolved as one reflection in the 20-Hz wiggle-plot. The high-amplitudes in the plots respond to the intrusions, while the peak and trough with low amplitude in the lower part of the plot correspond to the top and base of the organic rich shale, supported by the seismic images in Figure 5.4.4.

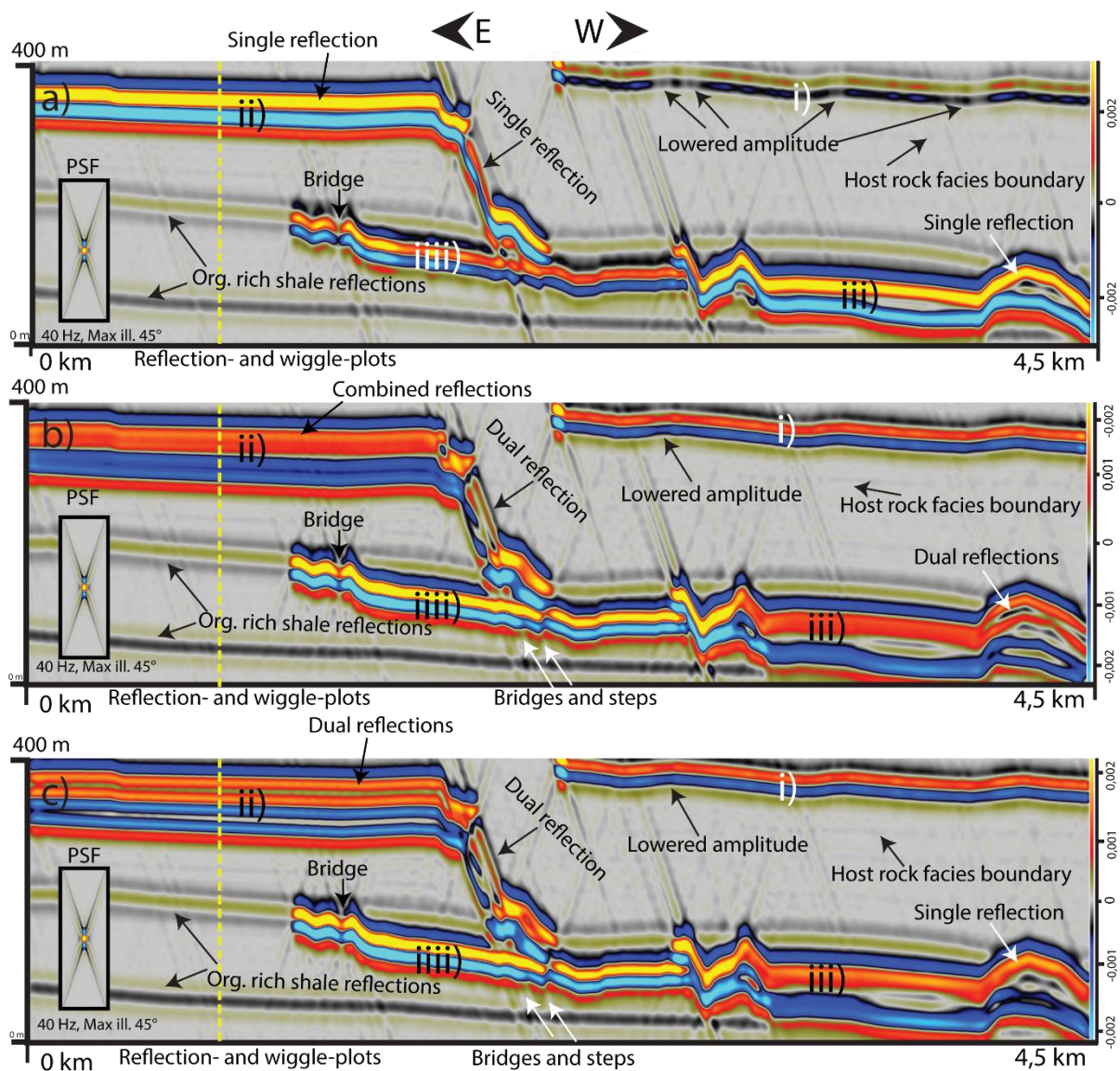


Figure 5.4.4 – 40-Hz seismic images of Botneheia north, dashed line indicating position of plots in Figure 5.4.3. a) Without contact aureole. b) Including one zone of contact aureole. c) Including several inner layers of contact aureole.

The modelled case including one zone of contact metamorphism leads to thicker reflections in Figure 5.4.4, b). By zooming in on intrusion (ii) and (iii) one can see that two reflections are

combined into one thicker reflection, also supported by the wiggle-plot (Figure 5.4.3 b), while two reflections are resolved in the arc-shape in intrusion (iii). This means that the contact aureole reflection in some cases is smeared together with the reflection from the intrusion itself, leading to a thicker reflection, while it can also be resolved in addition to the intrusion reflection, so that two reflections appear. The dyke is imaged with dual reflections in both cases including a contact aureole (Figure 5.4.4, b and c). The uppermost western thin sill (i) is imaged with a stronger reflection for the two cases involving a contact aureole (Figure 5.4.4, b and c). In the case without a contact aureole, the highest amplitude reflections correspond to the upper eastern intrusion (ii) and the bottom western (iii) (Figure 5.4.4, b and c), while this changes when a contact aureole is included. For these two cases, the strongest reflection originates from intrusion (iii). Case (2) with inner layers of contact aureole has similarities to the case with one zone of contact metamorphism, but it has resolved a higher number of single-reflections for intrusion (ii), as seen in the wiggle-plot (Figure 5.4.3 c), while the lowermost western sill (iii) is more smeared (Figure 5.4.4, c). As mentioned, two reflections are resolved in the bottom western corner in Figure 5.4.4, b) while in Figure 5.4.4, c) there is mainly one resolvable reflection, with one semi-attached to the low amplitude reflection within the arc-shape. The parts of intrusion (iii) that were offset in Figure 5.4.4, a), indicating bridges, are more connected in Figure 5.4.4, b and c), probably due to limited lateral resolution, and can thus be interpreted to represent broken-bridges and/or steps, while actually being bridges. There is no visible changes in the host-rock reflections for the images involving a contact aureole, and the seismic expression of the host rocks is thus the same as described in the previous section.

The eastern side of Botneheia is modelled with one zone of contact aureole, and the overall geometry of the intrusions is well imaged. The seismic image including a contact aureole differs slightly (Figure 5.4.5, b) from the one without an aureole (Figure 5.4.5, a) as the reflection from the thin sill (iii) becomes stronger, and the gap between sill (i) and (ii) in the middle of the outcrop is filled with a reflection with a higher amplitude (Figure 5.4.5, b). The part of sill (ii) overlying this gap has a higher amplitude in the model including a contact aureole. There is a larger gap in the most southern part of the model between sill (i) and (ii) in the model without an aureole. The steps are well imaged, but there is still an offset, as for Figure 5.4.2, due to a disconnected part in the seismic images in the north. The host rocks are not well imaged above the main sills (i) and (ii), but one can still see weak reflections. The organic rich shale reflectors are also well expressed in these seismic images, as previously presented for the northern side.

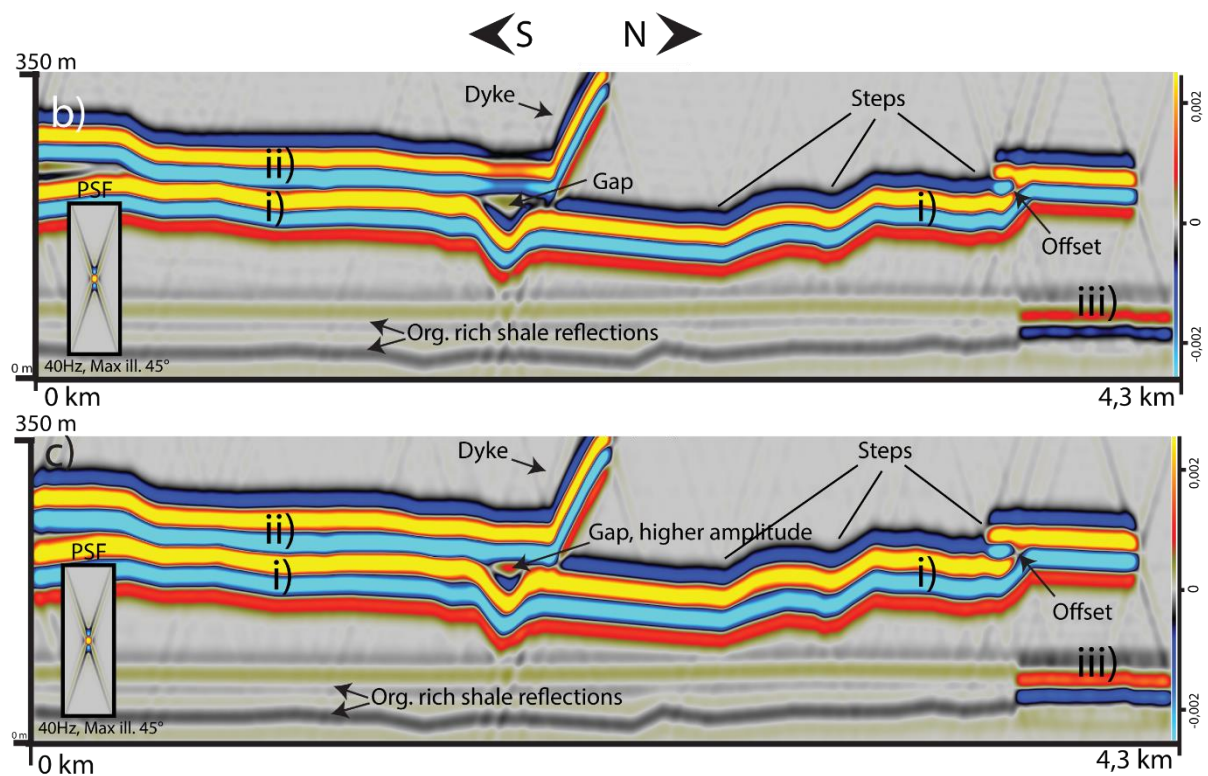


Figure 5.4.5 – Seismic 40-Hz images of Botneheia east. a) Without contact aureole, b) Including one zone of contact aureole.

### 5.5 Seismic modelling of 3D-model

This section will present the results from seismic modelling of the 3D geological model representing Botneheia, built in Petrel and RMS. The seismic images are created by following the steps described in section 4.4.2.

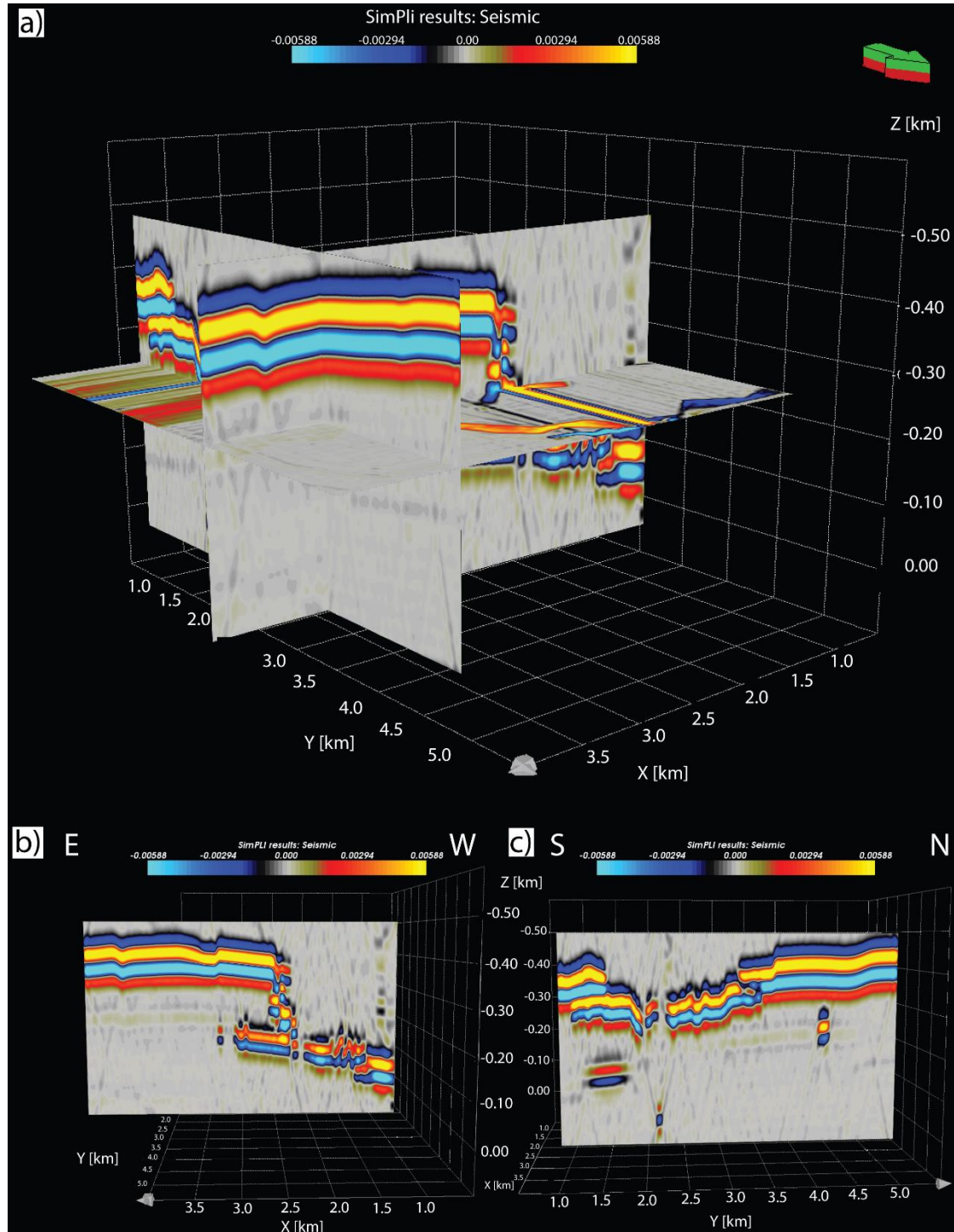


Figure 5.5.1 – a) 3D visualization of the 3D synthetic seismic at 20 Hz with max illuminated dip 45 degrees. b) 3D synthetic seismic image of the northern side of Botneheia. c) 3D synthetic seismic image of the eastern side of Botneheia. Vertical exaggeration 3x.

The modelled facies for the 3D model are sand, fine sand, shale, organic rich shale and intrusion, and the corresponding elastic properties for these facies have been used (Table 4.3-1). A contact aureole is not included, in contrast to the modelled cases in the 2D seismic images, due to the high time cost for such detailed model building.

The 3D synthetic seismic images are similar to those of the modelled 2D cases. This is expected as both the 2D- and 3D-model(s) are based on the same interpretation from the virtual outcrop models and the facies have the same elastic properties, while the seismic modelling method is equivalent (but using a 3D PSF and coarser sampling). High-amplitude reflections dominate the seismic images, representing the intrusions, but one can see some low-amplitude reflections as well, corresponding to the host-rock facies boundaries, as in the 2D cases. The geometry of the high-amplitude reflections varies in both lateral and vertical directions, and one can then analyse the modelled seismic versus the input model (Figure 5.3.1). The advantage of a 3D model is indeed that one can go through slices of the model in all directions. Consequently, a high number of seismic images can be analysed in order to examine how the geological features - in this case intrusions - are imaged, especially laterally. A few selected seismic images will be displayed in the following, this in order to focus on key results.

The synthetic seismic presented in Figure 5.5.2 has a high resemblance to the input model, but also to the 2D seismic images of the northern side of Botneheia, as presented in the previous section. This is expected, as the input- and seismic-slice picked for Figure 5.5.2 are approximately matching the outcrop section, i.e. also being the basis for the 2D geological models previously discussed. Seismic images at 20 Hz and 40 Hz from 3D seismic data of the northern side of Botneheia will only be briefly described here by addressing the differences with the 2D ones. Figure 5.5.2, b and c) show overall the same intrusion geometry, while there are more details, i.e. thinner and more reflections resolved, at 40 Hz, as previously observed. The host rocks are nearly not resolved at all, except for a couple of horizontal reflections of low amplitude underneath intrusion (i). The transgressive intrusion (dyke) is not well imaged, as it consists of several small high amplitude reflections on top of each other, probably due to the cell-based structure of the input model. This is also observed for intrusion (ii), where several individual small reflections are resolved at 40 Hz, while they are interfering with one another at 20 Hz. There “same” artefacts, i.e. the cross-pattern effects of the PSF, are also present in the 3D seismic images, as for the 2D ones.

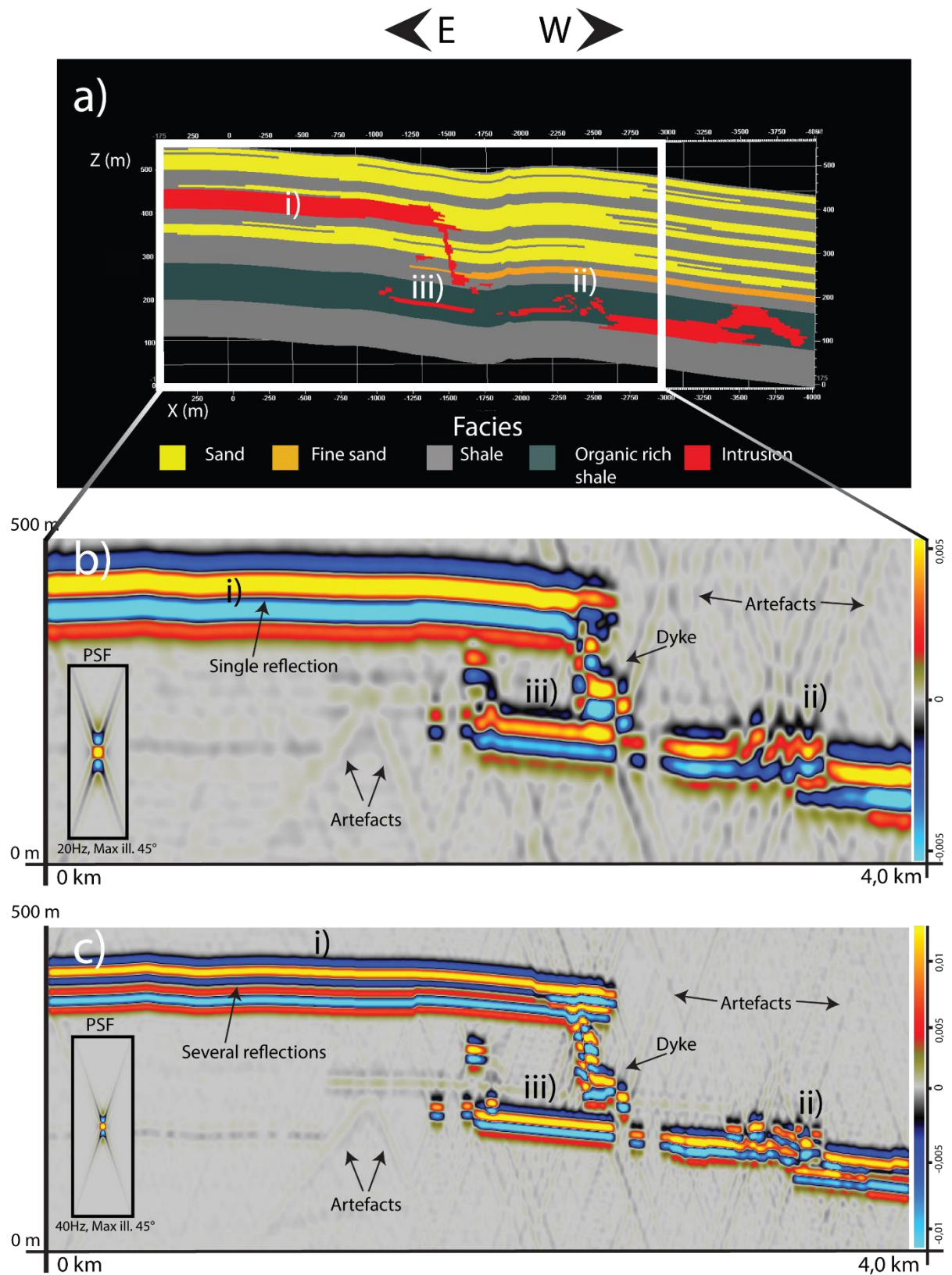


Figure 5.5.2 – Synthetic seismic images from 3D seismic data. a) Slice of input model approximately corresponding to the slice of seismic data viewed in b) and c). b) Seismic image at 20 Hz. c) Seismic image at 40 Hz, from the northern side of Botneheia. NB! a) not to scale with b-c).

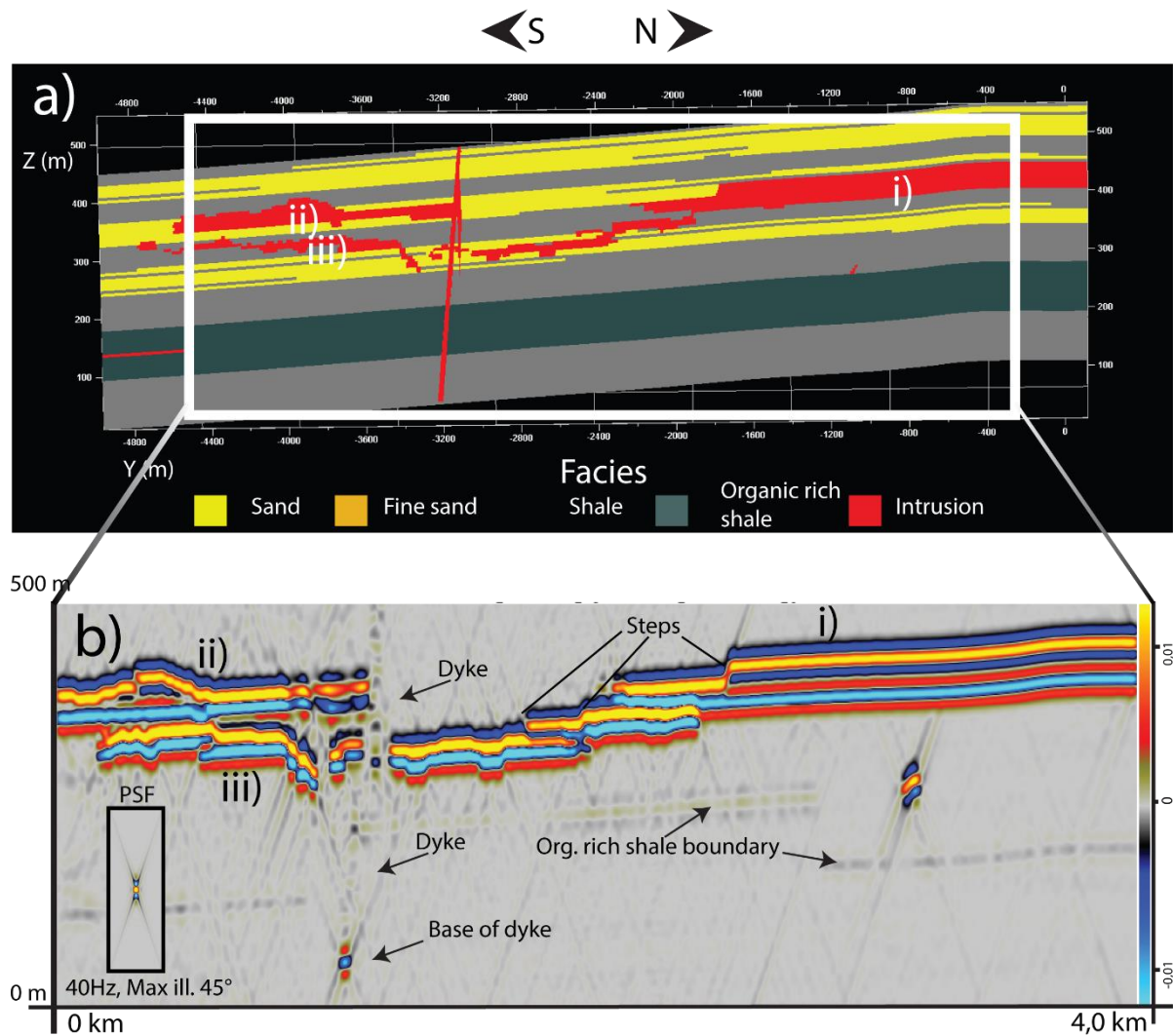


Figure 5.5.3 - Synthetic seismic images from 3D seismic data. a) Slice of input model approximately corresponding to slice of seismic model viewed in b). b) 40 Hz seismic image of eastern side of Botneheia. NB! a) not to scale with b).

The overall imaging result is the same for the seismic image of the eastern side of Botneheia, and the majority of the features are indicated on Figure 5.5.3. One can spot the base of the dyke, which is otherwise not visible, other than by creating discontinuities along its path at the contact with the more horizontal seismic reflections. The top and base reflector of the organic rich shale are only visible at some locations.

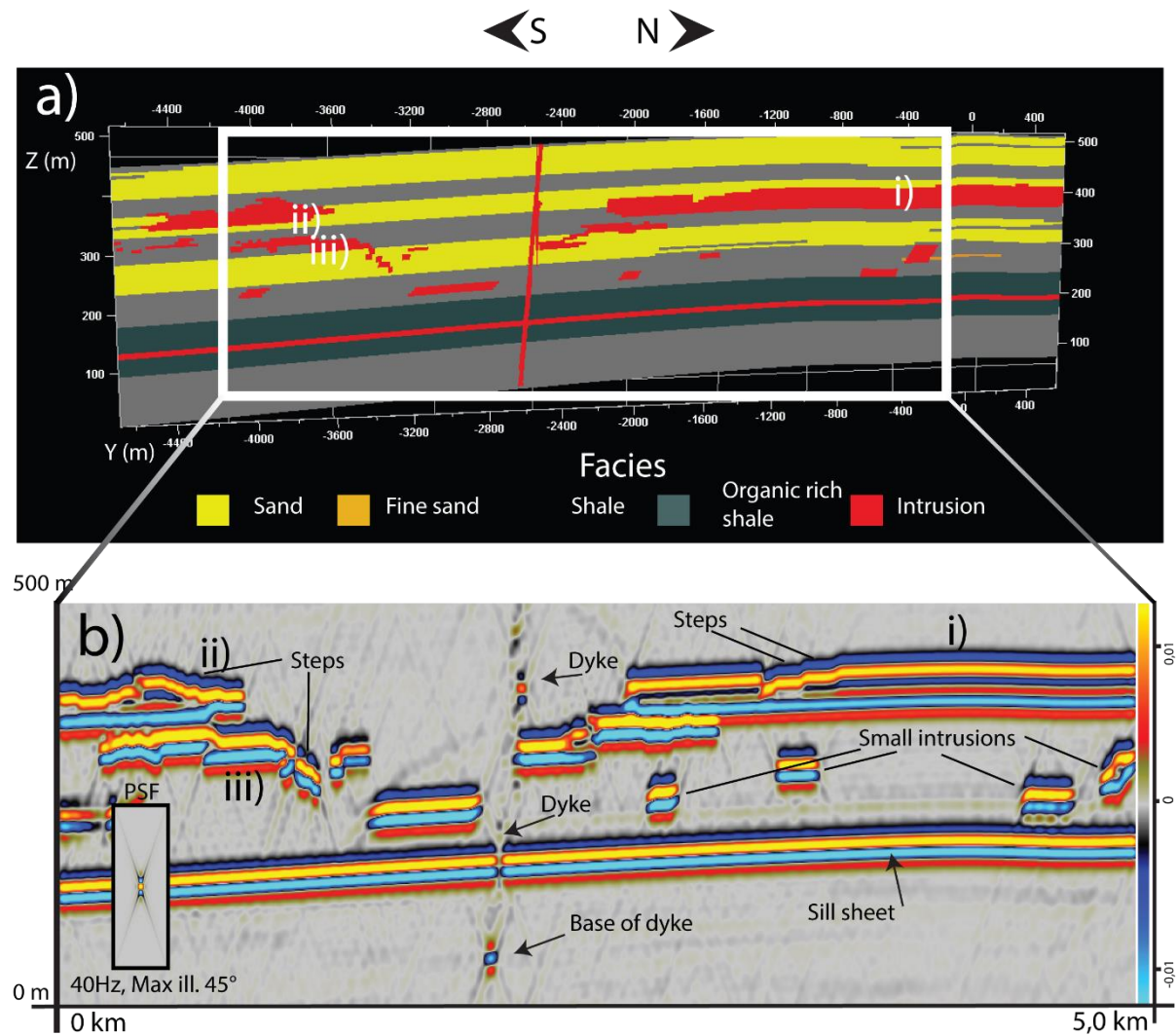


Figure 5.5.4 - Synthetic seismic image from 3D seismic data. a) Slice of input model approximately corresponding to slice of seismic model viewed in b). b) 40 Hz seismic image of eastern side of Botneheia. NB! a) is not to scale with b).

Figure 5.5.4 presents another section of the 3D seismic data, located “within” the mountain, and viewed from the east. The overall geometry and amplitudes are similar to the previous presented images. A sill with a large horizontal extent is imaged in the lower half of the section. The dyke is also visible at its base and by creating discontinuities in the rest of the seismic image. Several steps within intrusion (i-iii) and small intrusions and/or splays are well imaged.

The 3D seismic dataset can also be viewed in XY sections, i.e. at constant Z (depth), as viewed in Figure 5.5.5. The presented section is chosen as it represents some of the same intrusions as already seen in previous sections. Intrusion (i) and (ii) in Figure 5.5.5 correspond to intrusion (i) in Figure 5.5.2, and intrusion (ii and iii) in Figure 5.5.3-5.5.4, respectively. One can also see

the dyke cutting through Botneheia, and the other main intrusions, e.g. (i) and (ii), are connected to it.

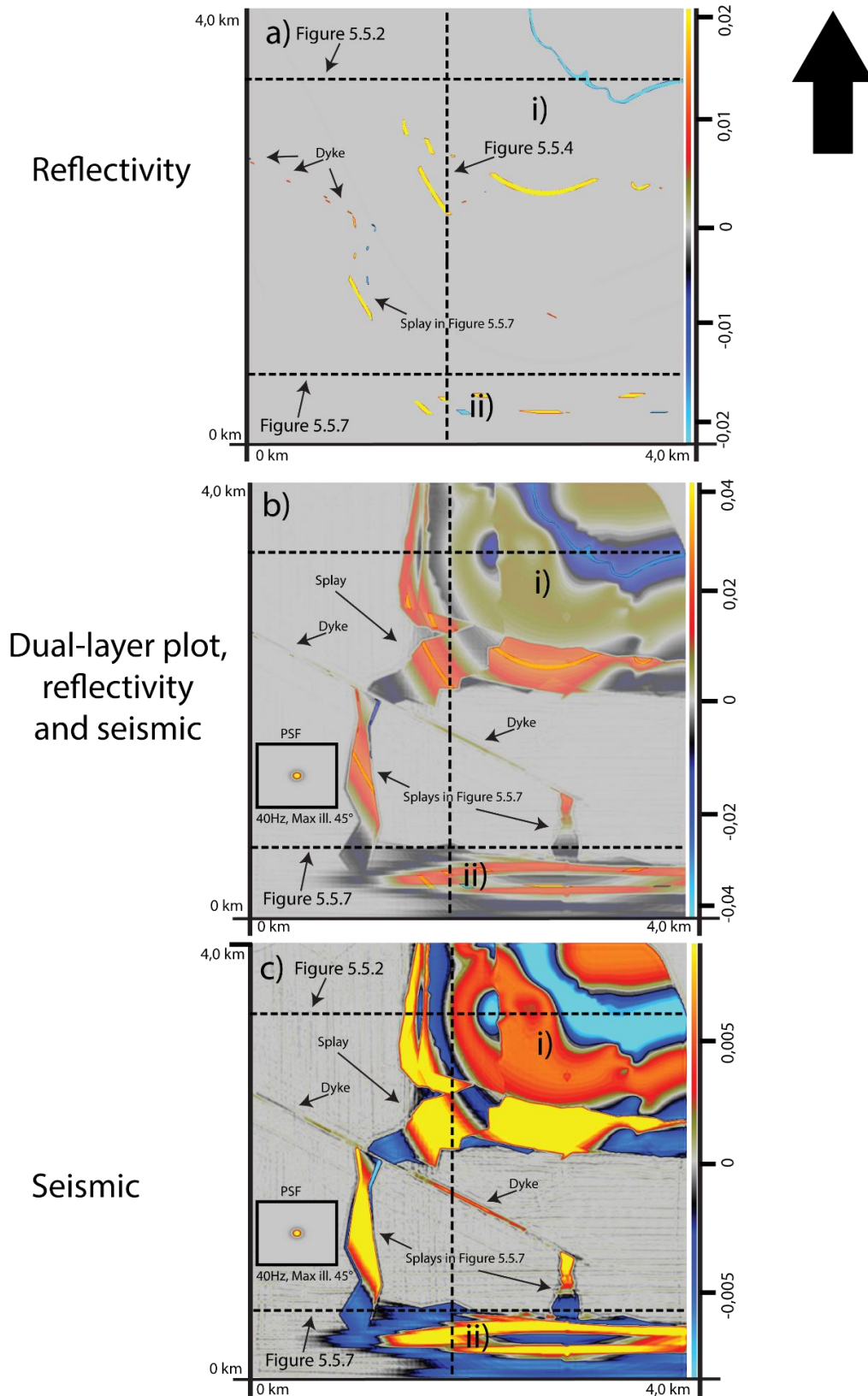


Figure 5.5.5 – 3D synthetic seismic in horizontal plane. a) Reflectivity model. b) Dual plot of reflectivity and seismic image, note how the reflections are smeared in the lateral direction. c) Seismic image at 40 Hz.

There are structures in the seismic horizontal section, which is not present at the same slice in the reflectivity model. This is illustrated in Figure 5.5.5, where the reflectivity in Figure 5.5.5 a) shows a number of reflectivity structures, while the resulting seismic image (Figure 5.5.5 b - c) shows a significant more complex picture, i.e. additional and smeared structures. This is due to both vertical and lateral resolution interplay, i.e. structures below/above interfering. Consequently, less or more structures may be imaged in the seismic data, than what is present in the reflectivity plot of the corresponding section. In addition, amplitudes are affected by the planar nature of the seismic section, i.e. the horizon in the input model can have an undulating topography which is cut by the seismic section (Figure 5.5.6 a-b), thus leading to amplitude variation, e.g. the circular pattern for intrusion (i) (Figure 5.5.5 b-c). One can also see the dyke cutting through Botneheia, and the other main intrusions, e.g. (i) and (ii), are connected to it.

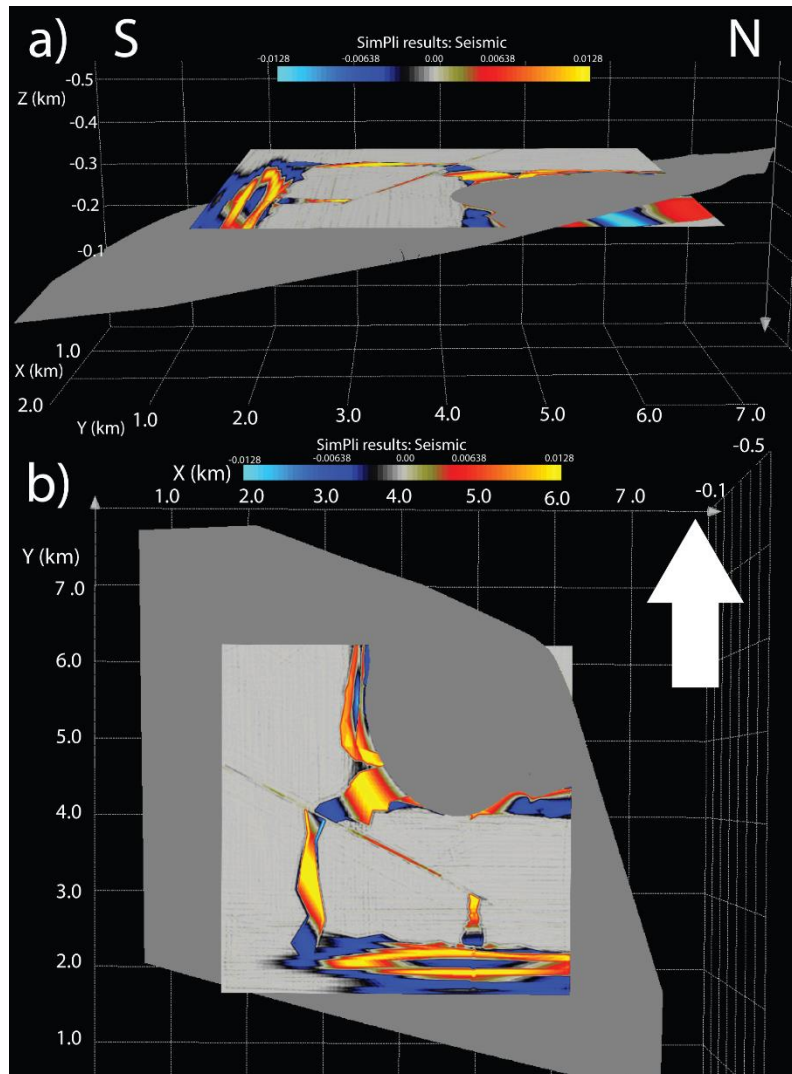


Figure 5.5.6 – Illustrating how the planar geometry of a horizontal section in the seismic (40 Hz image) is related to the topography of a horizon from the input model. a) Note how the planar seismic section “cut” the horizon, creating a “circle shape”, viewed from above in b). This shape is evident in Figure 5.5.5, b-c) through circular amplitude changes for intrusion (i).

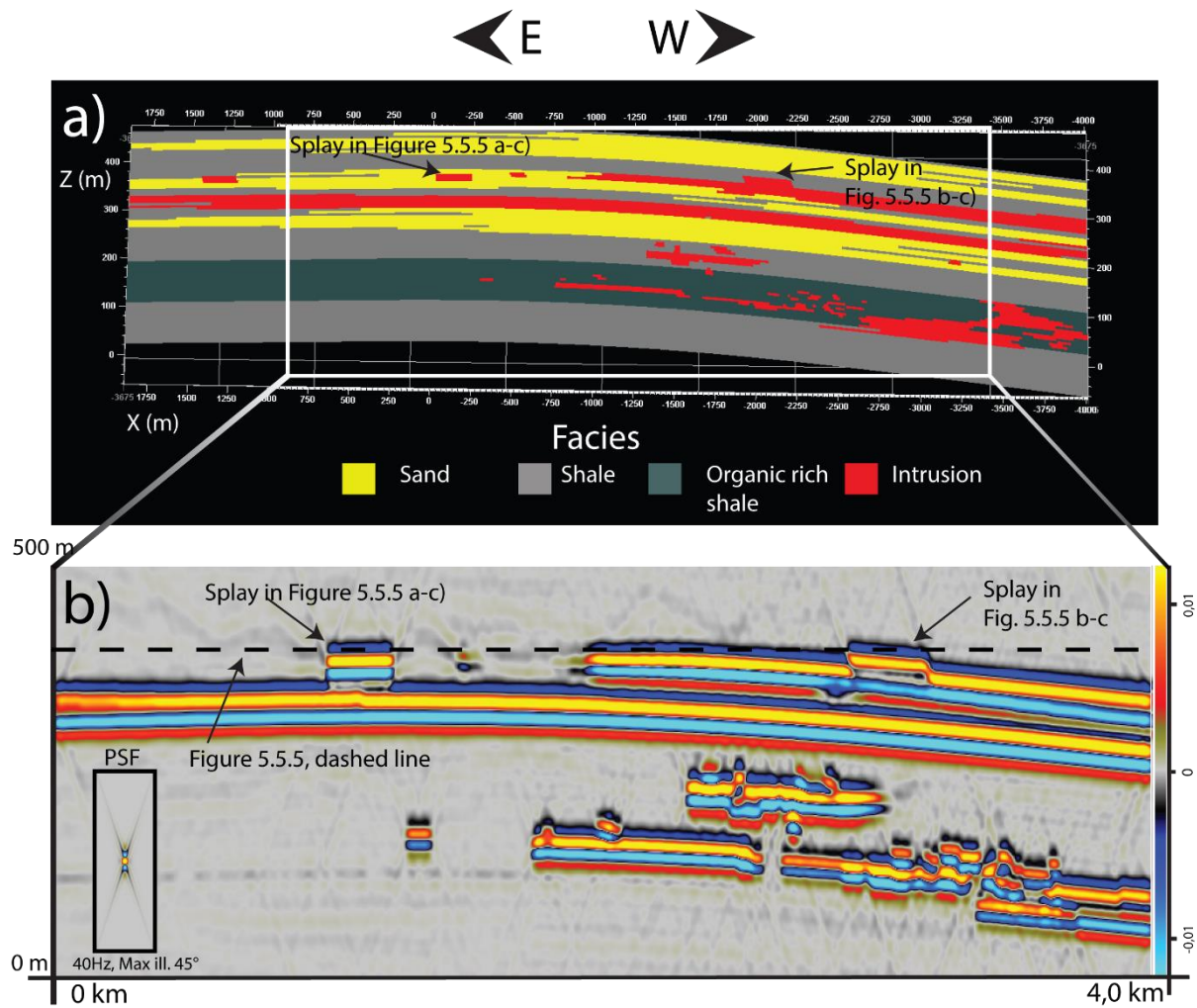


Figure 5.5.7 – Synthetic seismic image from 3D model highlighting presented splays in Figure 5.5.5. a) Input model seen from north. b) Seismic image at 40 Hz, with indicated splays, and dashed line plotting location of Figure 5.5.5.

The figure above is presented in order to illustrate the location of Figure 5.5.5 and the position of the splays that are imaged in Figure 5.5.5. These splays seem to have a simple geometry when viewed in the 2D section in Figure 5.5.7 b), while the geometry actually is complex (Figure 5.5.5 b-c).

## 6 Discussion

The present study of the igneous intrusions at Botneheia integrates a set of results that will be further discussed and assessed in this section. The use of several methods, datasets and theories allows several sensitivity analyses with respect to various parameters, technical or physical. First, the construction and interpretation of virtual outcrop models from photogrammetry is assessed by comparing them to the model from lidar-data. Secondly, the synthetic seismic images resulting from 2D seismic modelling are evaluated to investigate which details that can or cannot be observed at different dominant frequencies. These images will also be discussed regarding the effect on seismic images of igneous intrusions when the petrophysical properties of contact metamorphic aureoles are taken into account; this has not been done in previous and similar studies (e.g. Magee et al., 2015; Eide et al., 2018; Rabbel et al., 2018). Furthermore, the impact of implementing this aureole as only one zone with constant petrophysical properties, versus modelling it with several inner layers, to mimic gradual changes towards the intrusion, will be discussed. Lastly, the seismic images from the 3D synthetic dataset are compared to the 2D ones.

### 6.1 Comparison of outcrop models from photogrammetry vs. lidar-data

The construction and interpretation of virtual outcrop models based on photos collected in the field have been described and presented in section 4.1.3 and 5.1, respectively. The overview virtual outcrop models from photogrammetry represent Botneheia in a good manner, but disconnected and offset parts result in a reduced overall connectivity and quality of the outcrop sections, i.e. parts are disconnected from one another and/or smeared, so that geological features are difficult to follow (Section 4.1.3, Figure 4.1.4). These issues can cause a less accurate interpretation of geological features and uncertain/wrong (several metres) measurements of distances. Consequently, interpretations of geological units may be mismatched, i.e. appearing discontinuous, thus making it hard to use as basis for further modelling, e.g. building of a geological model. Therefore, the lidar-data proved to be very valuable to constrain the main geological interpretations. This model is of high quality, having no disconnected or smeared parts and it was thus the fundament for the build of the 2D- and 3D- geological models. Nevertheless, as data are missing in parts of the lidar-scan, a virtual outcrop model of the northern side of Botneheia from photogrammetry provided valuable information. Thus, the

photogrammetry completed the interpretation of the lidar-scan, this yielding a more complete dataset.

Virtual outcrop models from photogrammetry is a cost- and time-efficient method for gathering geological information, consequently extending the “field-season” by allowing for interpretation of outcrops in the office. Nevertheless, as presented, problems may arise when gathering photos that way. Most likely, due to it being a terrestrial photogrammetric survey covered over large distances by foot, thus making it difficult to gather data in the exact same manner, e.g. distance and angle to outcrop, and changing light and weather conditions may also alter the result, since it has to be done over several days. In contrast, a lidar-scan can cover large areas over shorter time and the result may therefore be of higher quality (Buckley et al., 2008a). However, this would most likely result in a higher cost, given a helicopter-based approach, thus demanding a well-funded project. Acquiring virtual outcrop models from photogrammetry is instead a low-threshold method and the results are especially good given the cost and time put in. This method (in combination with the lidar-data) contributed with valuable constraints for the following geological modelling in this study.

## 6.2 Limitations in geological models and associated elastic properties

The geological models in this study are built from the interpretation of virtual outcrop models as basis, with the aim to give a first (simplified) representation of the Botneheia mountain, in both 2D and 3D, for use in seismic modelling. There is a level of uncertainty in the models because the representation of the geological features is dependent on the interpretation of the virtual outcrop models. This interpretation may be inaccurate and thus resulting in incorrect geometry of the geological features. This is especially the case for the host rocks present at Botneheia, because the interpretation of these units have been simply extrapolated into areas with missing data. Nonetheless, the uncertainty and errors related to the modelling of host rocks would probably only lead to small changes on the corresponding seismic images. This is due to the high contrast in acoustic impedance between the intrusions and the surrounding host rocks, as previously presented. As a result, a more detailed modelling of the host rocks would probably not change the outcome of this study.

Moreover, the main aim of the study is to examine the imaging potential of the igneous intrusions, thus the focus was on modelling these with a high degree of detail. Following this, the intrusion geometry in the geological models was kept close to the actual geometry in the outcrop sections, especially for the 2D geological models, which directly represent the studied outcrop sections. This is slightly different in the 3D geological model, as the interpretation from the outcrop sections has been extrapolated laterally, in order to model a 3D geometry. There is thus a high degree of uncertainty related to this, as the modelling in the third dimension is based on conceptual and simplified ideas of intrusion geometry and connectivity. The intrusion geometry within Botneheia is indeed unknown, and the modelling within the mountain may be completely inaccurate. In addition, the 3D geological model was not modelled including a contact aureole, in contrast to the 2D-models, this due to the high time cost in building that model and the degree of detail is therefore limited. This high time cost is mainly related to the implementation of realistic intrusion geometries, which practically requires a manual discretization. As the 3D model is gridded, i.e. cell-based, intrusion geometries are built by assigning each cell the facies-value “intrusion”, a contact aureole was therefore not included for such practical reasons. Therefore, there are aspects of the 2D-models that are not comparable to the 3D model, the former being especially useful for more detailed structures (e.g. the contact aureoles). Still, the 3D geological model gives a valid, though simplified, representation of Botneheia and its potential intrusion geometries. In addition, the present work provides a valuable workflow for building 3D geological models input to seismic modelling in 3D.

A contact aureole is surrounding the intrusions in the 2D geological models, modelled in two different cases for Botneheia north and one for Botneheia east. The basis for the size (100 - 150% of sill thickness), and the choice of the zone setup has been described earlier, but the uncertainty of the modelling has not yet been evaluated. The thickness of the contact aureole in this study is within the interval of expected thickness from literature, i.e. ~ 30 - 200% of sill thickness (e.g. Aarnes et al., 2010; Senger et al., 2014a), and it is supported by field observations. To account for the wide spread in sill thickness from literature (mentioned above), the thickness of the modelled contact aureole did vary slightly in this study. A fluctuating thickness of the contact aureole may also be the case in reality, and the modelled contact aureole in this study may still thus give a valid representation of the distribution of such a zone.

Once built, the geological model is assigned elastic properties, i.e.  $V_p$ ,  $V_s$ , density, because they are needed for the seismic modelling. Consequently, the chosen values influence the

resulting seismic. Rabbel et al. (2018) did present seismic modelling results including vertical variability (that was extrapolated laterally) in the host-rock elastic properties, which to a high degree influence the resulting seismic images. For this study, no lateral or vertical variability of the elastic properties within the geological units were introduced, mainly for the sake of simplification. This is indeed a simplification because these properties are expected to vary within the various host rocks and intrusions. However, the sedimentary strata at Botneheia mainly consist of shale, organic rich shale, and sand with varying grain size. These sedimentary units have low acoustic impedance values, due to little variation in elastic properties (e.g.  $V_p$ : 3092 - 3277 m/s, Table 4.3-1). Consequently, the resulting reflectivity (due to rapid changes of AI) values between the host-rock units are low (no significant seismic signals), while the AI from the intrusions are high in comparison (Figure 5.4.1), thus yielding a large reflectivity value at the contact between host rock and intrusions. As a result, using variable host-rock elastic properties for the facies in this study may not lead to significant differences, because the intrusions would stand out nonetheless. In contrast, the host rocks modelled by Rabbel et al. (2018) consisted of evaporates, carbonates and organic rich shales with a high variability in seismic properties ( $V_p$ : 3350 - 5950 m/s), thus less of a contrast in AI between host rocks and intrusions. As a result, the intrusions does not stand out from the host rocks, and are more difficult to interpret as the reflections are closer in amplitude and interfere with one another.

The way elastic properties are modelled towards the intrusion within the inner layers of the contact aureole may however matter for the resulting seismic images. The elastic properties of the contact aureole with inner layers have been modelled after the schematic log responses in Smallwood and Maresh (2002), as illustrated in Figure 3.2.1 and described in section 4.3. This setup is also supported by the sonic log, i.e.  $V_p$ , in well 7715/3-1 (Figure 6.2.1), which shows a log response very similar to that of Smallwood and Maresh (2002).

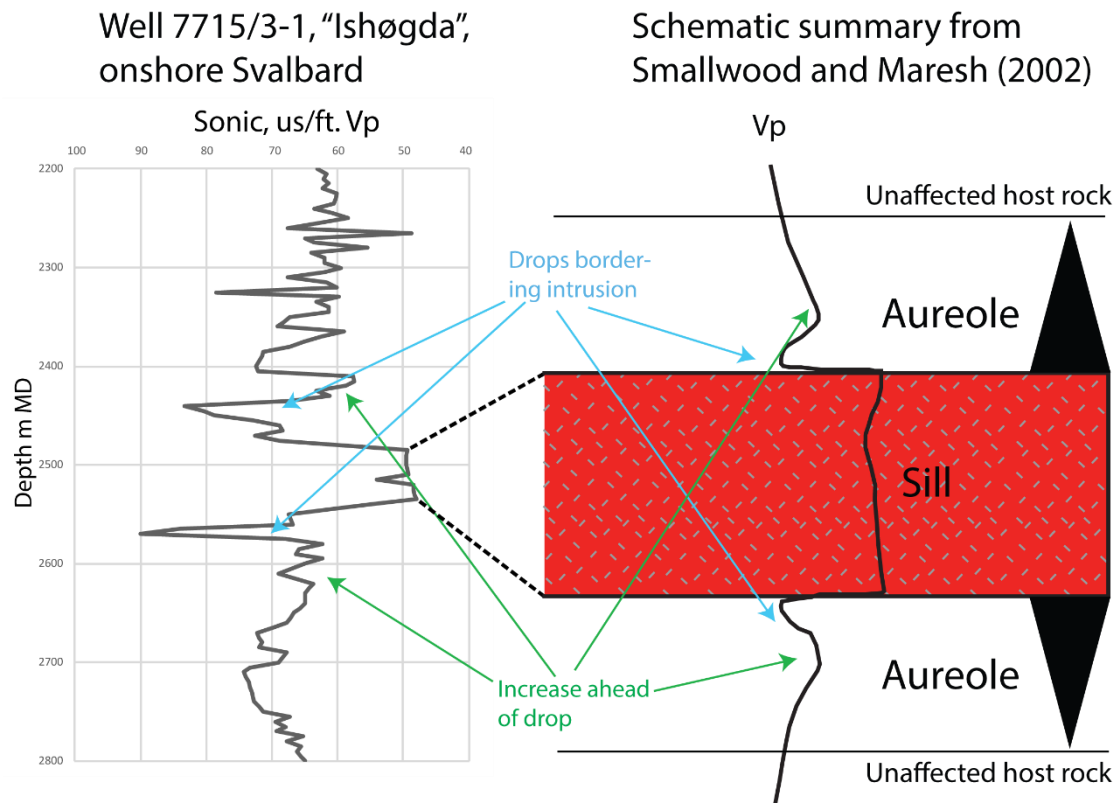


Figure 6.2.1 – Comparison between sonic log response, i.e. Vp, with schematic log response of Smallwood and Maresh (2002). Note the similarity of the logs, also highlighted in the figure. Dashed lines indicate where the sill is located in the log in well 7715/3-1 and correlate the sonic response to the schematic summary to the right.

### 6.3 Seismic modelling

This section will evaluate the seismic images from the seismic modelling of 2D and 3D geological input models. The images are assessed regarding change of dominant frequencies, and with and without contact aureoles, i.e. test the effect of implementing it as one layer versus multiple layers to mimic gradual changes often observed in contact aureoles of other studies, and 2D images will be compared to 3D images.

#### 6.3.1 Change of dominant frequencies

The 2D and 3D seismic images relate well to the input models and the main intrusion geometries are overall properly imaged, as seen from the results, e.g. Figure 5.4.1 – 5.4.2 and Figure 5.5.2 – 5.5.5. The intrusions stand out from the host rocks due to a high contrast in AI, and the host rocks are barely or not imaged, in comparison. However, the seismic expression of the intrusions vary when models are generated with different frequencies. The 20-Hz images provide reflections with overestimated thicknesses and details are not well resolved. This is the

result of tuning effects and interference with other reflections due to lack of resolution. The latter may also lead to amplitude variations, and seismic image artefacts. Magee et al. (2015) presented an example of such artefacts, with apparent steps (pseudo-steps) in transgressive intrusions resulting from interference with reflections from host-rocks with planar bedding. Such pseudo-steps are not observed in this study, which can be the result of several factors, i.e. 2(3)D convolution modelling contra 1D (i.e. proper modelling accounting for lateral resolution effects used here), higher contrast in AI and homogenous host-rocks (Eide et al., 2018). Given a model with layered host-rocks, such apparent steps would not necessarily appear, as demonstrated by e.g. Flesland (2017).

As there are limitations in the resolution at 20 Hz, small splays and other details are not well resolved (Figure 6.3.1 c). This may lead to interpretation issues with real seismic data because details may be overlooked. This may further induce risks for well-planning, if the area is subject to e.g. exploration, petroleum production or CO<sub>2</sub>-injection. Intrusions are namely hard and can lead to challenging drilling conditions (Farooqui et al., 2009). However, the intrusions are well resolved at 40 Hz (Figure 6.3.1 d), with a more accurate thickness and structures are easier to identify due to a higher degree of detail, i.e. higher resolution. In this case, an average velocity of 3700 m/s and dominant frequency of 20 and 40 Hz are used in the modelling (Figure 6.3.1 c-d). These factors yield a vertical resolution ( $\lambda/4$ ) of  $\sim 46$  m for the seismic at 20 Hz (Figure 6.3.1 c) and  $\sim 23$  m for the 40-Hz image (Figure 6.3.1 d). Due to this, splays and other small features related to the intrusions may be identified and accounted for in the interpretation of a real seismic dataset at 40 Hz. Yet, steep features as splay 3 in Figure 6.3.1 may not be resolved at all at 40 Hz either. In addition, frequencies and seismic energy are lost with depth, thus one may not be fortunate enough to have a dataset with a dominant frequency of 40 Hz at the depth where the intrusions are located. A dominant frequency of 40 Hz can correspond to a target depth of 1 km (e.g. Eide et al., 2018). Consequently, the intrusions are imaged at a dominant frequency lower than 40 Hz if they are located at a deeper depth, and therefore with less details (Figure 6.3.1 c), e.g. at 3 km at 20 Hz. The details resolved in the 40-Hz synthetic images are therefore valuable analogues to seismic datasets with similar dominant frequencies and resolution, though not directly applicable for datasets with other properties.

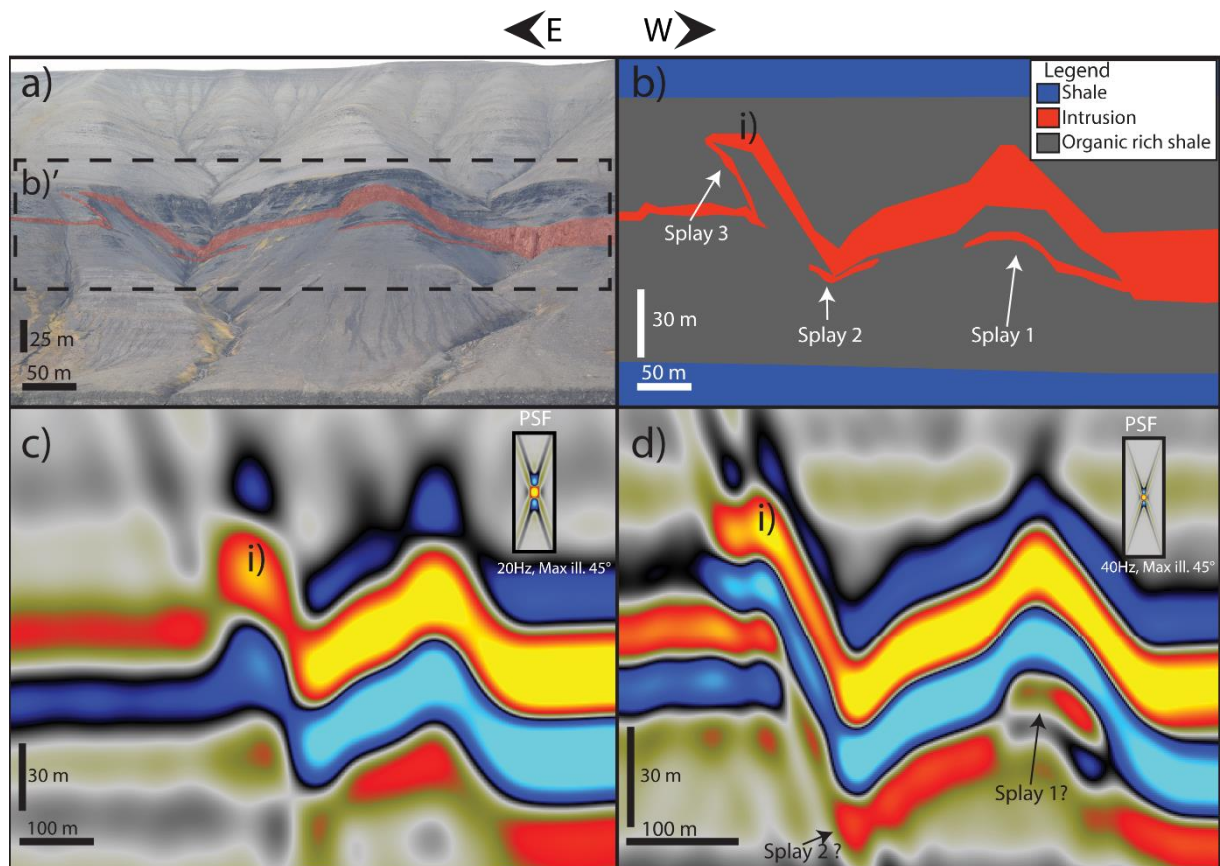


Figure 6.3.1 – Focused sections of Botneheia north. a) Photo from fieldwork with main intrusion geometries marked in red. b) Focused section of 2D geological model (without contact aureole) of Botneheia north, captured from Figure 5.2.1 b). c) Synthetic seismic image at 20 Hz, focused section from Figure 5.4.1 b). d) Synthetic seismic image at 40 Hz, focused section from Figure 5.4.1 c). Note that the splays are not resolved in c) at all, while splay 1 and 2 are barely resolvable in d). Splay 3 is not imaged in either c) or d).

### 6.3.2 Effect of contact metamorphism – one zone vs. several inner layers in zone

Igneous intrusions affect the host rock they enter by developing contact aureoles due to the high temperature of the melt; such contact aureoles are therefore implemented in the 2D models of this study, as earlier presented. The effect of this implementation in the 40-Hz seismic images is twofold: (1) it affects the way the reflection of the intrusion is resolved, i.e. a strong combined reflection and/or individual ones, (2) the amplitude of the major intrusions is lowered. The first effect (1) can thus lead to an overestimation of the thickness of the intrusion itself, which is observed both at 20 and 40 Hz in the wiggle-plots and the resulting seismic images (Figure 5.4.3 - Figure 5.4.4 and here; Figure 6.3.2). This may thus have implications for a seismic interpreter that needs to estimate the thickness as precise as possible, e.g. for well planning and/or volume estimations. As presented in section 5.4.2, the first effect (1) may also lead to several reflections being resolved for parts of the intrusion reflection, e.g. for intrusion (iii) in Figure 6.3.2 b). The contact aureole in case (1) is modelled by one zone, which mainly appears as a combined reflection for intrusion (ii) and (iii), with some dual reflections in parts of

intrusion (iii), i.e. due to the high resolution at 40 Hz. However, in case (2) the zone consisting of several inner layers is represented by only one additional individual reflection in addition to the intrusion (ii) reflection itself (Figure 6.3.2 c), while the zone actually consists of in total five layers. This is a result of the tuning effect, in which the five inner layers of the contact aureole in case (2) interfere with one another, resulting in a combined reflection. Yet, intrusion (iii) in (Figure 6.3.2 c) is only represented by a single reflection, in contrast to intrusion (ii) in the same figure. In real seismic, this could be a result of loss of high frequencies and energy below intrusion (i). However, as this is a synthetic model, the seismic image is idealised and does not incorporate such real effects. Therefore, the single reflection (Figure 6.3.2 c) is also a result of the tuning effect.

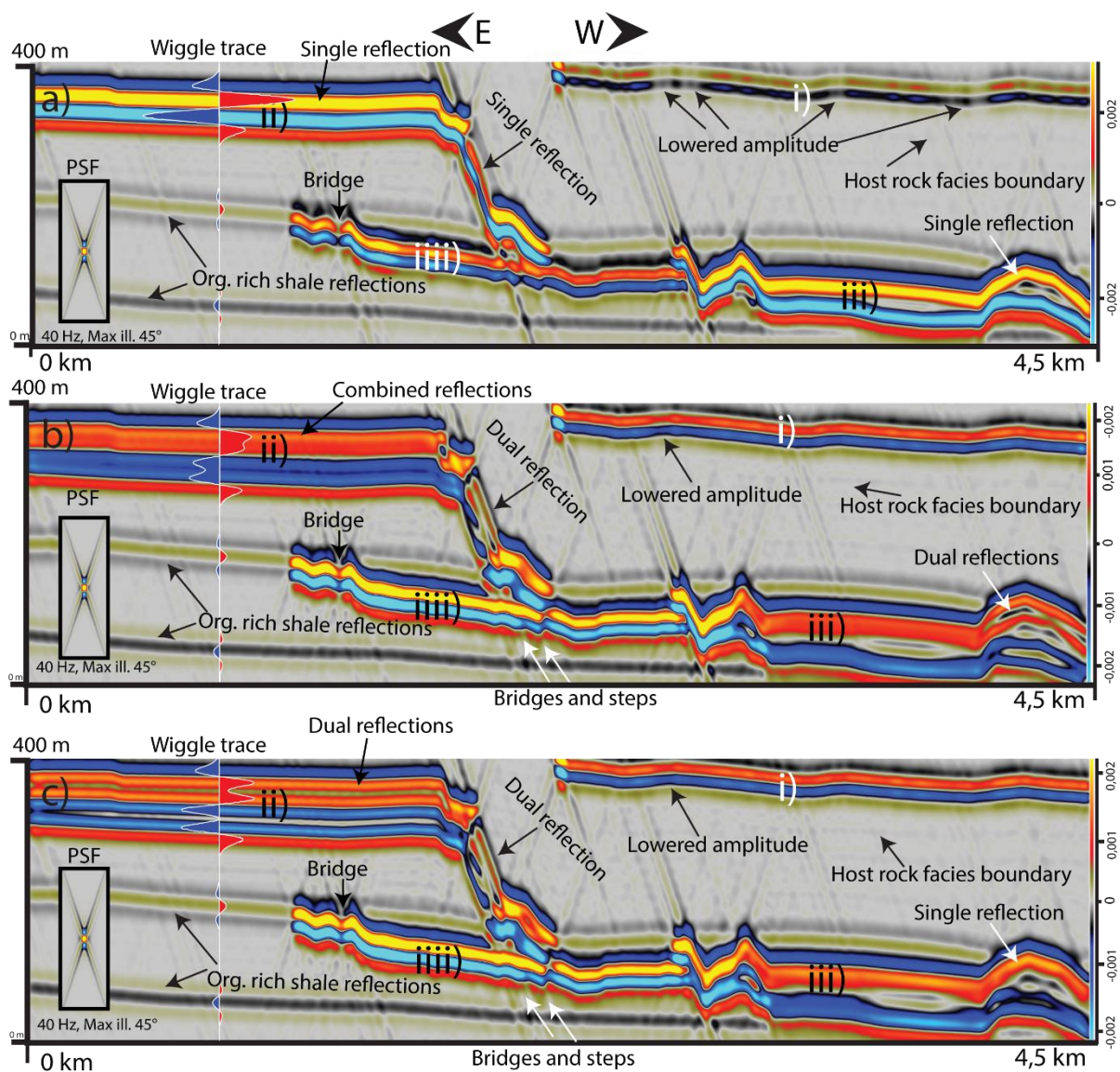


Figure 6.3.2 – 40-Hz seismic images of Botneheia north with included wiggle trace. a) Without contact aureole. b) Including one zone of contact aureole. c) Including several inner layers of contact aureole.

The latter effect (2) is that the overall amplitude for the seismic data is lowered when implementing a contact aureole. This is clearly visualised for both 20 Hz and 40 Hz in the wiggle-plots, but also in the seismic images. The model without a contact aureole has significantly higher amplitude (Figure 6.3.2 a) than the following two cases where the contact aureole is included (Figure 6.3.2 b-c). This result is interesting, as every intrusion affects the host rock in which it enters. To which degree the host rock is altered is highly variable and dependent on several factors, i.e. melt temperature, size, distribution, stacked or individual sills. Consequently, the host rock alteration can lead to a change in seismic properties, which can have an effect, as seen, on the imaging of the intrusion, i.e. by lowering the amplitude in this study. The way the contact-aureole is implemented in modelling studies can therefore also be of significance, e.g. when it comes to contact aureole thickness, distribution, one zone vs several inner layers, etc. Five zones are used in this study, but the result would maybe differ by increasing this number. Increasing the number of zones could probably lead to a thicker reflection with a lowered amplitude, as the zones would interfere with one another, given that they are modelled closely together.

An overall lowered amplitude for the intrusions does not however reduce the detectability of the intrusions for the seismic images in this study, i.e. due to the very high contrast in acoustic impedance between the intrusions and the host rocks. Nevertheless, if this contrast is lower, as in Rabbel et al. (2018), it would maybe be more difficult to detect the intrusions in the layered model with host-rocks with high acoustic impedance. It should be noted that the detectability also depends on the amplitude of the seismic signal in relation to noise. Noise from acquisition and processing is commonly present in actual seismic data, and only partially removed by processing. The issue with modelling noise is that it is difficult to model it in an accurate manner (Scales & Snieder, 1998). Consequently, there would be no good way of constraining if the detectability in the resulting seismic image is realistic or not. A contact aureole clearly affects the imaging potential of the intrusions, and should thus be implemented in seismic modelling studies, to better represent an analogue for how intrusions are imaged in real seismic data. However, this requires a better petrophysical and elastic characterization of such contact aureoles.

### 6.3.3 Comparison between 2D- and 3D synthetic seismic

This study presented synthetic seismic images from both 2D- and 3D-geological input models. The resulting images have resolved the main intrusion geometries and the detectability of sills is high in both datasets. A change of dominant frequencies has already been discussed with the 2D cases, but the degree of detail and interference within the 2D- and 3D-models have yet not been compared, and will thus be done in the following.

The seismic images resulting from the 3D model have a less degree of detail, which is expected because the sampling is different (section 4.4.1 - 4.4.2) and it was not modelled with a contact aureole, due to the high time cost related to manually building such a large geological model (~140 million cells) as previously described. However, the 3D seismic images are highly valuable as they allow for the analysis of a high number of slices, cutting through the model in all three directions, especially in the horizontal plane. This allows for the interpretation of structures that may interfere with other features located above/under and nearby. As a result, such interferences may result in imaging of features on slices/sections in which they originally do not appear on in the input model (Figure 5.5.5). Consequently, it leads to a better understanding of how features, i.e. intrusions in this study, are imaged. In combination with the 2D-data, it gives a better knowledge of what is behind the seismic data. Nonetheless, the intrusion geometries detected in the seismic images from within the mountain of Botneheia are uncertain, as this geometry is based on extrapolated geometries seen in a few outcrop sections. Thus, the seismic images from within the mountain do probably not give a complete representation of how the intrusions distribute. However, it still gives one scenario out of many, and as such provides insights on how sills and dykes interfere with one another in a 3D dataset.

To the knowledge of the author, this study is the first to model igneous intrusions in 3D synthetic seismic data with a 3D PSF-based convolution approach; there is therefore limited studies that can be compared to the results in this study; other studies involving such 3D seismic modelling concerned different geological structures (Botter, 2016; Mascolo, 2016). However, this study already demonstrates a complete workflow from outcrop to synthetic seismic, for both 2D- and 3D-models, and opens the door for more complex models of igneous intrusions and various sensitivity analyses of their corresponding seismic images.

## 7 Conclusions and further work

This interdisciplinary study has presented well-exposed intrusions in virtual outcrop models at Botneheia, central Spitsbergen, which are the basis for geological modelling, followed by seismic modelling in both 2D and 3D, the latter being the first of its kind as it includes both realistic intrusion geometries and contact-metamorphic aureoles. The resulting synthetic seismic images have increased the understanding of how igneous intrusions are imaged. The result and discussion in this thesis have led to the following conclusions:

1. Building virtual outcrop models from photogrammetry is a cost- and time-efficient method for gathering high-quality outcrop data in the field, and its potential limitations can be compensated by the use of a complementary lidar-model whenever available.
2. Building of realistic and detailed geological models is time-consuming, especially for 3D modelling in which it may go at the expense of the degree of detail that can be achieved.
3. A complete workflow from outcrop to 3D synthetic seismic is demonstrated and is ready for future work.
4. Igneous intrusions are resolved and detected at both 20 and 40 Hz when the contrast in acoustic impedance to the host rocks are high; however, 40-Hz images provide a higher degree of detail, thus better imaging small structures related to the intrusions.
5. The implementation of a contact-metamorphic aureole leads to (1) combined reflections and/or individual resolved reflections, dependent on the model approach, (2) an overall lower amplitude at both 20 and 40 Hz.
6. The seismic images from 3D modelling visualise the intrusion geometry in all three directions and allow for the interpretation of structures that may induce interference on seismic images. It opens for thorough analyses, and a high number of seismic images can be compared with the input model.

## 7.1 Further work

This thesis is a contribution to a better understanding of the seismic imaging of igneous intrusions. However, this is a complex matter, and the following ideas for future work may improve and extend this study:

- Improve the 3D geological model by increasing the level of detail, i.e. implementing a contact aureole and by doing fieldwork and stratigraphic logging at Botneheia to better constrain the host rock facies.
- Model realistic noise in order to see to which degree it affects the detectability of the intrusions or not, and to which degree it masks fine-scale features and contact-metamorphic aureoles.
- Perform detailed analysis, e.g. P- and S-wave, density, porosity and permeability, of the host rocks, contact aureoles and the intrusions at Botneheia in order to better constrain the properties of the facies, for more precise modelling.
- Use the 3D geological model for fluid flow analyses, in order to see how the intrusions affect the flow and assess the potential implications igneous intrusions have for a hypothetical hydrocarbon-system at Botneheia.
- Register the lidar- and photogrammetry-model(s) together (using e.g. ground control points), in order to reduce the risk of mismatches in the subsequent geological interpretation.

## References

- Aarnes, I., Planke, S., Trulsvik, M., & Svensen, H. (2015). Contact metamorphism and thermogenic gas generation in the Voring and More Basins, offshore Norway, during the Paleocene-Eocene Thermal Maximum. *Journal of the Geological Society of London*, 172(5), 588-598.
- Aarnes, I., Svensen, H., Connolly, J. A. D., & Podladchikov, Y. Y. (2010). How contact metamorphism can trigger global climate changes: Modeling gas generation around igneous sills in sedimentary basins. *Geochimica et Cosmochimica Acta*, 74(24), 7179-7195.
- Bemis, S. P., Micklethwaite, S., Turner, D., James, M. R., Akciz, S., Thiele, S. T., & Bangash, H. A. (2014). Ground-based and UAV-Based photogrammetry: A multi-scale, high-resolution mapping tool for structural geology and paleoseismology. *Journal of Structural Geology*, 69, 163-178.
- Botter, C. D. (2016). *Seismic Imaging of Fault Zones: A synthetic workflow to study the impact of faults on seismic images*. (PhD), University of Stavanger.
- Bryan, S. E., & Ernst, R. E. (2008). Revised definition of Large Igneous Provinces (LIPs). *Earth Science Reviews*, 86(1), 175-202.
- Buckley, S., Vallet, J., Braathen, A., & Wheeler, W. (2008a). Oblique helicopter-based laser scanning for digital terrain modelling and visualisation of geological outcrops. *International Archives of the Photogrammetry, Remote Sensing and Spatial Information Sciences*, 37(Part B4).
- Buckley, S. J., Howell, J., Enge, H. D., & Kurz, T. (2008b). Terrestrial laser scanning in geology: data acquisition, processing and accuracy considerations. *Journal of the Geological Society*, 165, 625-638.
- Buckley, S. J., Ringdal, K., Naumann, N., Dolva, B., Kurz, T. H., Howell, J. A., & Dewez, T. J. B. (2019). LIME: Software for 3-D visualization, interpretation, and communication of virtual geoscience models. *Geosphere*, 15(1), 222-235.
- Corfu, F., Polteau, S., Planke, S., Faleide, J. I., Svensen, H., Zayoncheck, A., & Stolbov, N. (2013). U-Pb geochronology of Cretaceous magmatism on Svalbard and Franz Josef Land, Barents Sea Large Igneous Province. *Geological Magazine*, 150(6), 1127-1135.
- Dallmann, W. K. (Ed.) (1999). *Lithostratigraphic lexicon of Svalbard : review and recommendations for nomenclature use : Upper Palaeozoic to Quaternary bedrock*. Tromsø: Norsk polarinstitutt.
- Dallmann, W. K. (Ed.) (2015). *Geoscience atlas of Svalbard* (no.148 ed.). Tromsø: Norsk polarinstitutt.
- Døssing, A., Jackson, H. R., Matzka, J., Einarsson, I., Rasmussen, T. M., Olesen, A. V., & Brozena, J. M. (2013). On the origin of the Amerasia Basin and the High Arctic Large Igneous Province—Results of new aeromagnetic data. *Earth and Planetary Science Letters*, 363, 219-230.

- Eide, C. H., Schofield, N., Jerram, D. A., & Howell, J. A. (2017). Basin-scale architecture of deeply emplaced sill complexes: Jameson Land, East Greenland. *Journal of the Geological Society*, 174(1), 23-40.
- Eide, C. H., Schofield, N., Lecomte, I., Buckley, S. J., & Howell, J. A. (2018). Seismic interpretation of sill complexes in sedimentary basins: implications for the sub-sill imaging problem. *Journal of the Geological Society*, 175(2), 193-209.
- Farooqui, M., Hou, H., Li, G., Machin, N., Neville, T., Pal, A., Shrivastva, C., Wang, Y., Yang, F., & Yin, C. (2009). Evaluating volcanic reservoirs. *Oilfield Review*, 21(1), 36-47.
- Festøy, M. (2017). *Integrated characterization of igneous intrusions in Central Spitsbergen*. (MSc), The Arctic University of Norway. Tromsø.
- Flesland, M. (2017). *Controls on architecture and seismic imaging of igneous intrusions: Examples from LIDAR outcrop data on Traill Ø (East Greenland) and seismic data from the conjugate Møre Margin*. (MSc), University of Bergen.
- Friestad, E. (2018). *Synthetic seismic modelling of fluvial channels in the Blackhawk Formation as an analogue to the Triassic Barents Sea*. (MSc), University of Bergen. Bergen.
- Galland, O., Spacapan, J. B., Rabbel, O., Mair, K., Soto, F. G., Eiken, T., Schiuma, M., & Leanza, H. A. (2019). Structure, emplacement mechanism and magma-flow significance of igneous fingers – Implications for sill emplacement in sedimentary basins. *Journal of Structural Geology*, 124, 120-135.
- Hubred, J. H. (2006). *Thermal effects of basaltic sill emplacement in source rocks on maturation and hydrocarbon generation*. (Cand.Scient-thesis), University of Oslo.
- Hutton, D. H. W., Schofield, N., Turner, J. P., & Underhill, J. R. (2009). Insights into magmatism in volcanic margins; bridge structures and a new mechanism of basic sill emplacement; Theron Mountains, Antarctica. *Petroleum Geoscience*, 15(3), 269-278.
- Jakobsson, M., Mayer, L., Coakley, B., Dowdeswell, J. A., Forbes, S., Fridman, B., Hodnesdal, H., Noormets, R., Pedersen, R., Rebesco, M., Schenke, H. W., Zarayskaya, Y., Accettella, D., Armstrong, A., Anderson, R. M., Bienhoff, P., Camerlenghi, A., Church, I., Edwards, M., Gardner, J. V., Hall, J. K., Hell, B., Hestvik, O., Kristoffersen, Y., Marcussen, C., Mohammad, R., Mosher, D., Nghiem, S. V., Pedrosa, M. T., Travaglini, P. G., & Weatherall, P. (2012). The International Bathymetric Chart of the Arctic Ocean (IBCAO) Version 3.0. *Geophysical Research Letters*, 39(12).
- Kallweit, R. S., & Wood, L. C. (1982). The limits of resolution of zero-phase wavelets. *Geophysics*, 47(7), 1035-1046.
- Klausen, T. G., & Mørk, A. (2014). The upper Triassic paralic deposits of the De Geerdalen Formation on Hopen: Outcrop analog to the subsurface Snadd Formation in the Barents Sea. *AAPG Bulletin*, 98(10), 1911-1941.

- Knarud, R. (1980). *En sedimentologisk og diagenetisk undersøkelse av Kapp Toscana Formasjonens sedimenter på Svalbard. (A sedimentological and diagenetic study of the sediments of the Kapp Toscana Formation in Svalbard)*. (Cand. real. thesis), University of Oslo.
- Lecomte, I., Lavadera, P. L., Anell, I., Buckley, S. J., Schmid, D. W., & Heeremans, M. (2015). Ray-based seismic modeling of geologic models: Understanding and analyzing seismic images efficiently. *Interpretation*, 3(4), SAC71-SAC89.
- Lecomte, I., Lavadera, P. L., Botter, C., Anell, I., Buckley, S. J., Eide, C. H., Grippa, A., Mascolo, V., & Kjoberg, S. (2016). 2 (3) D convolution modelling of complex geological targets beyond-1D convolution. *First Break*, 34(5), 99-107.
- Magee, C., Maharaj, S., Wrona, T., & Jackson, C. L. (2015). Controls on the expression of igneous intrusions in seismic reflection data. *Geosphere*, 11(4), 1024-1041.
- Magee, C., Muirhead, J., Karvelas, A., Holford, S., Jackson, C. L., Bastow, I., Schofield, N., Stevenson, C., McLean, C., McCarthy, W., Shtukert, O., & The Leverhulme, T. (2016). Lateral magma flow in mafic sill complexes. *Geosphere*, 12(3).
- Magee, C., Muirhead, J., Schofield, N., Walker, R. J., Galland, O., Holford, S., Spacapan, J., Jackson, C. A. L., & McCarthy, W. (2018). Structural signatures of igneous sheet intrusion propagation. *Journal of Structural Geology*.
- Maher, J. H. D. (2001). Manifestations of the Cretaceous High Arctic Large Igneous Province in Svalbard. *The Journal of Geology*, 109(1), 91-104.
- Malthe-Sørenssen, A., Planke, S., Svensen, H., & Jamtveit, B. (2004). Formation of saucer-shaped sills. In C. Breitkreuz & N. Petford (Eds.), *Physical Geology of High-Level Magmatic Systems* (p. 215-227). London: Geological Society, Special Publications, 234.
- Mark, N. J., Schofield, N., Pugliese, S., Watson, D., Holford, S., Muirhead, D., Brown, R., & Healy, D. (2018). Igneous intrusions in the Faroe Shetland basin and their implications for hydrocarbon exploration; new insights from well and seismic data. *Marine and Petroleum Geology*, 92, 733-753.
- Mascolo, V. (2016). *Geological and seismic modelling of outcropping carbonate systems: an application to the Cretaceous platform-to-basin system of the Maiella Mountain (Central Apennines, Italy)*. (PhD), University 'G. d'Annunzio' of Chieti-Pescara.
- Mjelde, R., Raum, T., Digranes, P., Shimamura, H., Shiobara, H., & Kodaira, S. (2003). Vp/Vs ratio along the Vøring Margin, NE Atlantic, derived from OBS data: implications on lithology and stress field. *Tectonophysics*, 369(3), 175-197.
- Muirhead, J. D., Airoidi, G., White, J. D. L., & Rowland, J. V. (2014). Cracking the lid: Sill-fed dikes are the likely feeders of flood basalt eruptions. *Earth and Planetary Science Letters*, 406, 187-197.
- Planke, S., Alvestad, E., & Eldholm, O. (1999). Seismic characteristics of basaltic extrusive and intrusive rocks. *The Leading Edge*, 18(3), 342-348.

- Planke, S., Rasmussen, T. M., Rey, S. S., & Myklebust, R. (2005). Seismic characteristics and distribution of volcanic intrusions and hydrothermal vent complexes in the Vøring and Møre basins. In A. G. Doré & B. A. Vining (Eds.), *Petroleum Geology: North-West Europe and Global Perspectives - Proceedings of the 6th Petroleum Geology Conference* (p. 833-844). London: Geological Society.
- Polteau, S., Hendriks, B. W. H., Planke, S., Ganerød, M., Corfu, F., Faleide, J. I., Midtkandal, I., Svensen, H. S., & Myklebust, R. (2016). The Early Cretaceous Barents Sea Sill Complex: Distribution,  $^{40}\text{Ar}/^{39}\text{Ar}$  geochronology, and implications for carbon gas formation. *Palaeogeography, Palaeoclimatology, Palaeoecology*, *441*(1), 83-95.
- Rabbel, O., Galland, O., Mair, K., Lecomte, I., Senger, K., Spacapan, J. B., & Manceda, R. (2018). From field analogues to realistic seismic modelling: a case study of an oil-producing andesitic sill complex in the Neuquen Basin, Argentina. *Journal of the Geological Society*, *175*(4), 580-593.
- Ricker, N. H. (1940). The form and nature of seismic waves and the structure of seismograms. *Geophysics*, *5*(4), 348-366.
- Rittersbacher, A., Buckley, S. J., Howell, J. A., Hampson, G. J., Vallet, J., Martinius, A. W., Howell, J. A., & Good, T. (2014). Helicopter-based laser scanning; a method for quantitative analysis of large-scale sedimentary architecture. *Special Publication - Geological Society of London*, *387*(1), 185-202.
- Scales, J. A., & Snieder, R. (1998). What is noise? *Geophysics*, *63*(4), 1122-1124.
- Schmiedel, T., Kjoberg, S., Planke, S., Magee, C., Galland, O., Schofield, N., Jackson, C., Jerram, D., & Junior Research, F. (2017). Mechanisms of overburden deformation associated with the emplacement of the Tulipan Sill, Mid-Norwegian Margin. *Interpretation*, *5*(3), SK23-SK38.
- Schofield, N., Brown, D., Mage, C., & Stevenson, C. (2012). Sill morphology and comparison of brittle and non-brittle emplacement mechanisms. *Journal of the Geological Society*, *169*, 127-141.
- Schofield, N., Holford, S., Millett, J., Brown, D., Jolley, D., Passey, S. R., Muirhead, D., Grove, C., Magee, C., Murray, J., Hole, M., Jackson, C. A. L., & Stevenson, C. (2017). Regional magma plumbing and emplacement mechanisms of the Faroe-Shetland Sill Complex: implications for magma transport and petroleum systems within sedimentary basins. *Basin Research*, *29*(1), 41-63.
- Senger, K., Millett, J., Planke, S., Ogata, K., Eide, C. H., Festøy, M., Galland, O., & Jerram, D. A. (2017). Effects of igneous intrusions on the petroleum system: a review. *First Break*, *35*(6), 47-56.
- Senger, K., Planke, S., Polteau, S., Ogata, K., & Svensen, H. (2014a). Sill emplacement and contact metamorphism in a siliciclastic reservoir on Svalbard, Arctic Norway. *Norwegian Journal of Geology*, *94*.

- Senger, K., Roy, S., Braathen, A., Buckley, S. J., Bælum, K., Gernigon, L., Mjelde, R., Noormets, R., Ogata, K., & Olaussen, S. (2013). Geometries of doleritic intrusions in central Spitsbergen, Svalbard: an integrated study of an onshore-offshore magmatic province with implications for CO<sub>2</sub> sequestration. *Norwegian Journal of Geology*, *93*, 143-166.
- Senger, K., Tveranger, J., Ogata, K., Braathen, A., & Planke, S. (2014b). Late Mesozoic magmatism in Svalbard: A review. *Earth-Science Reviews*, *139*, 123-144.
- Simm, R., & Bacon, M. (2014). *Seismic amplitude : an interpreter's handbook*. Cambridge, England: Cambridge University Press.
- Skogseid, J., Pedersen, T., Eldholm, O., & Larsen, B. T. (1992). Tectonism and magmatism during NE Atlantic continental break-up: the Vøring Margin. *Geological Society, London, Special Publications*, *68*(1), 305-320.
- Smallwood, J. R., & Maresh, J. (2002). The properties, morphology and distribution of igneous sills: modelling, borehole data and 3D seismic from the Faroe-Shetland area. *Geological Society, London, Special Publications*, *197*(1), 271-306.
- Tarduno, J., Brinkman, D., Renne, P., Cottrell, R., Scher, H., & Castillo, P. (1998). *Late Cretaceous Arctic volcanism: tectonic and climatic consequences*. Paper presented at the AGU Spring Meeting.
- Westoby, M. J., Brasington, J., Glasser, N. F., Hambrey, M. J., & Reynolds, J. M. (2012). 'Structure-from-Motion' photogrammetry: A low-cost, effective tool for geoscience applications. *Geomorphology*, *179*(C), 300-314.
- Widess, M. B. (1973). How thin is a thin bed? *Geophysics*, *38*(6), 1176-1180.
- Worsley, D. (2008). The post-Caledonian development of Svalbard and the western Barents Sea. *Polar Research*, *27*(3), 298-317.

### Electronic references

- NPD (2019). Factpages, wellbore 7222/1-1, Norwegian Petroleum Directorate. Retrieved from <http://factpages.npd.no/FactPages/Default.aspx?nav1=wellbore&nav2=PageView|Exploration|All&nav3=7987&culture=en> [Access date: 01.06.2019]
- NPI (2019). Svalbardkartet - Norwegian Polar Institute. Retrieved from <http://svalbardkartet.npolar.no/> [Access date: 01.06.2019]